Physik Department

Future Neutrino Detectors and their Impact on Particle- and Astrophysics

Dissertation

November 2004
Dipl. Phys. Univ. Christian Grieb

Technische Universität
München

Technische Universität München
Physik Department
Lehrstuhl für Experimentalphysik-Astroteilchenphysik E15
Prof. Dr. Franz von Feilitzsch

FUTURE NEUTRINO DETECTORS AND THEIR IMPACT ON PARTICLE- AND ASTROPHYSICS

DIPL. PHYS. UNIV. CHRISTIAN GRIEB

Vollständiger Abdruck der von der Fakultät für Physik der Technischen Universität München zur Erlangung des akademischen Grades eines

Doktors der Naturwissenschaften (Dr. rer. nat.)

genehmigten Dissertation.

Vorsitzender:	Univ.-Prof. Dr. Manfred Lindner
Prüfer der Dissertation:	1. Univ.-Prof. Dr. Franz von Feilitzsch
	2. Univ.-Prof. Dr. Oliver Zimmer

Die Dissertation wurde am 02.12.2004 bei der Technischen Universität München eingereicht und durch die Fakultät für Physik am 14.12.2004 angenommen.

Abstract

The progress in neutrino physics in recent years has brought the research in this field to a new level: where understanding the phenomena discovered with the first generation neutrino experiments (a lack of neutrinos) was the main objective, now the focus is on quantifying the theory which is able to explain the experimental results obtained to date. Neutrino flavor oscillations which allow transitions of one neutrino flavor to another while the neutrinos propagate in space have been proven to be the mechanism which causes the observed lack of neutrinos (of a certain flavor). The improved understanding of the neutrino and its properties now even allows to use neutrinos as powerful probes in astrophysics, cosmology and geophysics.

Chapter 1 will trace the history of the improved understanding of the neutrino from its original postulation by Pauli to the current status of research. The theoretical framework of neutrino oscillations will be explained, and finally a summary of the most interesting open questions, which are either currently or in the near future being addressed by new experiments, is given.

In the following Chapter 2, the Borexino detector and its physics program is presented. Borexino will perform real time spectroscopy of low energy neutrinos from the sun, but is also capable to detect supernova- and geoneutrinos as well as reactor neutrinos.

Chapter 3 describes the development and the production of light collecting mirrors ("light guides") for Borexino. This technique, which can be of great value for future experiments using photomultipliers, allows Borexino to increase the light yield (and therefore the energy resolution) at low cost and with great benefits concerning radioactive background. A Monte Carlo simulation was developed to determine the efficiency of the Germanium de-

tector, which was used to measure the radioactive contaminations in the light guides. A second Monte Carlo simulation then determined the amount of background introduced in Borexino by the light guides.

In Chapter 4, the Borexino Source Calibration System is presented. It will allow to insert radioactive sources into the Borexino scintillator, move them around freely and, at the same time, determine the exact position of the radioactive source independently from the photomultiplier timing information. The technique is cheap and surprisingly accurate. It is based on optical triangulation of a light emitting diode with consumer grade digital cameras. A software has been developed, which allows the user to perform this triangulation with the press of a button. In addition, the system will allow visual surveillance of the detector's inside after it has been sealed.

Chapter 5 focuses on the new Double Chooz experiment, which will probe the so far unknown neutrino mixing angle θ_{13}. The detector and the physics program are presented in detail. Of great concern for this detector was background induced by fast external neutrons. Cosmic ray muons can produce neutrons by spallation processes in the rock surrounding the detector. These neutrons, then, can enter the detector without a strong signal in the muon veto and create background events. A Monte Carlo simulation was developed which determined the amount of background expected from these neutrons.

In Chapter 6, it is shown how the future LENA (**L**ow **E**nergy **N**eutrino **A**stronomy) detector will bring neutrino physics from merely studying neutrinos to using neutrinos as probes to solve questions in astrophysics, cosmology, geophysics and elementary particle physics.

Contents

Chapter 1

Introduction

1.1 Early Experimental Observations of Neutrinos

The measurement of the energy spectrum of electrons from β-decays in the early 20th century can be called the first indirect observation of neutrinos. Without the existence of neutrinos, there were thought to be only two particles in the outgoing channel of the reaction, which would produce a monoenergetic electron as the consequence of energy and momentum conservation. The observed continuous energy spectrum of the electron seemed to violate energy conservation until Pauli in 1930 (see Figure 1.1 on Page 2) proposed a third particle in the outgoing channel of the reaction [PAU 30], a "neutron", as he called it, which would later be called neutrino and placed on a concrete theoretical foundation by Fermi [FER 34].

The first direct observation of neutrinos was made by Cowan and Reines in 1956 ([REI 57], [REI 60], [REI 95]), when they measured $\bar{\nu}_e$ from the Savannah River nuclear reactor via the reaction:

$$\bar{\nu}_e + p \longrightarrow e^+ + n \tag{1.1}$$

with a $CdCl_2$-solution as target. The positron annihilation gammas and the gammas emitted after the delayed capture of the neutron on Cadmium

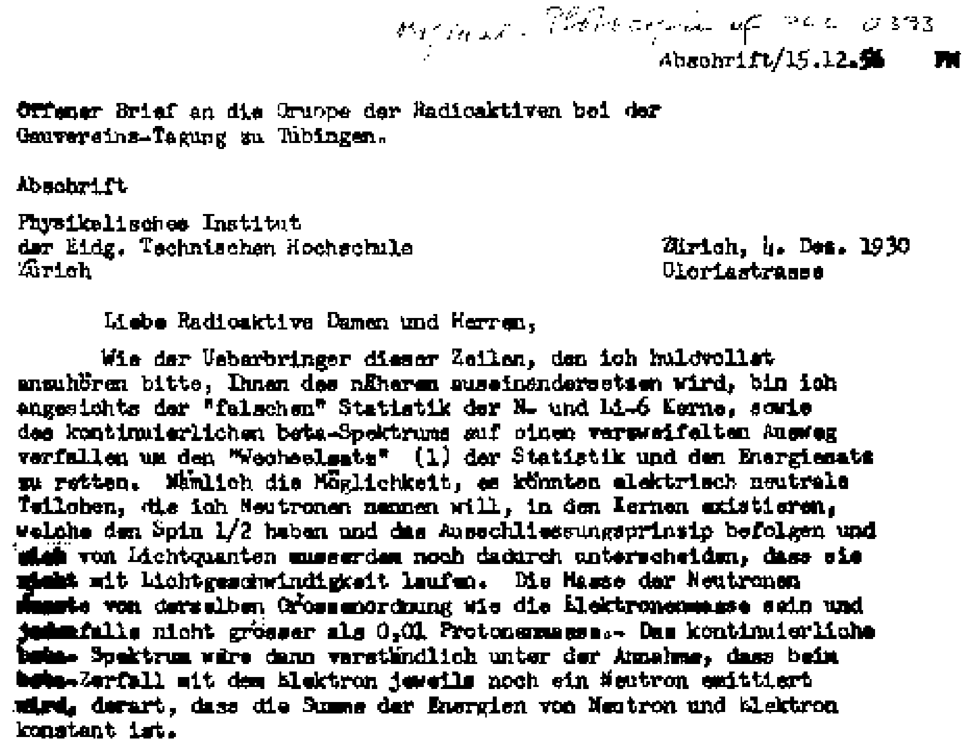

Original. Photocopie of PLC 0393

Abschrift/15.12.56 PM

Offener Brief an die Gruppe der Radioaktiven bei der Gauvereins-Tagung zu Tübingen.

Abschrift

Physikalisches Institut
der Eidg. Technischen Hochschule
Zürich

Zürich, 4. Dez. 1930
Gloriastrasse

Liebe Radioaktive Damen und Herren,

Wie der Ueberbringer dieser Zeilen, den ich huldvollst anzuhören bitte, Ihnen des näheren auseinandersetzen wird, bin ich angesichts der "falschen" Statistik der N- und Li-6 Kerne, sowie des kontinuierlichen beta-Spektrums auf einen verzweifelten Ausweg verfallen um den "Wechselsatz" (1) der Statistik und den Energiesatz zu retten. Nämlich die Möglichkeit, es könnten elektrisch neutrale Teilchen, die ich Neutronen nennen will, in den Kernen existieren, welche den Spin 1/2 haben und das Ausschliessungsprinzip befolgen und sich von Lichtquanten ausserdem noch dadurch unterscheiden, dass sie nicht mit Lichtgeschwindigkeit laufen. Die Masse der Neutronen müsste von derselben Grössenordnung wie die Elektronenmasse sein und jedenfalls nicht grösser als 0,01 Protonenmasse.- Das kontinuierliche beta- Spektrum wäre dann verständlich unter der Annahme, dass beim beta-Zerfall mit dem Elektron jeweils noch ein Neutron emittiert wird, derart, dass die Summe der Energien von Neutron und Elektron konstant ist.

Figure 1.1: Copy of a letter sent by Wolfgang Pauli to a physicists workshop in Tübingen [PAU 30]. The neutrino he proposed was still called “Neutron”.

were detected with liquid scintillator detectors on top of and below the target. Following were the discovery of parity violation in weak interactions by Wu [WU 57] and the measurement of the neutrino helicity by Goldhaber [GOL 58] in 1957/58.

Then, the muon neutrino was discovered in 1961 at the Brookhaven Proton Synchrotron by Ledermann, Schwarz und Steinberger [STE 88]. The first direct measurement of the tau neutrino was made in the year 2000 by the DONUT experiment at Fermilab [KOD 00].

The number of (active) neutrinos can be inferred from the decay width of the Z^0. The Z^0 decays into e^+e^-, $\mu^+\mu^-$, $\tau^+\tau^-$, $q\bar{q}\,(q = u, d, c, s, b)$ and $\nu_\alpha\bar{\nu}_\alpha$. The partial width of the decay into neutrino-antineutrino pairs (*invisible width*) $\Gamma_{\nu\bar{\nu}}$is:

$$\Gamma_{\nu\bar{\nu}} = \frac{1}{12\pi}\frac{G_F}{\sqrt{2}}M_Z^3 N_\nu \tag{1.2}$$

G_F: Fermi coupling constant
M_Z: Z^0 mass
N_ν: Number of (active) neutrinos

Measurements of the total Z^0 decay width and the widths of the visible decay channels at LEP yield an experimental value for N_ν of [HAG 02]:

$$N_\nu = 2.984 \pm 0.008 \tag{1.3}$$

This value is close to the expected number of 3, though it is two sigma low.

The analysis of the cosmic microwave background anistropy as measured by WMAP ([BEN 03], [HIN 03]), yields a limit for the number of additional neutrinos present in the early universe of $\Delta N_\nu < 5.3$ at 95% C.L. with $\Delta N_\nu = N_\nu - 3$ [BAR 03-3]. A better constraint on the number of neutrinos present in the early universe comes from Big Bang Nucleosynthesis (BBN). Here the best-fit result is $\Delta N_\nu = -0.7$ and the upper limit is $\Delta N_\nu \leq 3$ at 95% C.L. [BAR 03-3].

Besides the active types of neutrinos there might also exist sterile neutrinos, which could account for the result of the LSND experiment, see Chapter 1.3.2.

A new era of neutrino physics was entered with the study of solar neutrinos. The neutrinos are produced in nuclear fusion processes in the core of the sun [BET 39], where the dominant part of the energy is produced the so-called pp-chain, see Figure 1.2 on Page 4. Another process, which, according to current solar models [BAH 01] contributes about 1.6% of the total energy production in the sun is the CNO-cycle where ^{12}C acts as a catalyst for the fusion of four protons into helium.

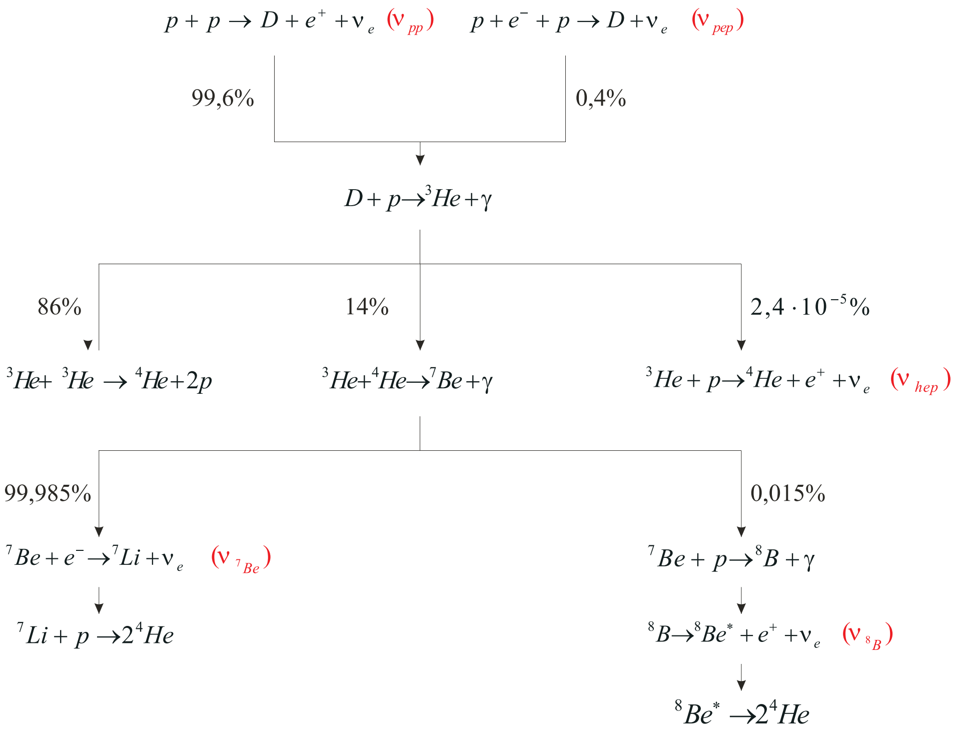

Figure 1.2: The pp fusion chain creates approximately 98.4% of the energy in the sun according to current solar models. The graph illustrates the contributing reactions, their branchings, and the names used to identify the neutrinos from each reaction (in red).

The spectrum of solar neutrinos at the earth contains monoenergetic lines from the ^{7}Be- and pep-neutrinos and continuous spectra from pp-, ^{8}B- and hep-neutrinos from the pp-chain as well as additional continuous contributions of ^{13}N-, ^{15}O- and ^{17}F-neutrinos from the CNO-cycle, see Figure 1.3 on Page 5.

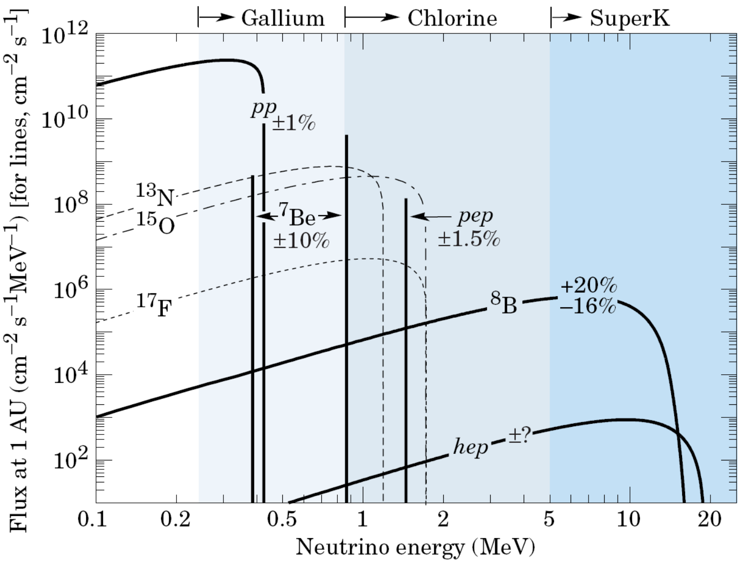

Figure 1.3: The solar neutrino spectrum at the earth, as predicted by the standard solar model. The pp-chain components are plotted with solid lines, the CNO contributions in dotted lines. The energy thresholds for the Gallium and Chloride experiments as well as the Super Kamiokande detector are shown in the top part of the diagram [HAG 02].

The first solar neutrino detector was built in the mid-1960s by Ray Davis in the Homestake gold mine in Lead, South Dakota. It used approximately 615 tons of perchlochethylene C_2Cl_4 as target for the ν_es produced in the sun (see Figures 1.2 and 1.3). The ν_es were detected via the following reaction:

$$\nu_e +^{37}\mathrm{Cl} \longrightarrow^{37}\mathrm{Ar} + \mathrm{e}^- \tag{1.4}$$

The threshold for this reaction is 814 keV (therefore the detector was not sensitive to the dominant part of the solar neutrino spectrum, the pp-neutrinos). The Argon atoms produced within a run of 60 - 70 days were extracted and counted with proportional counters. The measured event rate was ≈ 1/3 of the expected value derived from solar models [DAV 96]. This surprising finding instituted the so-called the “solar neutrino problem”, which lead to a great increase in research in the field of neutrinos and spawned the construction of bigger and more sensitive detectors to investigate this mystery.

The Kamiokande detector [KOS 92] in the Kamioka mine 300 km west of Tokyo is a water Čerenkov detector built in 1983 to measure solar neutrinos via elastic neutrino electron scattering:

$$\nu + \mathrm{e}^- \longrightarrow \nu + \mathrm{e}^- \tag{1.5}$$

The Čerenkov light emitted by the recoil electron in water is detected by 948 photomultipliers which surround the 618 tons of water target. The energy threshold (for the recoil electron) was at first 9.3 MeV, later it improved to 7.5 MeV, i.e. the detector was only sensitive to the high energy part of the solar neutrino spectrum (see Figure 1.3 on Page 5 for the spectrum), the ^{8}B-neutrinos. The measured neutrino flux $\phi_{\mathrm{exp}} = (2.80 \pm 0.19 \pm 0.33) \cdot 10^6\ \mathrm{cm}^{-2}\ \mathrm{s}^{-1}$ [FUK 96] was only $(49 \pm 3 \pm 6)\,\%$ of the flux predicted by solar models [BAH 95]. Though the discrepancy was smaller than the one found by Ray Davis, it was more significant as the errors of the result were smaller.

In the beginning of the 1990s, two experiments started to probe the solar neutrino spectrum at lower energies: GALLEX in the Gran Sasso underground laboratory in Assergi, Italy ([ANS 92], [HAM 96], [HAM 98]) and SAGE in Baksan, Russia ([GAV 89], [ABD 99]). Both experiments use Gallium to capture solar ν_es in the reaction:

$$\nu_e +^{71} \mathrm{Ga} \longrightarrow^{71} \mathrm{Ge} + \mathrm{e}^- \tag{1.6}$$

GALLEX used 101 tons of Galliumchloride ($\mathrm{GaCl_3}$)-solution as target (30.3t of Gallium), SAGE used first 30t and later 57t of liquid Gallium. In both experiments the produced Ge atoms are extracted after each run and then counted in proportional counters via their decay to Ga with a half life of 11.4 days (electron capture):

$$\mathrm{e}^- +^{71} \mathrm{Ge} \longrightarrow^{71} \mathrm{Ga} + \nu_e \tag{1.7}$$

With an energy threshold of 233 keV for the reaction (1.6) the Gallium experiments are sensitive for the pp-neutrinos (see the solar neutrino spectrum in Figure 1.3 on Page 5), a unique feature that at this time. The ν_e-capture rate measured in GALLEX [CRI 99] is $(53 \pm 7)\,\%$ of the expected rate from solar models [BAH 95], in SAGE the measured rate is $(56 \pm 11)\,\%$ [ABD 02] of the expected rate.

The favored explanation for this neutrino deficit, oscillations from one neutrino flavor to another, was first proposed in 1968 by Gribov and Pontecorve [PON 68],[GRI 69]. The proof for this was provided later by the experiments Super Kamiokande, Kamland and SNO (Chapter 1.3.2).

1.2 Neutrino Mixing and Neutrino Oscillations

1.2.1 Neutrino Mixing

In the standard model there are three left-handed neutrinos. They reside in left-handed lepton doublets:

$$L_\alpha = \begin{pmatrix} \nu_{L\alpha} \\ \alpha_L^- \end{pmatrix} \qquad \alpha = e, \mu, \tau \tag{1.8}$$

The standard model neutrinos are massless (as there are only left-handed ν-states) and the lepton numbers L$_e$, L$_\mu$ and L$_\tau$ as well as $L = L_e + L_\mu + L_\tau$ are conserved(see Table 1.1 on Page 7 for the lepton numbers).

	L$_e$	L$_\mu$	L$_\tau$	L		L$_e$	L$_\mu$	L$_\tau$	L
e$^-$	1	0	0	1	e$^+$	-1	0	0	-1
μ^-	0	1	0	1	μ^+	0	-1	0	-1
τ^-	0	0	1	1	τ^+	0	0	-1	-1
ν_e	1	0	0	1	$\bar{\nu}_e$	-1	0	0	-1
ν_μ	0	1	0	1	$\bar{\nu}_\mu$	0	-1	0	-1
ν_τ	0	0	1	1	$\bar{\nu}_\tau$	0	0	-1	-1

Table 1.1: Lepton numbers L$_e$, L$_\mu$, L$_\tau$ and $L = L_e + L_\mu + L_\tau$

In an extension to the standard model, where the neutrinos have mass and the lepton numbers L$_e$, L$_\mu$ and L$_\tau$ are not conserved, the electron muon and tau neutrinos in the lepton doublets (1.8) are flavor eigenstates which relate to the mass eigenstates ν_1, ν_2 and ν_3 with the eigenvalues m_1, m_2 and m_3 via a unitary mixing matrix V [MAK 62]:

$$|\nu_\alpha\rangle = \sum_{k=1}^{n} V^*_{\alpha k}|\nu_k\rangle \quad \alpha = e, \mu, \tau \quad \text{and} \quad k = 1, 2, 3 \tag{1.9}$$

The mixing matrix V can be written as the following matrix product using three rotation angles θ_{12}, θ_{23} and θ_{13} ($0 \leq \theta_i \leq \pi/2$) and three CP-violating phases, a Dirac CP-phase δ and two Majorana CP-phases ϕ_2 and ϕ_3 ($0 \leq \delta, \phi_i \leq 2\pi$) [BAR 03-1]:

$$\begin{aligned} V = &\begin{pmatrix} 1 & 0 & 0 \\ 0 & c_{23} & s_{23} \\ 0 & -s_{23} & c_{23} \end{pmatrix} \cdot \begin{pmatrix} c_{13} & 0 & s_{13}e^{-i\delta} \\ 0 & 1 & 0 \\ -s_{13}e^{i\delta} & 0 & c_{13} \end{pmatrix} \\ &\cdot \begin{pmatrix} c_{12} & s_{12} & 0 \\ -s_{12} & c_{12} & 0 \\ 0 & 0 & 1 \end{pmatrix} \cdot \begin{pmatrix} 1 & 0 & 0 \\ 0 & e^{i\left(\frac{1}{2}\phi_2\right)} & 0 \\ 0 & 0 & e^{i\left(\frac{1}{2}\phi_3+\delta\right)} \end{pmatrix} \end{aligned} \tag{1.10}$$

$$c_{ij} = \cos\theta_{ij}$$
$$s_{ij} = \sin\theta_{ij}$$

1.2.2 Vacuum Oscillations

A neutrino of the flavor ν_α produced in a weak process is described by a coherent superposition of mass eigenstates as shown in Equation (1.9). The state $|\nu_k\rangle$ with mass m_k has the energy E_k:

$$E_k = \sqrt{p^2 + m_k^2} \approx p + \frac{m_k^2}{2p} \tag{1.11}$$

where $|\mathbf{p}| \gg m_i$ is assumed for the approximation. After the production, the mass eigenstates $|\nu_k\rangle$ evolve in time with the phase factors e^{-iE_kt} according to the Schrödinger equation. Using Equation (1.9), after a time t $|\nu_\alpha\rangle$ has evolved to:

$$|\nu_\alpha\rangle_t = \sum_{k=1}^{n} V^*_{\alpha k} e^{-iE_k t} |\nu_k\rangle \tag{1.12}$$

As neutrinos are detected by weak interaction processes, it is convenient to write Equation 1.12 in the basis of the state $|\nu_\beta\rangle$:

$$|\nu_\alpha\rangle_t = \sum_{\beta=1}^{n} \sum_{k=1}^{n} V_{\beta k} e^{-iE_k t} V^*_{\alpha k} |\nu_\beta\rangle \tag{1.13}$$

The probability of the transition $\nu_\alpha \rightarrow \nu_\beta$ is given by:

$$P_{\nu_\alpha \rightarrow \nu_\beta} = \left| \sum_{k=1}^{n} V_{\beta k} e^{-iE_k t} V^*_{\alpha k} \right|^2 \tag{1.14}$$

Using the unitarity relation:

$$\sum_{k=1}^{n} V_{\beta k} V^*_{\alpha k} = \delta_{\alpha\beta} \tag{1.15}$$

and the ultrarelativistic approximation $|\mathbf{p}| \gg m_i$, the transition probability can also be written as:

$$P_{\nu_\alpha \rightarrow \nu_\beta} = \left| \delta_{\alpha\beta} + \sum_{k=2}^{n} V_{\beta k} V^*_{\alpha k} \left(e^{-i\frac{\Delta m^2_{k1} L}{2E}} - 1 \right) \right|^2 \tag{1.16}$$

Δm^2_{ij}:	Mass-squared differences, $\Delta m^2_{ij} = m_i 2 - m^2_j$
L:	Distance of detection point from the point of creation

The oscillation probabilities for antineutrinos can be obtained by switching V and V^*. From Equation (1.16) it can be seen that the probability for the transition $\nu_\alpha \rightarrow \nu_\beta$ depends on the elements of the mixing matrix V, the parameter L/E and the mass-squared differences. Accordingly, all neutrino oscillation experiments are only sensitive to these parameters, i.e. the determination of the absolute neutrino mass and the CP-phases need other experiments. Interesting is also the influence of the mixing angle θ_{13} as seen in Equation (1.10). Any effects of the Dirac CP-phase δ_{CP} will be suppressed by a small θ_{13}, i.e. a large enough θ_{13} is a prerequisite for measuring δ_{CP} in the future, see also Chapter 5 on the future Double Chooz experiment. Exemplary results for the oscillation probabilites $P_{\bar{\nu}_e \to \bar{\nu}_e}$ and $P_{\nu_\mu \to \nu_e}$ are shown in Chapter 5.2.3 and Chapter 5.5, respectively.

1.2.3 Matter Oscillations

When neutrinos propagate through matter they feel a potential due to elastic forward scattering on electrons. As electron neutrinos can interact via charged and neutral current whereas muon and tau neutrinos interact only via the neutral current, their interaction potentials differ. The electron neutrinos have an additional potential contribution

$$A = \pm 2\sqrt{2} G_F n_e E \tag{1.17}$$

G_F: Fermi coupling constant
n_e: Electron density
E: Neutrino energy

compared to ν_μ and ν_τ, where the plus sign is for ν_e and the minus sign for $\bar{\nu}_e$. This additional potential has an effect on the flavor oscillation mechanism when neutrinos propagate [WOL 78], [BAR 80]. In the following, the neutrino oscillations will be illustrated in a two-neutrino framework which is sufficient to understand the mechanism. A complete three-neutrino treatment can be found in [OHL 00]. The Schrödinger equation for neutrino propagation in matter is modified with a term that contains the additional potential A:

$$i \frac{d}{dt} \begin{pmatrix} \nu_\alpha \\ \nu_\beta \end{pmatrix} = \frac{1}{2E} \left[V \begin{pmatrix} m_1^2 & 0 \\ 0 & m_2^2 \end{pmatrix} V^\dagger + \begin{pmatrix} A(t) & 0 \\ 0 & 0 \end{pmatrix} \right] \begin{pmatrix} \nu_\alpha \\ \nu_\beta \end{pmatrix} \tag{1.18}$$

In the case that the matter density is constant, the additional potential $A(t)$ becomes a constant, A. The solution of Equation 1.18 can then be obtained by diagonalisation which leads to a form equivalent to vacuum oscillations, but with new parameters Δm_m^2 and θ_m (with the subscript m for matter), which are derived from the the vacuum parameters as follows:

$$\Delta m_m^2 = \Delta m^2 \sqrt{\left(\frac{|A|}{\Delta m^2} \mp \cos 2\theta\right)^2 + \sin^2 2\theta} \tag{1.19}$$

and

$$\sin^2 2\theta_m = \frac{\sin^2 2\theta}{\left(\frac{|A|}{\Delta m^2} \mp \cos 2\theta\right)^2 + \sin^2 2\theta} \tag{1.20}$$

In Equations (1.19) and (1.20) the minus sign refers to neutrinos and the plus sign to antineutrinos. It can be inferred from Equations (1.20) and (1.17) that the mixing angle θ_m has a maximum when

$$\sqrt{2} G_F n_e = \frac{\Delta m^2}{2E} \cos 2\theta \tag{1.21}$$

This resonant behavior was first pointed out by Mikheyev, Smirnov and Wolfenstein ([MIK 85], [MIK 86],[WOL 78]) and has therefore been named MSW effect. In case the resonance condition from Equation (1.21) is fulfilled any mixing angle θ is amplified to $\theta_m = \pi/4$, i.e. $\sin^2 2\theta_m = 1$ and mixing becomes maximal.

This is especially important in the case of solar neutrinos. Here, the neutrinos travel from their production point in the core of the sun to the outside of the sun through matter with monotonously decreasing electron density n_e. If, along the way, the resonance condition (1.21) is met, the flavor transition probability for the neutrino is resonantly enhanced. As it can be seen from Equation (1.21), with smaller neutrino energy E, a higher electron density n_e is needed to fulfill the resonance condition. With the electron density present in the core of the sun, the high energy ^{8}B neutrinos (see Figure 1.3 on Page 5) meet the resonance condition on their way through the sun, and therefore have a strongly enhanced disappearance probability ($\approx 2/3$), whereas the lower energy ^{7}Be neutrinos do not meet the resonance condition and their disappearance probability is only $\approx 1/3$. This will be an interesting feature to be measured in the solar neutrino spectrum by Borexino, see Chapter 2.

1.3 The Current Status of Neutrino Physics

1.3.1 The Neutrino Masses

Neutrinos have been proven to be massive particles by the existence of neutrino oscillations (see Chapter 1.2 and Chapter 1.3.2 for the experimental results.) Only if neutrinos have mass, neutrino mixing and neutrino oscillations can occur. But as it was shown in Chapter 1.2.2, the transition probabilities for neutrino oscillations only depend on the mass-squared differences Δm^2, i.e. neutrino oscillations cannot give any information about the absolute neutrino masses.

The most successful technique so far for probing the absolute neutrino mass is to analyze the endpoint region of the electron spectrum in the β-decay of tritium. A nonzero neutrino mass will suppress the spectrum at the highest energies. The experiments could determine then the effective neutrino mass [MCK 80], [HOL 92]:

$$m_\beta^2 = \sum |V_{ei}|^2 m_i^2 \tag{1.22}$$

where V refers to the mixing matrix from Equation (1.9). The most stringent limits for m_ν come from the Troitsk experiment in ([LOB 01], [LOB 02]) and the Mainz experiment [WEI 02]. They both achieved a limit for the neutrino mass of $m_\beta < 2.2$ eV (at 95% C.L.). The future Katrin (**Ka**rlsruhe **Tri**tium **N**eutrino) experiment ([OSI 01], [BOR 03]), which will start to measure in 2007 plans to lower this limit down to $m_\beta = 0.35$ eV by increasing the energy resolution compared to the Mainz experiment.

A limit on the sum of the neutrino masses $\sum m_\nu$ was found by the by analyzing the anisotropy of the cosmic microwave background as measured by the WMAP (**W**ilkinson **M**icrowave **A**nisotropy **P**robe) collaboration ([BEN 03], [HIN 03]) in conjunction with data from the Two Degree Field Galaxy Redshift Survey ([COL 01], [PER 01]) and the Sloan Digital Sky Survey SDSS ([YOR 00]) The value reported in [BAR 03-2]is $\sum m_\nu \leq 0.75$ eV at 95% C.L. and $\sum m_\nu \leq 1.1$ eV at 99% C.L.

Another way to access the neutrino mass is the search for the neutrinoless double beta decay ($0\nu\beta\beta$-decay), provided that neutrinos are Majorana particles, i.e. neutrino and antineutrino are identical particles. In the $0\nu\beta\beta$-decay, a virtual right-handed antineutrino is created in one vertex and then absorbed as a left-handed neutrino. The interaction rate of the $0\nu\beta\beta$-decay depends on the effective neutrino mass [WOL 81]:

$$M_{ee} = \left| \sum V_{ei}^2 m_i \right| \tag{1.23}$$

Equation (1.23) describes a coherent sum over all mass eigenstates. As the matrix elements V may contain complex elements, cancellation in the sum might occur, in contrast to the effective mass for the β-decay (see Equation (1.22)). The best limits on M_{ee} come from the experiments Heidelberg-Moscow (in the Gran Sasso underground laboratory) [GUN 97] and IGEX [AAL 99]. Both experiments use large enriched ^{76}Ge-detectors. The mass limit reported form the Heidelberg-Moscow collaboration is $M_{ee} < 0.35$ eV at 90% C.L. [KLA 00], but due to uncertainties in the nuclear matrix elements an overall uncertainty of a factor 3 is attributed to this result ([FAE 99], [ELL 02]). The limit reported from IGEX is $M_{ee} < 0.33$ - 1.35 eV [AAL 02-1]. A part of the Heidelberg-Moscow collaboration has reported the detection of neutrinoless double beta decay with $M_{ee} = 0.39$ eV, however this result is still controversial and not yet generally accepted ([AAL 02-2], [KLA 02]). New experiments are planned which will either confirm this result or further increase the limit of sensitivity to at least 50 meV. These experiments include CUORE [ARN 03] (using ^{130}Te), XMASS [MOR 03] (using ^{136}Xe), EXO [WAM 02] (using ^{136}Xe), Gerda [ABT 04] (using ^{76}Ge), Majorana [AAL 02-3] (using ^{76}Ge) and MOON [EJI 03] (using ^{100}Mo).

1.3.2 Neutrino Oscillations - Experimental Results

Neutrino Oscillations provide the solution to the solar neutrino problem as detailed in Chapter 1.1, i.e. depending on the experiment, a suppression of the solar electron neutrino flux at the earth between 1/3 to 1/2 compared to the expectations from solar models. It was problematic though, that every experiment that measured the reduction in the solar neutrino flux had to rely on solar models which provide the numbers for the expected neutrino flux. The solar neutrino experiment SNO (**S**udbury **N**eutrino **O**bservatory) [BOG 99] however is the first experiment which was able to measure the reduction in the flux of electron neutrinos directly, as it also measured the total active neutrino flux via a neutral current reaction. Therefore, with the SNO experiment, the evidence for neutrino oscillations became more robust.

SNO is a water Čerenkov detector which uses 1000 tons of heavy water D_2O as target. The heavy water target allows detection of neutrinos via the following reactions:

$$\text{Charged Current:} \quad \nu_e + d \rightarrow e^- + p + p \quad \text{(CC)} \tag{1.24}$$

$$\text{Neutral Current:} \quad \nu_x + d \rightarrow \nu_x + n + p \quad \text{(NC)} \tag{1.25}$$

$$\text{Elastic Scattering:} \quad \nu_x + e^- \rightarrow \nu_x + e^- \quad \text{(ES)} \tag{1.26}$$

A flavor transition from ν_e to ν_μ or ν_τ can be observed by comparing the interaction rates measured for the charged current reaction (CC) and the neutral current reaction (NC):

$$\frac{CC}{NC} = \frac{\Phi\left(\nu_e\right)}{\Phi\left(\nu_e + \nu_\mu + \nu_\tau\right)} \tag{1.27}$$

An excess in the neutral current rate is therefore due to a ν_μ or ν_τ component in the solar neutrino flux, which must be due to a flavor transition as only ν_e are produced in the sun. The results reported from SNO are (in units of $10^6 \text{cm}^{-2}\text{s}^{-1}$) [AHM 03]:

$\phi_{CC} = 1.59^{+0.08}_{-0.07}$ (stat) $^{+0.06}_{-0.08}$ (syst)
$\phi_{ES} = 2.21^{+0.31}_{-0.26}$ (stat) ± 0.21 (syst)
$\phi_{NC} = 5.21 \pm 0.27$ (stat) ± 0.38 (syst)

These values represent the flux of solar ^{8}B neutrinos due to the energy threshold of 5.5 MeV, only a very small contribution from HEP neutrinos of 0.5% according to solar models could be present also, see Figure 1.3 on Page 5 for the solar neutrino spectrum. The measured neutral current flux of ^{8}B neutrinos agrees with the flux expected from solar models [BAH 01]: $\phi_{SSM} = 5.05^{+1.01}_{-0.81}$. The ratio of the ^{8}B flux measured with the CC and the NC reaction is [AHM 03]:

$$\frac{\phi_{CC}}{\phi_{NC}} = 0.306 \pm 0.026(\mathrm{stat}) \pm 0.024(\mathrm{syst}) \tag{1.28}$$

In addition, the SNO experiment has presented an indication for a day-night asymmetry in the CC rate [AHM 02-2], which is due to oscillation effects as the neutrinos cross the earth ([BAR 01], [MAR 02]).

The Kamland eperiment [PIE 01] is a 1000 ton liquid scintillator detector in the Kamioka mine in Japan. It is located at a distance of 150 - 210 Km to several nuclear power plants. Kamland measures the flux and energy spectrum of the electron antineutrinos emitted by these reactors. Antineutrinos are detected in Kamland via the inverse beta decay reaction:

$$\bar{\nu}_e + p \longrightarrow e^+ + n \tag{1.29}$$

with an energy threshold of 1.8 MeV for the $\bar{\nu}_e$. Kamland measured a survival probability of the $\bar{\nu}_e$ of [ARA 04]:

$$P_{\bar{\nu}_e \to \bar{\nu}_e} = 0.601 \pm 0.069(\mathrm{stat}) \pm 0.042(\mathrm{syst}) \tag{1.30}$$

In addition to measuring the disappearance of electron antineutrinos, Kamland also found an energy dependance of the effect which matches beautifully with the expectations from neutrino oscillations, see Figure 1.4 on Page 16.

Another important information about neutrino oscillations comes from the observation of atmospheric neutrinos by the Super Kamiokande ([FUK 98-1], [FUK 98-2]) experiment, a 50,000 ton water Čerenkov detector in the Mozumi mine in Kamioka-cho, Japan and an upgrade of the Kamiokande detector ([ARI 86], [KAJ 86]), which was originally built to study proton decay.

Cosmic rays produce pions and kaons when they interact with the atmosphere, these decay and produce electron and muon neutrinos and their antineutrinos:

$$\pi^+, K^+ \to \nu_\mu \mu^+ \to \nu_\mu e^+ \nu_e \bar{\nu}_\mu \tag{1.31}$$

$$\pi^-, K^- \to \bar{\nu}_\mu \mu^- \to \bar{\nu}_\mu e^- \bar{\nu}_e \nu_\mu \tag{1.32}$$

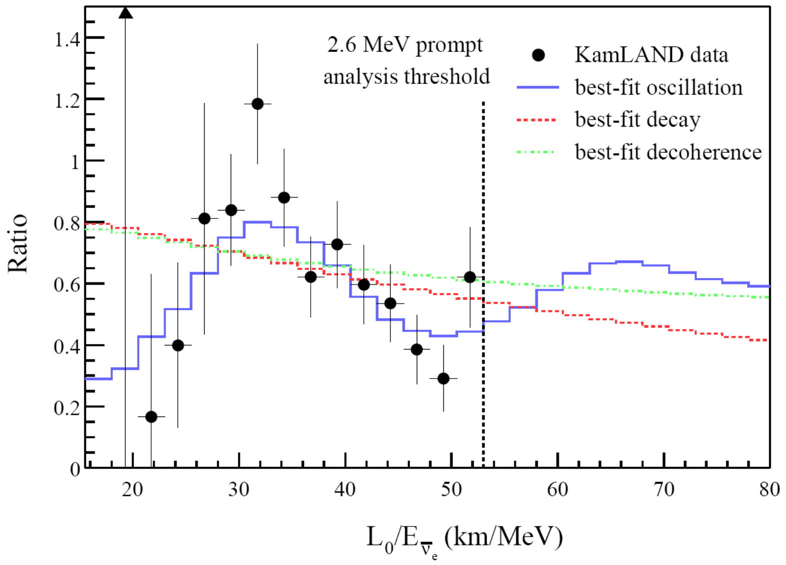

Figure 1.4: Ration of the observed $\bar{\nu}_e$-spectrum to the expectation for no oscillations versus L/E in Kamland. The blue curve is the expectation for neutrino oscillations with the best fit oscillation parameters [ARA 04].

At energies above 1 GeV there are twice as many muon neutrinos as electron neutrinos. Due to its nature as a Čerenkov detector, Super Kamiokande is able to measure the direction of the incoming neutrino. Neutrinos produced in the atmosphere travel between 15 Km and up to $\approx$ 13,000 Km, depending on their zenith angle. The ratio of observed to expected neutrinos is a sensitive probe to neutrino oscillations as different pathlenghths L and neutrino energies E can be studied. Already the Kamiokande detector, which was at $\approx$ 2100 tons target mass considerably smaller than Super Kamiokande (with a fiducial mass of 22.5 kt), observed a lack of muon neutrinos compared to the theoretical expectation ([HIR 88], [HIR 92]). The zenith angle distributions measured by Super Kamiokande for electron-like and muon-like events agree with neutrino oscillations, see Figure 1.5 on Page 17.

Recently, a dip in the [ASH 04] muon neutrino survival probability as a function of the neutrino flight pathlength L over the neutrino energy E was found, which is furhter evidence for neutrino oscillations as other models like neutrino decay do not predict this spectral feature.

Both the Soudan-2 ([ALL 96], [ALL 99], [SAN 03]) and MACRO ([AMB 98],

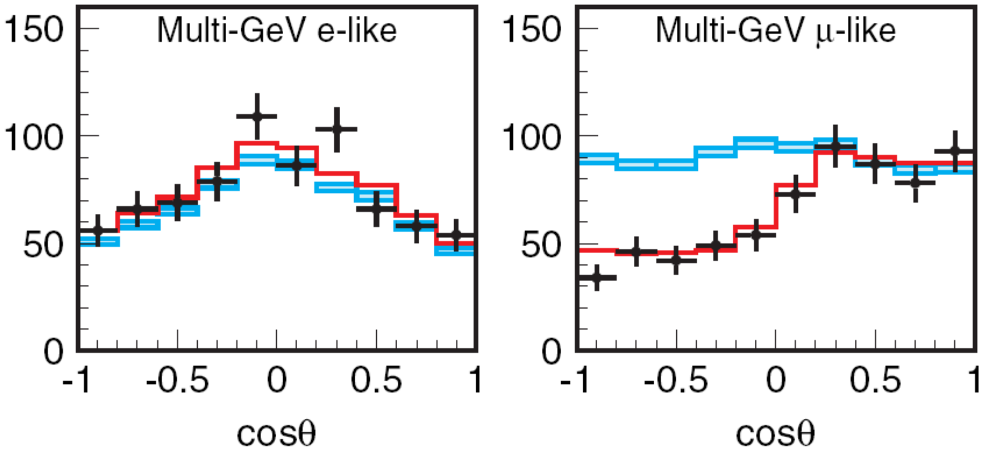

Figure 1.5: Zenith angle distributions for contained e-like and μ-like atmospheric neutrino events in Super Kamiokande [KEA 04]. $\cos\theta = 1$ corresponds to downward events with L $\approx$ 15 km and $\cos\theta = -1$ corresponds to upward events with L $\approx$ 13,000 km. The blue lines show the best fits without oscillations and the red lines with oscillations.

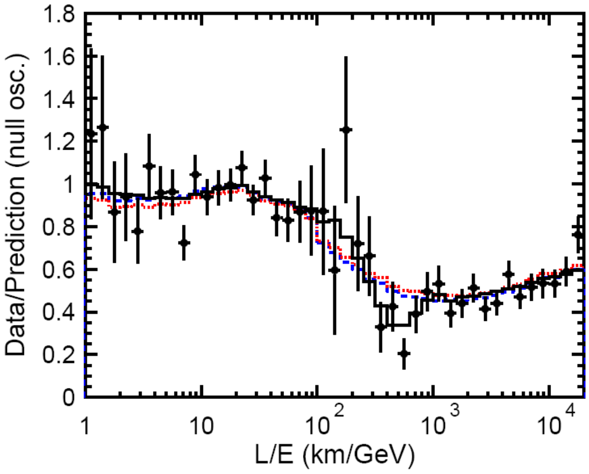

Figure 1.6: Muon neutrino survival probability as a function of L/E measured by Super Kamiokande [ASH 04]. The characteristic dip at $\approx$ 500 km/GeV is predicted by neutrino oscillations, the black line shows the best oscillation fit.

[AMB 00], [AMB 01], [AMB 03]) experiments have also measured atmospheric neutrinos and the oscillation parameters are consistent with the Super Kamiokande result.

The K2K experiment [AHN 01], in which ν_μ with energies of typically ≈ 1.4 GeV are directed from KEK to Super Kamiokande (L = 250 km), has measured a ν_μ survival probability consistent with the atmospheric neutrino results, $P_{\nu_\mu \to \nu_\mu} = 0.70^{+0.11}_{-0.10}$ [AHN 02].

The results from all the neutrino experiments to date (solar, atmospheric, accelerator and reactor neutrinos) are consistent with the 3-neutrino oscillation model as described in Chapter 1.2 (all experiments but LSND, see Page 18). Although the oscillation parameters can be derived from different experiments, the most precise results come from combined analyses of all the accumulated data including the results from the Gallium experiments. The combined analysis from Kamland and the solar neutrino experiments yields at 90% C.L. [ARA 04]:

$$\Delta m^2_{12} = 7.9^{+0.6}_{-0.5} \cdot 10^{-5} eV^2$$
$$\tan^2\theta_{12} = 0.40^{+0.10}_{-0.07}$$

The latest analysis of the Super Kamiokande data yields at 90% C.L. [ISH 04]:

$$\Delta m^2_{23} = 2.4^{+0.6}_{-0.5} \cdot 10^{-3} eV^2$$
$$\sin^2 2\theta_{23} = 1^{+0}_{-0.1}$$

The remaining mixing angle θ_{13} has not been measured yet. The best limit comes from the Chooz reactor antineutrino experiment ([CHO 98], [CHO 99], [CHO 00] and [CHO 03]), see also Chapter 5 on the new Double Chooz experiment:

$$\sin^2 2\theta_{13} < 0.2 \text{ at } 90\% \text{ C.L.}$$

As it was already mentioned, the LSND eperiment ([ATH 96], [AGU 01], [ATH 97]), produced a result which is not consistent with the 3 neutrino oscillation scheme. LSND found evidence for $\bar{\nu}_\mu \to \bar{\nu}_e$ oscillations at 3.3 σ, which corresponds to [AGU 01] (best-fit values):

$$\Delta m^2_{LSND} = 1.2 \text{ eV}^2$$
$$\sin^2 2\theta_{LSND} = 0.003$$

A large Δm^2 however does not agree with other experiments in a 3 neutrino oscillation scheme, as there are only 2 mass differences between 3 neutrinos and these have already been constrained to much smaller values, see above. Possibly the introduction of a fourth neutrino could solve this discrepancy, although 4 neutrino models can not fit all the current data convincingly ([OKA], [BAR 98], [MAL 02]). This fourth neutrino can not take part in the decay of the Z^0, as the measurement of the Z^0-width shows, see Chapter 1.1, therefore it is called *sterile* neutrino. In addition, most of the LSND allowed region in the $\sin^2 2\theta - \Delta m^2$ parameter space is excluded by the KARMEN experiment ([EIT 00], [ARM 02]). The future Mini-BooNE experiment ([STA 00]) will probe the whole region of the LSND evidence.

1.4 Open Questions

Although there has been a dramatic increase in the understanding of neutrino physics in the last years, neutrinos are still far from being fully understood. The most outstanding questions to be addressed in future experiments will be:

- **What is the flux of solar ^{7}Be, pep and CNO-cycle neutrinos and what is the precise pp-neutrino flux?** Here, the Borexino detector (see Chapter 2) as well as Kamland (see Chapter 1.3.2) could give the answer for the ^{7}Be-neutrinos. Future high precision experiments like LENS [SCH 00] might improve the precision on the pp-flux measurement.

- **What is the value of θ_{13}?** The Double Chooz experiment or future accelerator experiments might measure θ_{13}, see Chapter 5.

- **What are the exact values of the mixing angles θ_{12} and θ_{23}?** The future NUMI accelerator experiment might improve the current precision, see Chapter 5.5.

- **What are the absolute masses of the neutrinos?** This could be addressed by more sensitive beta-decay experiments or by the measurement of neutrinoless double beta decay, see Chapter 1.3.1.

- **Are neutrinos Majorana or Dirac particles?** This could be resolved by confirming the evidence of neutrinoless double beta decay (see Chapter 1.3.1).

- **What is the value of the Dirac CP phase δ_{CP}?** The possibility of a measurement depends on the size of θ_{13}, as detailed in Chapter 1.2.2.

- **What information can neutrinos give us about cosmology, astrophysics and geophysics?** Neutrinos can be probes to study supernovas, the star formation history of the universe and even the radioactivity in the Earth's crust. These topics will be adressed in Chapter 6.

Chapter 2

The Borexino Detector

Borexino is an experiment dedicated to rare-event neutrino physics at low energies, i.e. in the sub-MeV range. It is located in the Laboratori Nazionali del Gran Sasso, in Assergi, Italy, with a rock overburden of approximately 1300 m, equaling 3600 m.w.e. shielding [ALI 02].

Borexino is designed for real time solar neutrino spectroscopy via elastic neutrino electron scattering. Of main interest is the measurement of the solar ^{7}Be-neutrinos (see Figure 1.3 on Page 5). A determination of the solar ^{7}Be-ν flux with an accuracy of 10 % would allow the determination of the pp-ν flux with an error of less than ≈ 1 % [BAH 03], when using the known oscillation parameters and the solar luminosity. This would allow a precise measurement of the thermonuclear fusion processes inside the sun (see Figure 1.2 on Page 4). In addition, the measurement of the ^{7}Be-ν flux would allow a confirmation of the presence of matter effects in solar neutrino oscillations. Whereas the disappearance probability for the ^{8}B electron neutrinos measured by SNO is $\approx 2/3$ (the oscillation in this energy regime is dominated by matter effects in the sun), the disappearance probability for ^{7}Be electron neutrinos would be reduced to $\approx 1/3$ (at this energy matter effects become negligible), a spectral feature which could be seen when measuring the ^{7}Be-ν flux with Borexino. In addition, Borexino is expected to be able to measure pep-neutrinos and neutrinos form the CNO-cycle (if the cosmogenic background does not turn out to be worse than expected), which until now have only been measured as an integral part of the low energy solar neutrino flux in the Gallium experiments GALLEX and SAGE (see Chapter 1.1). The measurement of geo-ν's form the Earth's crust and supernova-ν's will also be possible with Borexino. Geo- and supernova-ν's will be discussed in Chapter 6. It is also foreseen to probe the magnetic moment of the neutrino with an artificial ν-source at Borexino. An enhancement of the neutrino interaction cross section due to the magnetic moment could be detected in this way. Finally, reactor neutrinos measured with Borexino will allow to test the oscillation parameters.

Target as well as the detection medium are $\approx$ 300 t of a liquid scintillator. It consists of the solvent pseudocumene (1-2-4 Trimethylbenzene) with about 1.5 g/l PPO (2,5-Diphenyloxazole) added to it. The light yield of this scintillator is $\approx 10^4$ photons for a beta-particle which deposits an energy of 1 MeV. The light is detected by photomultipliers (PMs) with their sensitivities matched closely to the maximum of the light emission spectrum which is at $\approx$ 390 nm. The chosen PPO concentration ensures large absorption lengths in the interesting wavelength region [ALI 00].

Borexino has a water tank with a diameter of 18 meters, containing a 13.7 meter diameter stainless steel sphere (SSS), see Figure 2.1 on Page 23. There are two nylon vessels located concentrically within the SSS. The inner vessel (IV) holds the scintillator, the 11 meter diameter outer vessel (OV) acts as a radon barrier to prevent diffusion of ^{222}Rn into the scintillator. ^{222}Rn is produced in the radioactive decay of ^{226}Ra, which occurs in various parts of the detector despite rigorous cleaning procedures and material selection. On the inside of the SSS are 2200 photo multiplier tubes (PMTs), 1840 of which are equipped with aluminum light guides, see Chapter 3.

Borexino detects solar ^{7}Be neutrinos by measuring the scintillation light produced by the recoil electron after elastic scattering of the neutrino on an electron. The mono-energetic 0.862 MeV ^{7}Be neutrino creates a Compton-like recoil spectrum with energies in the range 0 - 0.66 MeV.

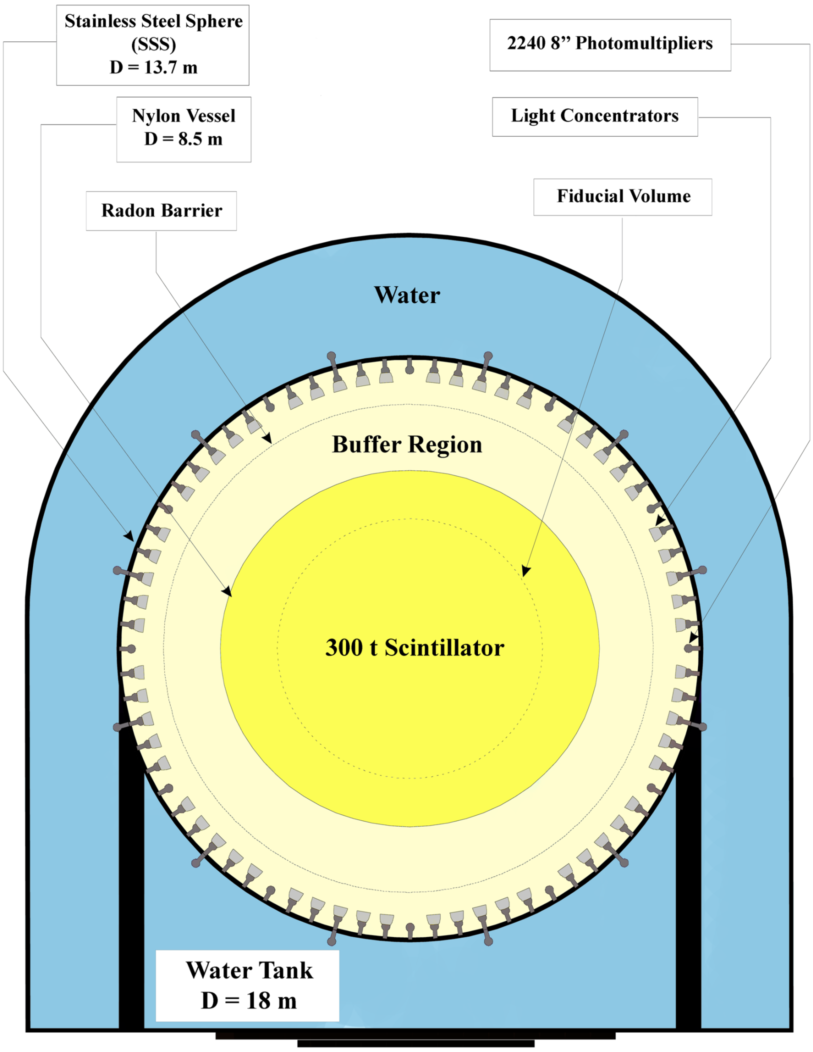

Figure 2.1: Schematics of the Borexino detector. 300 tons of scintillator are surrounded by 1100 tons of pseudocumene buffer and 2200 tons of ultrapure water shield on the outside. Borexino is equipped with 2214 photomultipliers.

Chapter 3

Light Guides for Borexino and the CTF

3.1 Motivation and Requirements

In the design of the Borexino detector (see Chapter 2) achieving the highest possible light yield was a main goal. The light yield is the total number of photo electrons generated by all photomultipliers per unit of deposited energy, usually given as $\frac{N}{E[MeV]}$ (also called photoelectron yield). A high light yield is crucial for the following reasons:

- Energy resolution

  It is not possible to tag the neutrino signal in Borexino. The signature of the ^{7}Be recoil spectrum is a step like function at the highest possible recoil energy of 660 keV, see Figure 3.1 on Page 27. A good energy resolution is needed to make this step function visible against background events. The number of photoelectrons created is proportional to the energy deposited in the scintillator, $N \propto E$. The statistical error on the number is the square root of N, therefore the statistical limit to the energy resolution is proportional to the square root of the number of created photoelectrons:

  $$\frac{\Delta E}{E} \propto \sqrt{N} \tag{3.1}$$

- Position reconstruction

  Borexino will use position reconstruction of events. The time of flight of photons to the different photomultipliers can be used to determine the location of the event inside the Inner Vessel. Using this position information for each event, a so called “Fiducial Volume” of $\sim$ 100t can be defined, and all events outside this Fiducial Volume will be rejected. This technique reduces the effective target mass, but at the same time it increases the shielding of the detector. The by far dominant part of the external background events can be rejected in this way. These external background events are caused by higher energy gamma rays ($>$ 1 MeV) with enough penetration strength to pass through the buffer volume. Those gamma rays can be created by gamma decays in the environment of the detector, e.g. the rock surrounding the laboratory or inside the detector by various radioactive components like the photomultipliers or even the light guides. The resolution of the position reconstruction scales with the square root of the number of photoelectrons measured. Therefore, a high light yield is needed to obtain a good rejection factor for the external background.

- Alpha/Beta discrimination

  Alpha decays from isotopes in the Uranium and Thorium chains inside the Inner Vessel are a not negligible background in Borexino. Although the energies of the alpha particles are typically several MeVs, the visible energy deposition in the scintillator falls into the interesting region for solar ^7Be neutrino detection (between 250 keV and 800 keV [ALI 02]) due to “quenching” of the signal. Quenching means that the light output for alpha particles is reduced by a factor of $\sim$ 10, compared to electrons. These alpha decays can be identified though through analysis of the pulse shape. The efficiency of this pulse shape discrimination depends strongly on the number of photoelectrons, and therefore a high light yield helps in reducing the background in Borexino.

The result of these considerations is that the optical coverage in Borexino needs to be as high as possible. Yet the total number of photomultipliers cannot be increased above the number that is installed now ($\approx$ 2200, see Chapter 2) due to the fact that they contribute to the external background. The concentration of radioactive isotopes from the Uranium and Thorium

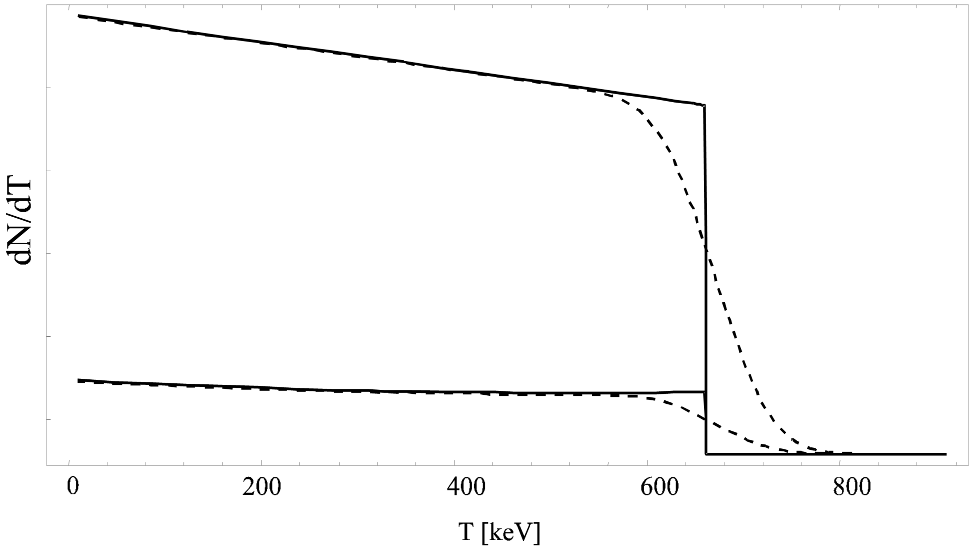

Figure 3.1: The recoil energy spectrum for elastic scattering of the monoenergetic ^{7}Be neutrinos (the dominant 862 keV line). The top solid line is for electron neutrinos, the lower one for muon neutrinos. The dashed lines show the spectra if Borexino's energy resolution is taken into account.

chain and also ^{40}K in the photomultipliers leads to an expected background of 0.15 counts/day in the in the neutrino window between 250 keV and 800 keV [CAD 01]. To increase to optical coverage with the same number of photomultipliers it was decided to use light guides. These are mirrors that increase the area of photon acceptance of the photomulitpliers, see Figure 3.2 on Page 28 and Figure 3.3 on Page 29. Of course, the same considerations on the radioactvie background that limit the number of photomultipliers also apply to the light guides. Already in the Borexino prototype detector, the CTF [ALI 98-1], light guides have been used. Their shape and material differ from the Borexino light guides due to the different detector geometry and environment. Whereas in Borexino the light guides are immersed in Pseusocumene, an organic solvent, in the CTF they are immersed in deionized water.

In summary, the most important specifications for the concentrators in Borexino are:

- highly efficient and uniform light collection from the scintillator region

- low background contribution in the energy spectrum of solar neutrinos
- long term stability against corrosion of other deterioration in either PC or deionized water as environmental medium

The light guides for for Borexino as well as for the CTF have been optimized to meet these requirements.

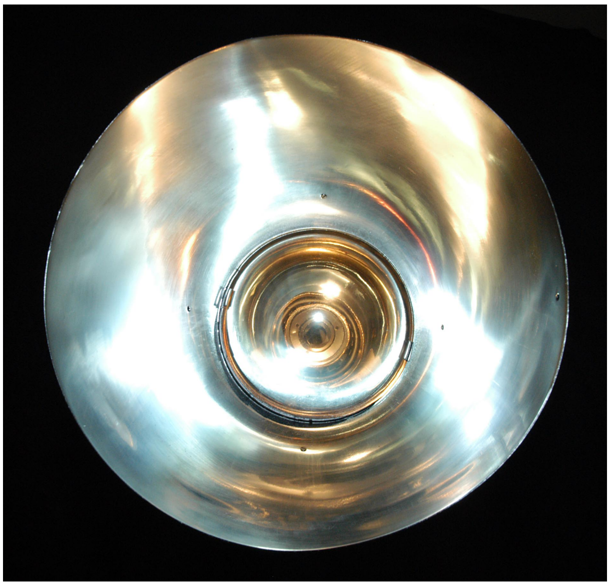

Figure 3.2: A Borexino light guide. The mounted photomultiplier can be seen in the opening in the back. The front aperture has a diameter of 30.1 cm

3.2 Shape of the Light Guides

The shapes of the light guides for Borexino and the CTF have been designed with the so called “string method” [WEL 89]. Their profile has been optimized to collect the light from the scintillator vessel uniformly.

3.2.1 The Borexino Light Guides

In the Borexino geometry, where the scintillator vessel has a diameter of 8.5 m and the front of the photomultiplier is 6.52 m from the center of

Figure 3.3: A CTF light guide. The mounted photomultiplier can be seen in the opening in the back. The front aperture has a diameter of 50.6 cm.

the detector, a photon emitted in the scintillator region can enter the light guide at all angles between zero degrees and the maximum angle δ_{max}, where $\delta_{max} \approx 41°$. If a photon enters the light guide at an angle $\delta < \delta_{max}$, it will hit the photo cathode after not more than one reflection on the light guide, see Figure 3.4 on Page 30. The light guides are designed so that photons originating from outside the scintillator vessel will not hit the photo cathode. The maximum angle of acceptance of the light guides δ_{max} has been chosen to be 44 degrees, that means it is a little bit bigger than necessary which allows for small misalignments of the light guides when mounted in the detector.

The profile of the light guides is designed using a string with constant length. One end of the string is fixed to an extreme point of the scintillator vessel, the other end to an extreme point of the photo cathode, see Figure 3.5 on Page 31. When the string is pulled to the other extreme point of the photo cathode it should be taut, which determines the length of the string. The string now consists of a straight section and two arches. By moving the other extreme point (point p in Figure 3.5) upwards while keeping the string taut one can draw the shape of the light guide.

A light ray which is tangential to the scintillator vessel is reflected on the light guide in such a way that is tangential also to the photo cathode, see Figure 3.4 on Page 30.

Whereas a parabolic mirror would focus the light emitted from the sperical scintillator vessel on a focal point, the light guides collect the incoming light uniformly on the photo cathode.

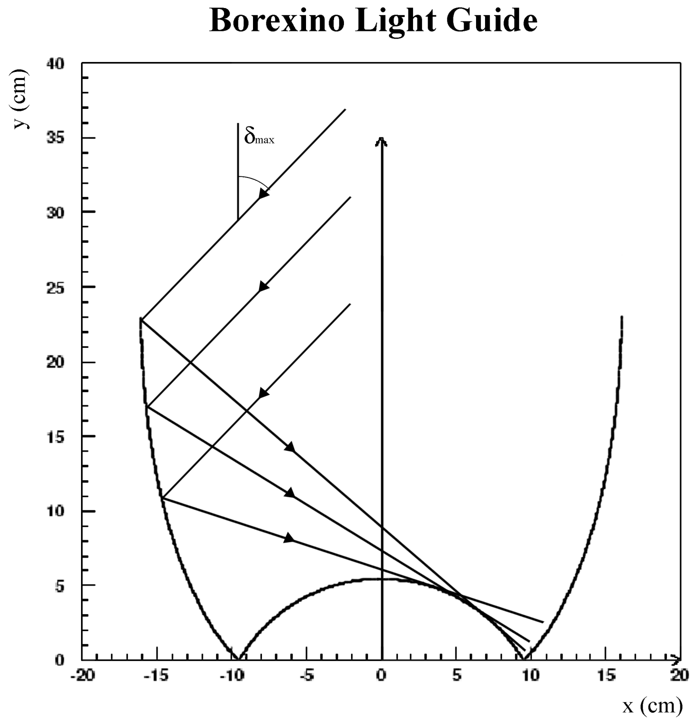

Figure 3.4: String Cone for Borexino. The radii of the entry and exit apertures are 15.5 cm and 9.5 cm respectively. The length of the light guide is 25.5 cm. The manufactured concentrators have been shortened to a height of 23 cm for technical reasons, see text. The critical angle of incidence is $\delta_{max} = 44^o$. For angles of incidence greater than δ_{max} the light will be reflected. The geometrical amplification factor of the concentrator in the Borexino case is 2.9.

The string method shown in Figure 3.5 on Page 31 is a two dimensional approximation of the three dimensional case. It could be shown that the three dimensional case works very well also. The light collection efficiency of

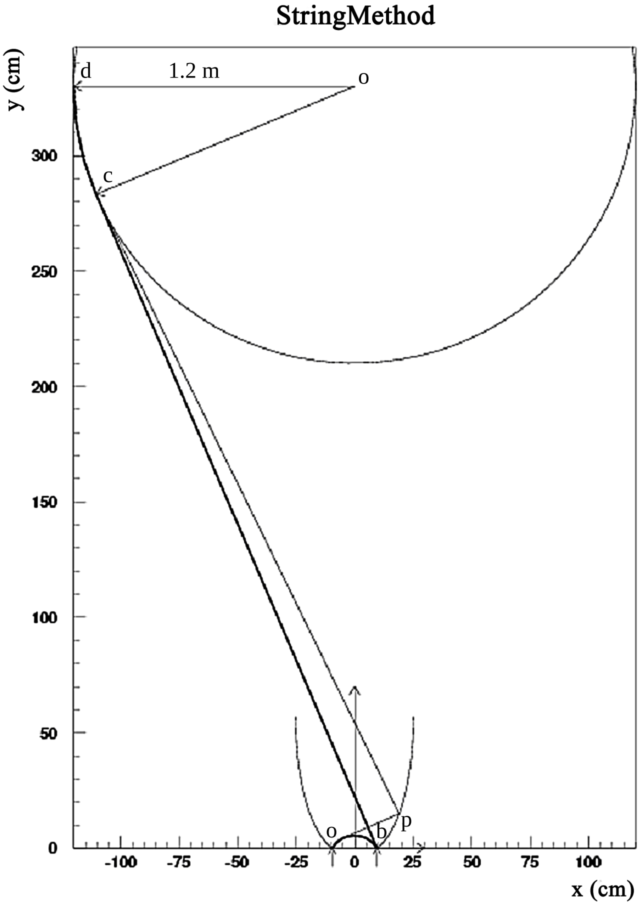

Figure 3.5: This figure illustrates the string method for constructing the shape of the concentrator (see text). A light ray that originates at the edge of the scintillator vessel is reflected at point p ant hits the photomutliplier cathode tangentially. This example shows a CTF light guide. The geometrical amplification factor in this case is ≈ 10.

the Borexino light guide as a function of the angle of incidence δ has been determined in a Monte Carlo calculation, see Figure 3.6 on Page 33. An average reflectivity of 86% was assumed for the light guide's surface (polished aluminum in the Borexino case) in this calculation. With this number for the reflectivity, the collection efficiency of the light guide was ≈ 0.88, which is also the experimentally determined value.

Also, in the three dimensional case a photon might need more than one reflection on the light guide to be directed onto the photo cathode. The average number of reflections has been calculated in a Monte Carlo simulation for the three dimensional case and the result is shown in Figure 3.7 on Page 34. It can be seen that the deviation from the two dimensional model is minor.

The Borexino light guides differ slightly from the calculated ideal shape. They should become slightly thinner towards their opening, yet this would have double the cost for the spinning process in which they were formed. It was decided to cut them at the point of their maximum diameter, and thus reducing their length by 1.5 cm. This resulted in a loss in light yield of only 2.25%.

The geometric amplification factor f_G for the Borexino light guides is 2.9. It is defined as the ratio of the covered solid angle of the photomultiplier with mounted light guide and without light guide:

$$f_G = \frac{\Theta_{lightguide}}{\Theta_{bare}} = \frac{\frac{R^2\pi}{4\pi(d-h)^2}}{\frac{r^2\pi}{4\pi d^2}} = \frac{R^2 d^2}{r^2\,(d-h)^2} \tag{3.2}$$

R: the radius of the light guide's entry aperture
r: the radius of the photo cathode
d: the distance of the photo cathode from the center of the scintillator vessel
h: the height of the light guide

In the Borexino case the radius of the light guide's opening is 15.5 cm and the radius of the photo cathode of the Thorn EMI 9351 photomultiplier is 9.5 cm. The distance of the photo cathode to the center of the Inner Vessel is 652 cm and the height of the light guide is 23 cm. This results in a geometric amplification factor f_G of 2.9.

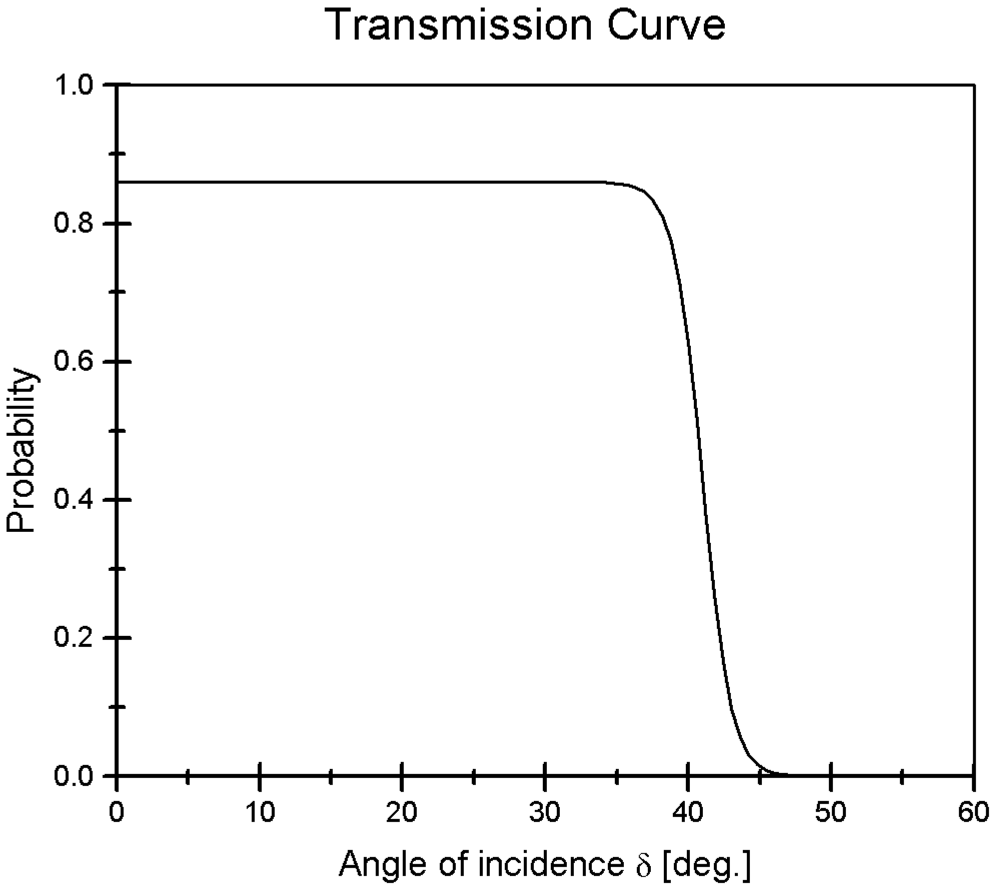

Figure 3.6: The calculated transmission curve (i.e. the collection efficiency for photons as a function of the angle of incidence) of the string cone designed for Borexino. The critical angle of acceptance is at $\approx 44^o$. The data points have been obtained in a Monte-Carlo calculation. The reflectivity R (for vertical direction of incidence) was a free parameter in the calculation. For $R = 0.86$ the data points coincide with the experimental value of 0.88 for the overall photon collection efficiency.

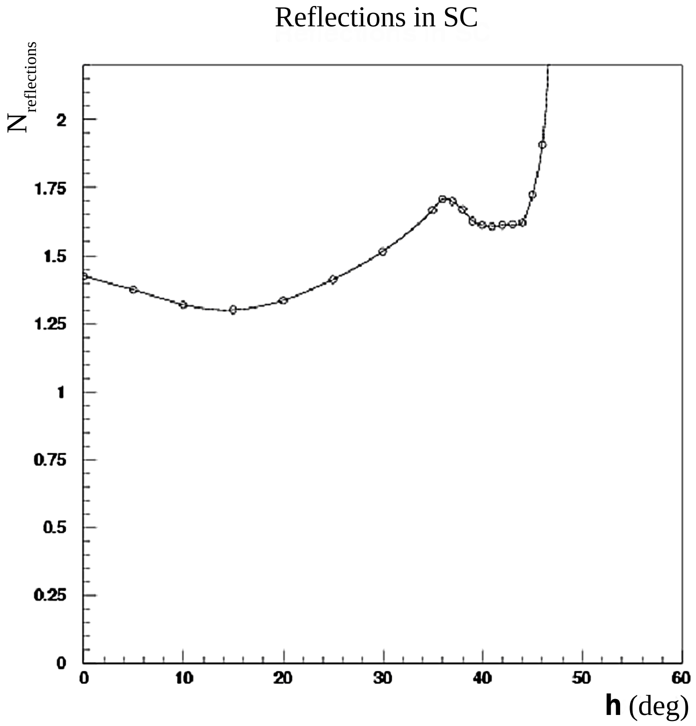

Figure 3.7: The calculated number of average reflections of a photon inside the Borexino light guide until it hits the photo cathode of the photomultiplier as a function of the angle of incidence. The ideal case of a two-dimensional cone with one reflection is only achieved within good approximation.

Borexino uses a total of 2214 photomultipliers, not counting the muon veto which is generally treated as a separate detector. Of these 2214 photomultipliers only 1870 have been equipped with light guides. The remaining 154 photomultipliers are used without light guides to improve the separation efficiency between point like events in the scintillator region (like a real neutrino event would be) and events that arise from a high energy cosmic muon crossing the buffer region of the detector. In the latter case, muons produce Čerenkov light and also scintillation light along their track [ALI 02]. Scintillation is strongly suppressed in the buffer region by the added quencher DMP (see Chapter 2), yet not completely. Note here that events in which the muon actually enters the scintillator vessel are not as dangerous as background, as their visible energy deposit is far above the energy range interesting for solar ^{7}Be neutrino detection. Experience with the CTF has shown that these muons crossing the buffer region can give rise to a non-negligible background [ALI 98-2].

Of the photons created by muons crossing the buffer region, a large part will not be observed by the photomultipliers with light guides, as their angle of incidence δ is greater than the light guide's maximum angle of acceptance. The photomultipliers without light guides however can detect these photons. Consequently the ratio between the number of photoelectrons seen by the photomultipliers without light guides and the number seen by the ones with light guides will be significantly higher for a muon that crosses the buffer region than for a point like event in the scintillator. The ratio between photomultipliers with and without light guides has been optimized with Monte Carlo calculations to maximize the separation power yet not lose too much ligh yield.

In total the effective geometrical coverage of the Borexino detector is 29.2 %, which is ≈ 2.5 times the value that would have been reached without using light guides.

3.2.2 The CTF Light Guides

The shape of the light guides for the CTF was calculated with the same method as for Borexino. Yet, due to the different geometry of the detector the CTF light guides (see Figure 3.3 on Page 29) are considerably bigger than their Borexino counterparts. The radius of their front opening is 25.3 cm and their length is 57 cm. In the CTF, the distance between the center of the scintillator vessel and the photomultiplier cathode is 3.3 m. The photomultipliers used are the same as in Borexino. Applying this to formula 3.2 results in a geometric amplification factor of $f_G \approx 10$ for a CTF photomultiplier.

Although the radius of the CTF scinitllator vessel is 1 m, for the calculation of the light guide's shape an effective radius of 1.2 m has been chosen. This increases their maximum angle of acceptance δ_{max} beyond the scintillator vessel and thus accommodates a possible misalignment of the light guides in the detector, like in Borexino.

The use of light guides in the CTF, which increased the geometrical coverage by a factor of ≈ 10, allowed to study the properties of the scintillator which will later be used in Borexino very sensitively. An energy threshold as low as 20 keV could be reached, using only 100 photomultipliers which are at 3.3 m distance for increased shielding from gamma ray background.

3.3 Construction and Reflectivity of the Light Guides

For the choice of material the light guides are made of, several aspects had to be considered: reflectivity, stability against degradation, mechanical feasibility, price and radioactive purity. Each of these points has posed difficulties and will be addressed separately in the following.

The light guide's reflectivity is crucial for their application in Borexino. The reflectivity, along with the shape of the light guide determine the collection efficiency for photons. The total gain in light yield is then the product of collection efficiency and geomtric amplification factor f_G.

The wavelength region of interest here is between about 370 nm and 450 nm. This is the wavelength range where the emission spectrum of the wavelength shifter PPO overlaps with a high collection efficiency of the photomultipliers. Of all possible materials suitable for the application, aluminum and silver have the highest reflectivity in this wavelength band. Their reflectivity at 400 nm is ≈ 90 % at vertical incidence.

In the CTF, the photomultipliers are immersed in ultra high purity deionized water. It has been found that deionized water corrodes aluminum very quickly, and even more so high purity aluminum (which was mandatory to use because of radioactive purity, see Chapter 3.4). Therefore silver was chosen as the reflective material for the CTF light guides. For Borexino however, the use of silver was not possible. The Borexino photomultipliers are immersed in Pseudocumene, which is not compatible with silver. Tests have shown that the surface of a silver layer turns purple after a short period of contact with Pseudocumene. Accordingly, the material of choice for the Borexino light guides had to be aluminum. A problem was that during the filling process of Borexino the light guides will be immersed in ultra pure deionized water for a period of time (possibly up to several months, see also Chapter 4.5.1), and also after the completion of the SSS installation the inside of Borexino was cleaned with ultra pure deionized water. Fortunately, a method was found to make the surface of the aluminum light guides resistant to deionized water for a period of time of up to 10 years, see text below.

3.3.1 Construction of the CTF Light Guides

The CTF light guides are made from acrylic which is UV transparent. The raw material came in plates with polished, very smooth surfaces. Both sides of the plates were covered with a protective plastic layer to keep the acrylic free from radioactive impurities (radon daughters) contained in dust (more on radioactive impurities in Chapter 3.4). The plates were cut to shape and then heated to remove water from the acrylic. In a thermal deep drawing process the plates were then formed to their shape as calculated with the string method described in Chapter 3.2. Only the inner protective plastic layer was removed for the deep drawing process. The light guides were then cut on both ends to their calculated length. Each light guide received four little acrylic holders on the rear side which serve as mounting points. For the ensuing transport the light guides were each packed in a clean plastic bag to ensure their cleanliness. Then the reflective silver layer was evaporated on the *outside* of the light guides. The second protective plastic layer was removed just before this evaporation process. A thin protective copper layer was then evaporated onto the silver. In laboratory test it was found that the combination silver-copper has good adhesive properties on the acrylic surface and also is very resistant against corrosion in deionized water. A third, very thin acrylic layer sprayed onto the outside of the light guides serves as additional protection.

The total manufacturing cost of one CTF light guide was ≈ 230 €, which is a only small fraction of the price of a photomultiplier and the necessary electronics to operate it.

3.3.2 Long Term Stability of the CTF Light Guides

The long term stability of the light guides is an important issue as they cannot be very easily replaced. Any work on the inside of the detector implies complete draining of the scintillator and the surrounding shielding liquid, which is a difficult process that can take months. This is not only the case in the CTF, but even more so in Borexino.

To estimate the amount of degradation of the light guides over time, laboratory tests were performed. For the CTF light guides, the material composition used was placed in deionized water at higher temperatures. This method, called accelerated aging test, relies on the general rule of thumb that the speed of a chemical reaction increase by a factor of ≈ 2 for a rise in temperature of 10 ^{o}C. This assumption has been tested and verified for the Borexino light guides, see Chapter 3.3.4 With a temperature of ≈ 40 ^{o}C above the ambient temperature of ≈ 15 ^{o}C in the Gran Sasso underground laboratory, it is possible to simulate the degradation by corrosion that would take place after several years within a few months. No visible deterioration of the light guides was found.

The light guides for the CTF were installed in the summer of 1994. During the first operational period of the detector from December 1994 to March 1997, the light yield per photomultiplier remained unchanged. This allows the conclusion that no significant degradation of the reflective surface of the light guides took place during this period of time of almost 2 1/2 years. Some of the light guides though showed degradation on their *outside*, and although this did not have an effect on their light collection capabilities, were replaced with newly manufactured spares. These new light guides have an additional silver layer on top of the copper protective layer instead of the acrylic spray.

In the next CTF measurement campaign between 1999 and 2001, the light guides were immersed in deionized water again. There was no loss in light yield per photomultiplier observed. The total light yield did decrease however due to the malfunctioning of several photomultipliers. During this period a different scintillator (PXE, Phenyl-o-xylylethan) was tested. Unfortunately, the nylon vessel which contained the scintillator was damaged and a small amount of the scintillator (several liters) leaked into the water buffer and thus came in contact with the light guides. As this incident occured during the draining of the water buffer, only the light guides on the lower hemisphere of the detector were affected. Almost all of them developed cracks which typically extended over the whole length of the light guide. This damage happened over the course of only a few days. After the complete draining of the detector, the light guides were removed and repaired. A large fraction of them could be glued back together, the rest were replaced by spares.

The most recent measurement campaign of the CTF is ongoing since fall 2001, and during these three years again the light yield per photomultiplier was observed to be stable. In conclusion, the stability against long term degradation of the CTF light guides was achieved as planned.

3.3.3 Construction of the Borexino Light Guides

As mentioned before, the Borexino light guides will be immersed in an organic solvent, Pseudocumene, during the operational phase of the detector. Acrylic could therefore not be used, and the material chosen for the Borexino light guides was aluminum because of it's high reflectivity (see the introduction in 3.3).

The choice of the bulk aluminum was very difficult. It had to be very pure in terms of radioactivity, especially thorium, see Chapter 3.4, yet the very pure aluminum which is unalloyed is extremely soft and therefore not usable in normal machining processes. In addition, high purity aluminum is very expensive and can cost up to several thousand €/Kg compared to approximately 5 €/Kg for standard grade aluminum.

After the bulk material had been chosen, plates of 3 mm thickness were produced. Then, from these plates round discs were cut. The discs were needed for the ensuing spinning process. In the spinning, the disc is mounted on top of a negative form of the light guide (a cone-shaped steel high precision steel form). Then the form together with the aluminum disc on top are spun around the axis of symmetry. A movable arm with a small wheel at the end (to reduce friction) presses the aluminum disk slowly against the form. This is done in several steps to avoid ripping the aluminum by forming it too fast. The thickness of the aluminum is reduced from 3 mm to $\approx$ 1 mm during this process. This was intended to make the light guides as light as possible, i.e. keep the total mass of aluminum and consequently radioactive isotopes introduced in the detector as low as possible, see Chapter 3.4. As mentioned earlier, it was necessary to deviate a little bit from the ideal shape calculated by the string method (Chapter 3.2). The form which was used in the spinning process has to be taken out by the front opening of the light guide, which means that the light guide cannot get smaller toward that opening. It was only a minor change which reduced the length of the light guides by about 1.5 cm and had a very small impact on the light yield (a reduction of 2.25%, see Chapter 3.2). Sticking to the ideal form would have doubled the cost of the spinning process.

After the spinning process, the light guides were cut to the right length, and holes for mounting them on the photomultipliers were drilled. They were then mechanically ground and polished on their inside to improve the smoothness of the surface. A final anodization of the surface in several steps to a depth of $\approx 7\ \mu$m makes the aluminum extremely inert and therefore resistant to degradation in deionized water during the initial filling procedure (see also Chapter 4.5.1 for the initial filling).

The shape of some of the manufactured cones has been measured to verify the agreement between their shape and the ideal (calculated) shape. It was found that the diameter of the light guides as a funtion of the height agrees to within $\approx$ 1 mm with the theoretical curve. It is only a minor deviation which is within the specifications of production accuracy and introduces only a very small loss in light collection efficiency. Due to the anodization process the Borexino light guides have a less smooth inner surface then the CTF ones. This was investigated by measuring the broadening of a parallel lase beam hitting the surface at an angle of 45^o. After one reflection, the laser beam showed a broadening of $\approx 3^o$. Calculations have shown that the impact of this on the photon collection efficiency is negligible. This is also in agreement with the measurement performed to determine the photon collection efficiency, see

Chapter 3.3.5.

The total manufacturing cost of one Borexino light guide was ≈ 100€. This is very cheap considering the fact that the increase in light yield per channel is ≈ 2.5 and one photomultiplier channel including the readout electronics costs about 2000 €. Achieving the same light yield for Borexino without using light guides would have meant an additional investment of ≈ 10 M€ in photomultipliers and electronics.

3.3.4 Long Term Stability of the Borexino Light Guides

As mentioned in Chapter 3.3.3, the surface of the Borexino light guides has been anodized to protect them from corrosion in water. Similar to the CTF light guides (in Chapter 3.3.2), an accelerated aging test has been performed to test the long term degradation of the surface. One light guide was immersed in hot deionized water for several months, which corresponded to more than 10 years at 15 ^{o}C, the ambient temperature in the Gran Sasso underground laboratory. The tested light guide showed no visible degradation or the reflective surface afterwards. Only very small corrosion spots could be seen at the mounting points where the anodization layer had been damaged. The reflectivity of this light guide was measured and was compatible with the value of a new light guide within the uncertainty of the measurement (Chapter 3.3.5).

The rate of corrosion of the aluminum light guides was measured in a laboratory experiment [GRI 00]. An aluminum sample cut from a light guide was used as an electrode in deionized water and Pseudocumene against a steel electrode, see Figure 3.8 on Page 42. The electrical current between the two electrodes gives information about the speed of the corrosion process. The loss of aluminum form the surface due to corrosion can be calculated from the measured corrosion current:

$$\dot{d} = \frac{I \cdot M_A}{n \cdot e \cdot \rho \cdot A} \tag{3.3}$$

I: the measured corrosion current
$\dot{d}$: material loss in nm/year
M_A: Atomic mass of aluminum
n: charge multiplicity of the aluminum ion
e: elementary charge
A: the total surface area of the aluminum electrode which is covered by the deionized water

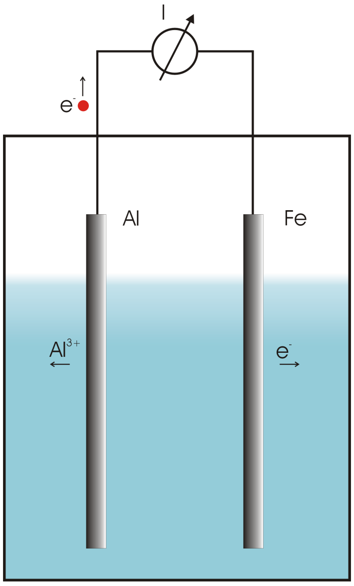

Figure 3.8: Experimental setup to measure the rate of corrosion of the aluminum used for the light guides. An aluminum electrode and a steel electrode are immersed in either deionized water or Pseudocumene. The speed of the oxidization can be quantified by measuring the electric current between the two electrodes.

This experiment yielded a corrosion current I of 11.5 nA, or using equation 3.3 and taking into account the uncertainties, a material loss through corrosion of 3.0 ± 0.5 nm/year. Considering the thickness of the protective anodization layer of ≈ 7 μm, one can conclude that the degradation of the surface of the light guides, by corrosion while being immersed in deionized water for several months, is negligible. For corrosion while being immersed in Pseudocumene, only an upper limit could be experimentally determined. The loss of aluminum from the surface is less than 0.3 nm/year in this case.

3.3.5 Photon Collection Efficiency of the CTF and Borexino Light Guides

The photon collection efficiency of the CTF and Borexino light guides were measured in a laboratory experiment, Figure 3.9 on Page 44. The measurement was done with scintillation photons. This has the advantage that the light has the same wavelength as it will have in the real use of the light guides. The experiment consisted of a spherical glass container with a diameter of 5 cm for the scintillator. A mixture of Pseudocumene with 1.5 g/l PPO as wavelength shifter was used, the same scintillator as in Borexino. Attached to the scintillator sphere was a ^{137}Cs source, an emitter of 660 keV gamma rays. These gamma rays can enter the scintillator sphere and undergo Compton scattering. The recoil electrons then create scintillation light. If a gamma ray gets Compton scattered at the maximum scattering angle of 180 degrees (back scattering), it can be detected by a NaI detector which is placed behind the ^{137}Cs source. There is a photomultiplier close the scintillator sphere (will be called "near PM") to detect the scintillation light and one photomultiplier of the Borexino/CTF type placed at variable distances between 29 cm and 98 cm from the scintillator sphere (will be called "far PM"). By operating the NaI detector in coincidence one can achieve a mono-energetic recoil signal. The energy of the recoil electron after Compton scattering is:

$$E_e = E_\gamma - \frac{E_\gamma m_0 c^2}{E_\gamma \left(1 - \cos\Theta\right) + m_0 c^2} \tag{3.4}$$

E_e: energy of the recoil electron
E_γ: energy of the incident gamma ray
Θ: scattering angle of the gamma ray
m_0: electron rest mass

The NaI detector selects those events where $\Theta = 180$ degrees, which results in a recoil energy of ≈ 476 keV for the electron.

In the experiment, the ratio of triple coincidences n_3 between all three detectors and double coincidences n_2 between NaI and near PM was measured. The overall photon collection efficiency of the light guide can then be determined by comparing the data taken with and without light guide on

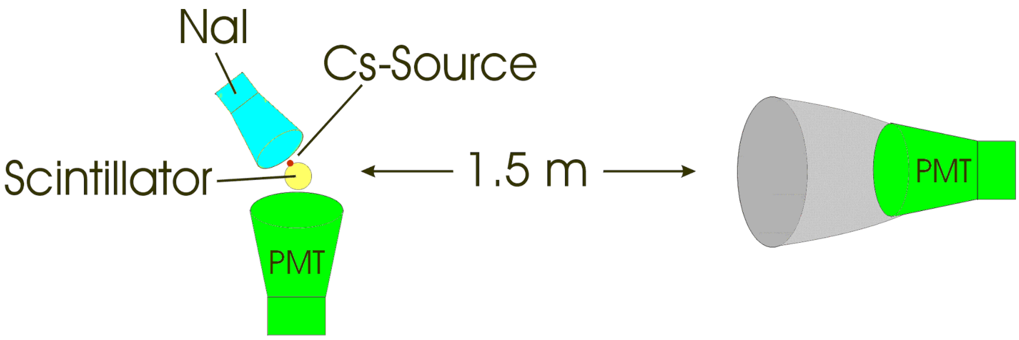

Figure 3.9: Experimental setup to measure the photon collection efficiency of the light guides. A glass sphere of 5 cm diameter holds the Borexino type scintillator. Attached to it is a ^{137}Cs source. A NaI detector behind the source measures backscattered gamma rays in coincidence with a near photomultiplier. The far photomultiplier can be placed at various distances to the scintillator and can be equipped with a light guide.

the far PM and at different distances between scintillator and far PM. The average number of photo electrons μ_0 measured in the far PM without light guide is proportional to the solid angle coverage:

$$\mu_0 = C\frac{\pi r^2}{4\pi d^2} \tag{3.5}$$

r: the radius of the far PM's entrance window (9.5 cm)
d: distance between the scintillator sphere and the far PM (29 cm - 98 cm)
C: a constant factor

The constant C depends on the light yield of the scintillator in the energy window that is selected by the double coincidence between the near PM and the NaI and on the efficiency of the far PM.

If there is a light guide mounted onto the far PM, the average number of photo electrons measured changes to:

$$\mu_+ = C\frac{\varepsilon\pi R^2}{4\pi\left(d-l\right)^2} \tag{3.6}$$

R: the radius of the light guide's entrance opening
d: distance between the scintillator sphere and the far PM (29 cm - 98 cm)
l: the length of the light guide
ε: the light guide's photon collection efficiency
C: a constant factor

The average number of photo electrons measured according to Poisson statistics is:

$$\mu = -\ln\left(1 - \frac{n_3}{n_2}\right) \tag{3.7}$$

With n_3/n_2 being the ratio between the number of triple coincidences and double coincidences.

The photomultiplier's threshold was adjusted to be fully sensitive to single photon pulses. The distance d between the scintillator sphere and the far PM was chosen so that the values of n_3/n_2 vary between 0.3 and 0.6 in order to avoid large uncertainties. By comparing the measured values of μ_0 and μ_+ one can determine the quantities C and $C \cdot \varepsilon$. Under the assumption that the value of C is the same in both cases (with and without light guide) the photon collection efficiency ε can be calculated.

The photon collection efficiency for the Borexino light guides is $\varepsilon = 0.88 \pm 0.04$. The measurement for the CTF light guides coincidentally produced the same result.

A Monte Carlo Calculation for the photon collection efficiency of the Borexino light guides was done in which the reflectivity $R$of the aluminum surface was kept as a free parameter. If the reflectivity R is set to 86%, the Monte Carlo calculation produced the experimental value of 0.88 for the photon collection efficiency of the Borexino light guide, see Figure 3.6 on Page 33. A direct measurement of the reflectivity of the anodized aluminum as used for the Borexino light guides yielded a value of $\approx$ 80%. This is less than the theoretical maximum value of 91% for aluminum at 400 nm. The loss in reflectivity can be attributed to the anodization of the surface though. The difference between the measured value of $\approx$ 80% and the value that was determined in the Monte Carlo is due to the different angles of incidence. The average angle of incidence in the photon collection measurement is significantly lower that 90 degrees, at which the reflectivity measurement was performed. A higher value for the reflectivity is therefore expected and the experimental result is very plausible.

All the laboratory measurements were done in air. In the real application though, the light guides are immersed in Pseudocumene (in Borexino) and in water (in the CTF). This might lead to slightly higher values of the photon collection efficiency ε in the real application than in the laboratory measurments. As the light guide increases the average angle of incidence on the glass of the photomultiplier compared to the case without using a light guide, the efficiency of the photomultiplier decreases. A higher angle of incidence of the photon means a higher reflectivity on the glass surface, thus a smaller chance of detection. This effect will be smaller though when the photomultiplier is under water or Pseudocumene as the indeces of refraction between the surrounding medium and the glass will match better then as it is the case in air.

The overall amplification factor f_t for a light guide is the product of the geometric amplification factor f_G (see equation 3.2) and the photon collection efficiency ε:

$$f_t = f_G \cdot \varepsilon \tag{3.8}$$

Neglecting the possible enhancement mentioned above, with the values measured in the laboratory experiment, the overall amplification factors f_t are 2.5 for the Borexino light guides and 8.8 for the CTF light guides.

All the Borexino light guides were installed by 2001. In a first test measurement with a small scintillator vessel doped with ^{222}Rn the light yield was as expected. In the CTF, the use of the light guides leads to a photo electron yield of $\approx$ 300 pe/MeV [ALI 98-1]. The trigger condition is a coincidence of at least 6 photomultipliers, which is sufficiently high to reduce the accidental trigger events to less than 1 per day. This trigger threshold corresponds to $\approx$ 6 photo electrons, which means the energy threshold achieved in the CTF is $\approx$ 20 keV.

3.4 Radiopurity of the CTF and Borexino Light Guides

Borexino is an ultra-low background detector. It will observe approximately 36 neutrino events per day in ≈ 100 t of scintillator and a recoil energy window between 250 keV and 800 keV. This assumes the occurrence of neutrino oscillations with the current best fit parameters for the squared mass difference $\Delta m_{12}^2 = 8.2 \cdot 10^{-5} eV^2$ and the mixing angle $\tan^2 \Theta_{12} = 0.39$ [BAH 04]. Most of these events are due to the ^{7}Be-neutrino electron scattering. In order to distinguish this signal from radioactive background, all the detector components have been carefully selected to keep the radioactive contamination as low as possible.

3.4.1 Radiopurity requirements for the CTF and the Borexino Light Guides

3.4.1.1 CTF

The CTF light guides were produced from UV transparent acrylic plates. Measurements of these plates with low background gamma spectroscopy using Ge-detectors have been done to determine the contamination by radioactive isotopes. The measurements only yielded upper limits for the ^{238}U and ^{232}Th content of $\approx 10^{-9} \frac{g}{g}$. These measurements assume secular equilibrium in the decay chains, and the reported concentrations are equivalent values of ^{238}U and ^{232}Th, respectively. The most dangerous contributor to background here is ^{208}Tl which occurs in the lower part of the thorium chain. ^{208}Tl emits a highly penetrating 2.6 MeV gamma ray with a high branching ratio in it's decay. Lower energy gamma rays are shielded very efficiently by the water buffer in the CTF. The low concentrations of thorium present in the acrylic material though are not dangerous for the CTF experiment. For natural potassium though the measured concentration in the bulk acrylic is $\approx 10^{-7} \frac{g}{g}$. Natural potassium contains $\approx 0.012\%$ ^{40}K which emits a 1461 keV gamma ray. Yet, due to the lower energy compared to the 2.6 MeV gamma ray from the ^{208}Tl, the penetration power is much smaller. Therefore, this concentration of potassium was acceptable for the CTF.

3.4.1.2 Borexino

In Borexino the requirements were stricter than in the CTF, and also with aluminum as bulk material proved to be more difficult to fulfill. The shielding in Borexino is higher than in the CTF (≈ 2.4 meters passive buffer plus ≈ 1.2 meters active scintillator shielding, see Chapter 2), but also the background aimed for in Borexino is extremely low. The design goal for the light guides was to limit their contribution to the background events to a *negligible* level, i.e. well below 1 count/day in the the fiducial volume of 100 tons and the ^{7}Be energy window between 250 keV and 800 keV. It was found that aluminum typically contains ^{2}32Th and its daughter isotopes, yet is very pure concerning uranium (Chapter 3.4.2). For Borexino it was necessary to determine the background contribution of the light quantitatively which was done in Monte Carlo studies (Chapter 3.4.3). The Monte Carlo studies also went hand in hand with the material selection to determine which type of aluminum could be used. The selection of the bulk aluminum was very difficult. It is possible to buy purified aluminum, and one of the world's leading aluminum producers (VAW Aluminium AG) has a special branch for marketing ultra pure aluminum, but unfortunately the price scales exponentially to the purity. Another problem was that, as mentioned earlier, very pure unalloyed aluminum is extremely soft and cannot be machined in conventional ways.

3.4.2 Measurement of Radioactive Purity of the Bulk Aluminum for the Borexino Light Guides

The goal was to find the purest possible (concerning radioactive isotopes) aluminum for an affordable price. Field measurements of aluminum types of different quality and from different sources were done in order to find a suitable bulk material. The concentration of various radioactive isotopes was determined via gamma ray spectroscopy using a Ge-detector.

3.4.2.1 The Germanium Detector Setup

The Ge-detecotor used is of the "Ortec LOAX" type and employs a 115 cm^{3} Germanium crystal. It is located at the Underground laboratory at the Technische Universität München in Garching at a depth of ≈ 15 m.w.e.

Figure 3.10 on Page 49 shows the setup of the detector. The detector has a carbon entry window and is shielded by 20 cm of lead all around. The innermost 5 cm of the lead shielding are made of ultra pure lead with an activity of ^{210}Pb of less than 3 Bq/Kg. ^{210}Pb is instable with a half life of 22.26 years and emits a 46.5 keV gamma ray. The attenuation length of a 46.5 keV gamma ray in lead is ≈ 0.07 mm, therefore it is sufficient to only use the pure lead on the inside of the shielding. Gamma rays of this energy originating in the outer lead shield will not be able to penetrate into the detector.

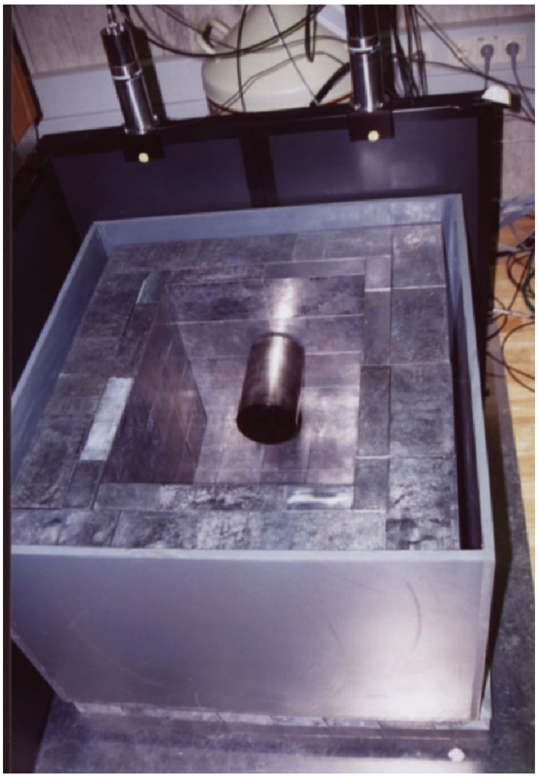

Figure 3.10: The setup of the Ge-detector in the underground laboratory in Garching. The detector is open, and the cup which holds the Ge crystal can be seen. Two layers of lead, standard on the outside and ultrapure with a ^{210}Pb activity of less than 3 Bq/Kg on the inside, shield the detector from ambient radioactivity. In the back there are two plastic scintillator panels which belong to the active muon veto. The other panels which completely encase the detector have been removed to take this picture.

The Ge crystal is placed inside an evacuated container to protect its surface, see Figure 3.11 on Page 50. This container has a very thin carbon window on one side which allows the gamma rays to enter. The sample to be measured is placed in front of this carbon window. Gamma rays which emerge from the sample can hit the Ge crystal and undergo compton scattering and photo absorption inside the Ge crystal. The detector measures the total energy transferred to electrons, which means that only if the gamma ray does not leave the Ge crystal again, its total energy is measured. Also, if the gamma ray is compton scattered either inside the sample itself or in the carbon window, it loses energy and will fall out of the peak in the spectrum which is used to determine the count rate. Figure 3.12 on Page 51 shows an exemplary spectrum.

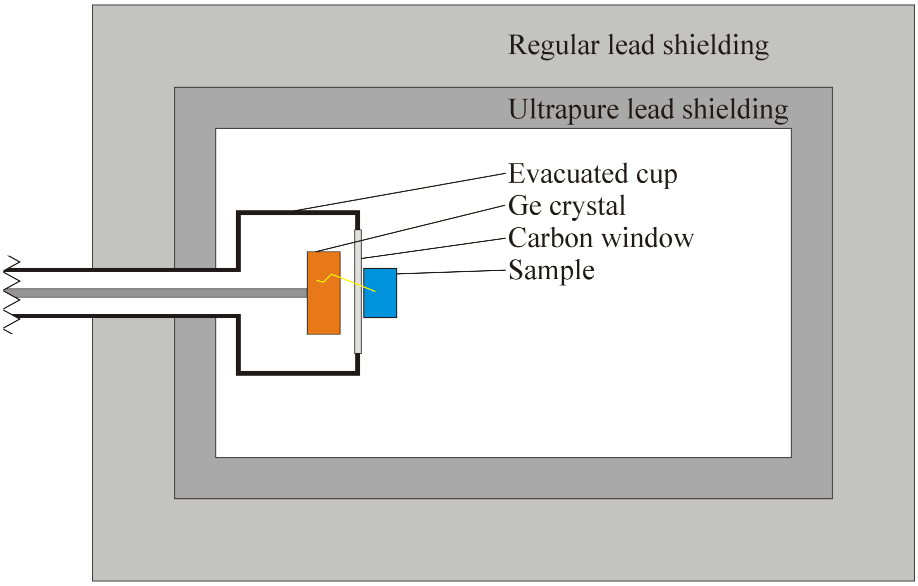

Figure 3.11: A schematic view of the Ge detector setup. The Ge crystal is placed inside an evacuated container. A very thin carbon window allows gamma rays to enter. The sample is placed as close as possible to the crystal for maximum solid angle coverage.

To determine the activity of a certain isotope in the sample, the measured spectrum has to be analyzed in order to find a peak with the energy of one of the characteristic gamma lines of the decay of this isotope. The number of events in this peak will be called N. It depends on the activity of the corresponding isotope, the time during which the measurement took place, the emission probability of the gamma ray and an efficiency factor ε:

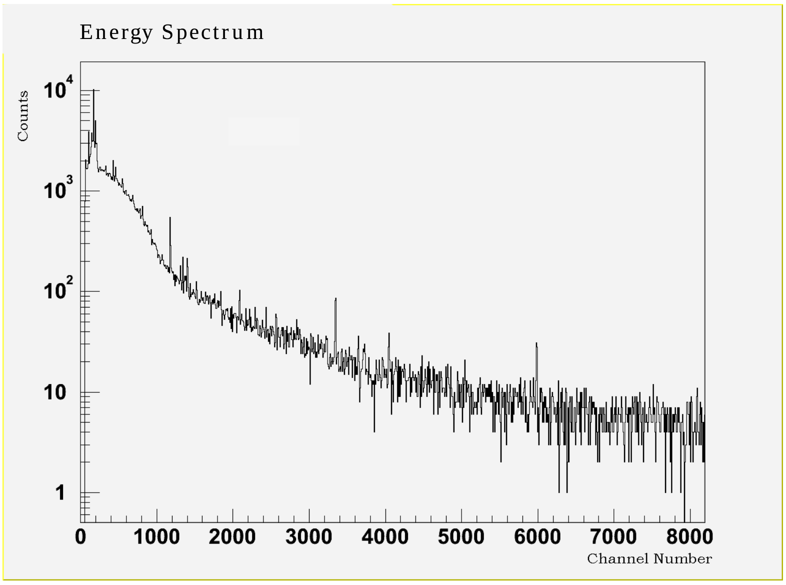

Figure 3.12: An energy spectrum taken with the “LOAX” Ge-detector. It is from an aluminum sample of the Borexino light guides and was taken during a period of time of 285 hours. Characteristic gamma lines can be seen emerging from the continuous compton background. See Figure 3.13 for an enlarged view.

$$N = A \cdot t \cdot \varepsilon \cdot p \tag{3.9}$$

N: Number of counts in the peak
A: Activity of the isotope
t: Time
ε: Efficiency factor
p: Emission probability of the gamma ray in this decay

The amount of radioactive contamination will always be quoted in mass concentrations of the isotope in units [g/g]. This allows the direct comparison between different materials. The mass concentration is calculated as follows:

$$c = \frac{A \cdot T_{1/2} \cdot m_A}{m_s \cdot \ln 2} \tag{3.10}$$

c: Mass concentration
A: Activity of the isotope, from equation 3.9
$T_{1/2}$: Halflife time of the isotope
m_A: Atomic mass of this isotope
m_s: Mass of the sample

The efficiency factor ε is the probability that a gamma ray emitted in the sample will deposit its total energy in the Ge crystal via compton scattering and photo effect. Accordingly, ε depends on the geometry of the setup, for example in terms of how large is the solid angle covered by the crystal or how far has the gamma ray to travel through the sample itself without losing energy. It also depends on the materials involved and the energy of the gamma ray as these determine the cross sections for compton scattering and photo effect. Obviously, it is not possible to calculate ε exactly, but it can be measured with reference samples of known activity. However, if this reference sample does not have the same geometric form and is not of the same material as the sample itself, the result will be inaccurate as effects like energy loss in the sample will be different. In order to get accurate results for the contaminations though it is mandatory to have an accurate value of

ε for the characteristic gamma lines used. This was achieved by a full Monte Carlo simulation of the detector setup.

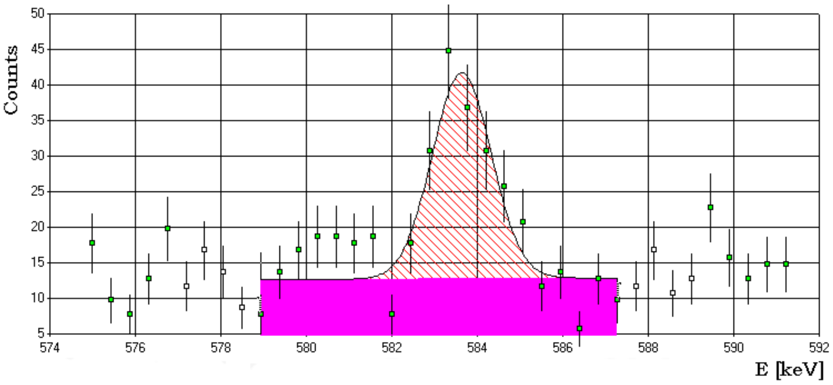

Figure 3.13: A small region of the spectrum shown in Figure 3.12 on Page 51. The x-axis is calibrated to show keV. The peak shown is the 583.2 keV line, which is emitted with a probability of 84.5% in the decay of ^{208}Tl. A Gaussian fit to the spectrum determines the number of counts in this peak above the continuous background.

3.4.2.2 Monte Carlo Simulation of the Germanium Detector with EGS

The probability ε that a gamma ray emitted in a sample deposits its total energy in the Ge crystal was calculated. This was done using the simulation toolkit "*EGS*", short for Electron Gamma Shower [KAW 03]. This toolkit is Fortran based and provides the capability to calculate the transport of electrons and photons with energies between a few keV and several hundred GeV through matter. The following physics processes are taken into account:

- Production of Bremsstrahlung
- Positron annihilation in flight and at rest
- Multiple scattering of charged particles by coulomb scattering
- Møller (e^-e^-) and Bhabha (e^+e^-) scattering
- Pair production

- Compton scattering
- Coherent (Rayleigh) scattering can be included optionally
- Photo effect
- Relaxation of excited atoms after vacancies are created (eg after photoelectric or Compton scattering events) to create fluorescent photons (K, L, M shells)

To use this toolkit the geometric setup and the materials need to be specified. Then, a single gamma ray can be created and its path through the detector along with the interactions that occur can be tracked. This needs to be done repeatedly with gamma rays starting in random places in the sample and going in random directions. The efficiency parameter ε and its uncertainty is then:

$$\varepsilon = \frac{N_{peak}}{N_{total}} \pm \frac{\sqrt{N_{peak}}}{N_{total}} \tag{3.11}$$

ε:	Efficiency parameter
N_{peak}:	Number of gamma rays which deposited their total energy in the Ge crystal
N_{total}:	Total number of gamma rays tracked

This simulation has been done for all the characteristic gamma lines which were seen in the spectra of the various aluminum samples and could be attributed to radioactive contaminations in the sample. Table 3.1 on Page 55 gives an overview over the isotopes found or investigated, their characteristic gamma lines, the emission probabilities p and the calculated efficiencies ε for each line. All the efficiencies have been calculated using using the same geometry: the aluminum sample is a solid block with the dimensions 60 mm by 60 mm by 31 mm and a mass of 301 grams. This block is placed in front of the carbon window at a distance of less than 1 mm, see Figure 3.11 on Page 50 for illustration. All the aluminum samples measured were cut into this shape to reduce the influence of systematic errors in the determination of the efficiencies (by avoiding to calculate different efficiencies for different shapes each time).

Energy	Isotope	Decay chain	Branching p	Efficiency ε
185.7 keV	^{235}U	^{235}U	57.2 %	$(3.81 \pm 0.04)\,\%$
186.1 keV	^{226}Ra	^{238}U	3.5 %	$(3.81 \pm 0.04)\,\%$
236.0 keV	^{227}Th	^{235}U	12.3 %	$(3.44 \pm 0.03)\,\%$
238.6 keV	^{212}Pb	^{232}Th	43.3 %	$(3.42 \pm 0.03)\,\%$
241.0 keV	^{224}Ra	^{232}Th	3.97 %	$(3.42 \pm 0.03)\,\%$
242.0 keV	^{214}Pb	^{238}U	7.5 %	$(3.40 \pm 0.03)\,\%$
277.4 keV	^{208}Tl	^{232}Th	6.3 %	$(3.09 \pm 0.03)\,\%$
295.2 keV	^{214}Pb	^{238}U	18.5 %	$(2.93 \pm 0.03)\,\%$
300.0 keV	^{227}Th	^{235}U	2.67 %	$(2.90 \pm 0.03)\,\%$
300.1 keV	^{212}Pb	^{232}Th	7.57 %	$(2.89 \pm 0.03)\,\%$
351.1 keV	^{211}Bi	^{235}U	12.9 %	$(2.58 \pm 0.03)\,\%$
351.9 keV	^{214}Pb	^{238}U	35.8 %	$(2.56 \pm 0.03)\,\%$
583.2 keV	^{208}Tl	^{232}Th	84.5 %	$(2.12 \pm 0.02)\,\%$
609.3 keV	^{214}Bi	^{238}U	44.8 %	$(1.75 \pm 0.02)\,\%$
661.7 keV	^{137}Cs	-	85.1 %	$(1.64 \pm 0.02)\,\%$
727.3 keV	^{212}Bi	^{232}Th	6.58 %	$(1.46 \pm 0.02)\,\%$
860.6 keV	^{208}Tl	^{232}Th	12.4 %	$(1.14 \pm 0.01)\,\%$
911.2 keV	^{228}Ac	^{232}Th	26.6 %	$(1.15 \pm 0.01)\,\%$
969.0 keV	^{228}Ac	^{232}Th	16.2 %	$(1.11 \pm 0.01)\,\%$
1120.3 keV	^{214}Bi	^{238}U	14.8 %	$(0.88 \pm 0.01)\,\%$
1460.8 keV	^{40}K	-	16.7 %	$(0.81 \pm 0.01)\,\%$
1764.5 keV	^{214}Bi	^{238}U	15.4 %	$(0.65 \pm 0.01)\,\%$
1808.6 keV	^{26}Al	-	99.7 %	$(0.61 \pm 0.01)\,\%$
2614.5 keV	^{208}Tl	^{232}Th	99.16 %	$(0.44 \pm 0.01)\,\%$

Table 3.1: The various radioactive isotopes which were either found in aluminum samples for the Borexino light guides or whose presence was investigated. The table shows the energies and the emission probability p of the most prominent characteristic gamma lines emitted in the decay. The efficiency ε is the probability that gamma ray of this energy emitted inside the aluminum sample deposits its total energy in the Ge crystal. It is also shown to which decay chain each isotope belongs, if applicable.

The accuracy of the Monte Carlo simulation was tested by comparison with efficiency measurements using radioactive samples with known activity. A first measurement using a very small (point-like) multi-isotope source containing ^{137}Cs, ^{109}Cd and ^{60}Co yielded very good results. The source was placed at different spots inside the detector to also test the dependence on the geometry. Then the peak count rate for each isotope was measured and using equation 3.9 the efficiency ε can be calculated. On the other hand, for each measurement the efficiency was also determined by using the Monte Carlo simulation. Tables 3.2 through 3.6 on Pages 56 through 57 show the comparison between measured efficiencies and the ones determined by simulation for the different experimental setups. It can be seen that the values agree within the quoted uncertainties. This can also be seen in Figures 3.14 and 3.15.

Energy	Isotope	Efficiency $\varepsilon_{measured}$	Efficiency $\varepsilon_{simulation}$
88.0 keV	^{109}Cd	$(4.05 \pm 0.08)\,\%$	$(4.10 \pm 0.08)\,\%$
661.7 keV	^{137}Cs	$(0.56 \pm 0.01)\,\%$	$(0.55 \pm 0.01)\,\%$
1173.2 keV	^{60}Co	$(0.375 \pm 0.008)\,\%$	$(0.369 \pm 0.007)\,\%$
1332.5 keV	^{60}Co	$(0.334 \pm 0.007)\,\%$	$(0.336 \pm 0.007)\,\%$

Table 3.2: Comparison between measured and simulated efficiencies ε for different gamma lines. The reference sample with known activity was very small, practically point-like. It was placed in front of the Ge-detector at a distance of 48 mm to the carbon window.

Energy	Isotope	Efficiency $\varepsilon_{measured}$	Efficiency $\varepsilon_{simulation}$
88.0 keV	^{109}Cd	$(2.93 \pm 0.06)\,\%$	$(2.86 \pm 0.06)\,\%$
661.7 keV	^{137}Cs	$(0.404 \pm 0.008)\,\%$	$(0.412 \pm 0.008)\,\%$
1173.2 keV	^{60}Co	$(0.273 \pm 0.005)\,\%$	$(0.279 \pm 0.006)\,\%$
1332.5 keV	^{60}Co	$(0.243 \pm 0.005)\,\%$	$(0.245 \pm 0.005)\,\%$

Table 3.3: Comparison between measured and simulated efficiencies ε for different gamma lines. The reference sample with known activity was very small, practically point-like. It was placed in front of the Ge-detector at a distance of 60 mm to the carbon window.

In a further test of the Monte Carlo simulation a sample of extended size was used. As mentioned above, the interaction of the gamma rays with the

Energy	Isotope	Efficiency $\varepsilon_{measured}$	Efficiency $\varepsilon_{simulation}$
88.0 keV	^{109}Cd	$(1.80 \pm 0.04)\,\%$	$(1.76 \pm 0.04)\,\%$
661.7 keV	^{137}Cs	$(0.257 \pm 0.005)\,\%$	$(0.261 \pm 0.005)\,\%$
1173.2 keV	^{60}Co	$(0.175 \pm 0.004)\,\%$	$(0.179 \pm 0.004)\,\%$
1332.5 keV	^{60}Co	$(0.156 \pm 0.003)\,\%$	$(0.156 \pm 0.003)\,\%$

Table 3.4: Comparison between measured and simulated efficiencies ε for different gamma lines. The reference sample with known activity was very small, practically point-like. It was placed in front of the Ge-detector at a distance of 80 mm to the carbon window.

Energy	Isotope	Efficiency $\varepsilon_{measured}$	Efficiency $\varepsilon_{simulation}$
88.0 keV	^{109}Cd	$(2.73 \pm 0.06)\,\%$	$(2.86 \pm 0.06)\,\%$
661.7 keV	^{137}Cs	$(0.407 \pm 0.008)\,\%$	$(0.408 \pm 0.008)\,\%$
1173.2 keV	^{60}Co	$(0.286 \pm 0.006)\,\%$	$(0.279 \pm 0.006)\,\%$
1332.5 keV	^{60}Co	$(0.242 \pm 0.005)\,\%$	$(0.235 \pm 0.005)\,\%$

Table 3.5: Comparison between measured and simulated efficiencies ε for different gamma lines. The reference sample with known activity was very small, practically point-like. It was placed in front of the Ge-detector at a distance of 60 mm to the carbon window, and shifted by 6 mm to the side in order to create a non-symmetrical setup.

Energy	Isotope	Efficiency $\varepsilon_{measured}$	Efficiency $\varepsilon_{simulation}$
88.0 keV	^{109}Cd	$(1.77 \pm 0.04)\,\%$	$(1.77 \pm 0.04)\,\%$
661.7 keV	^{137}Cs	$(0.262 \pm 0.005)\,\%$	$(0.261 \pm 0.005)\,\%$
1173.2 keV	^{60}Co	$(0.177 \pm 0.004)\,\%$	$(0.177 \pm 0.004)\,\%$
1332.5 keV	^{60}Co	$(0.159 \pm 0.003)\,\%$	$(0.163 \pm 0.003)\,\%$

Table 3.6: Comparison between measured and simulated efficiencies ε for different gamma lines. The reference sample with known activity was very small, practically point-like. It was placed in front of the Ge-detector at a distance of 80 mm to the carbon window, and shifted by 6 mm to the side in order to create a non-symmetrical setup.

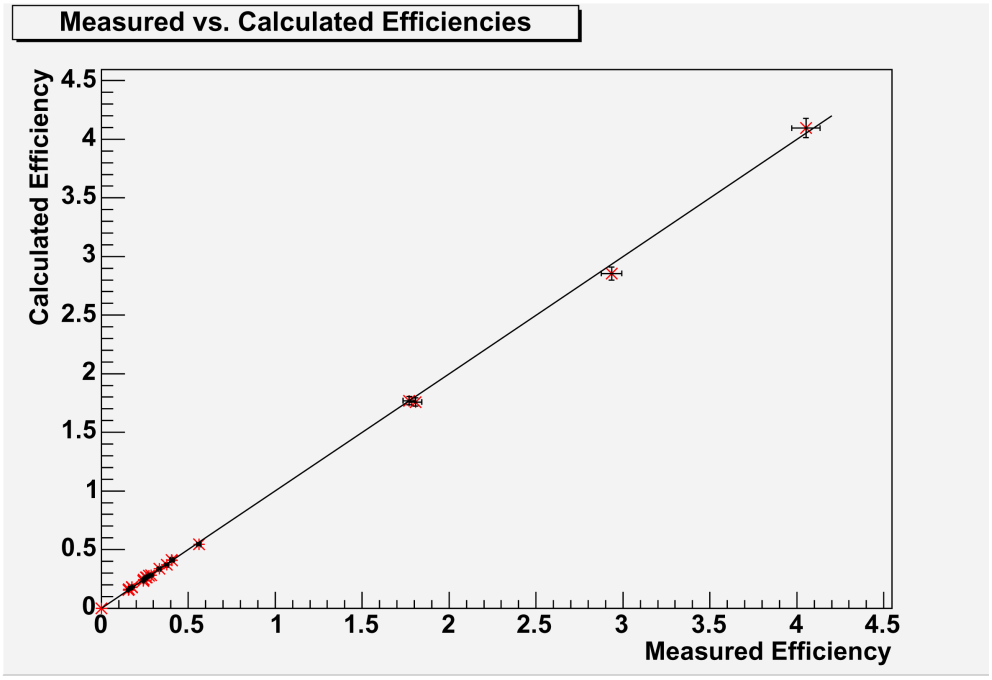

Figure 3.14: Comparison between measured detector efficiencies and ones calculated by Monte Carlo simulation. A multi-isotope reference source of known activity was placed at different locations inside the detector to measure different efficiencies. The simulated effiencies agree very well with the measured values.

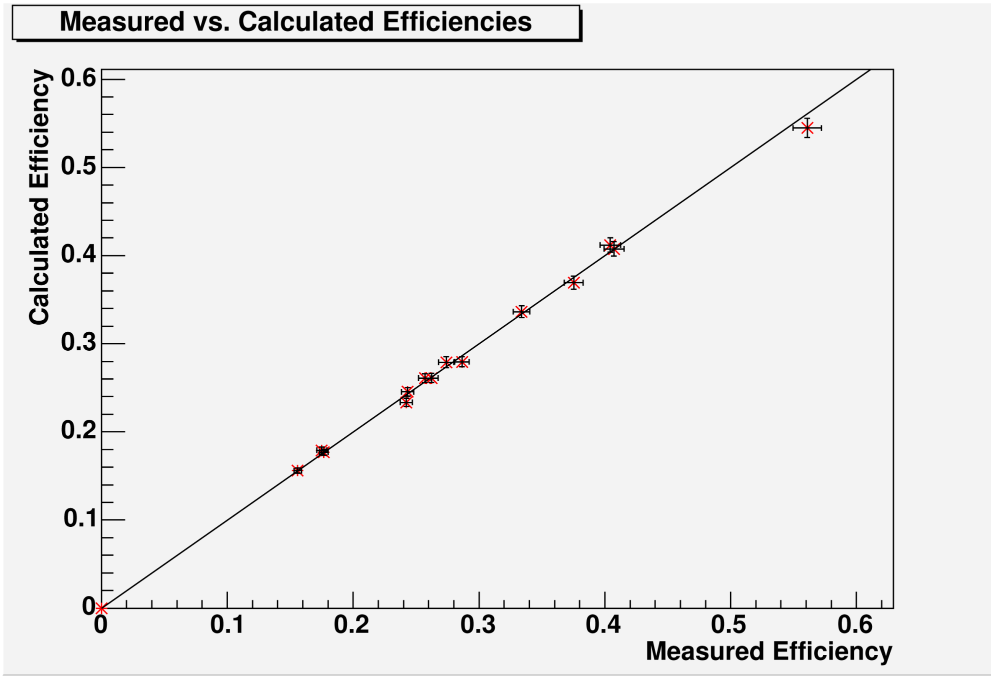

Figure 3.15: A zoomed in view of Figure 3.14 on Page 58. The efficiencies obtained by Monte Carlo simulation agree with the measured values within the uncertainties.

sample itself is not negligible. Any scattering in the sample leads to energy loss and thus reduces the detector efficiency. The measurement was with $\approx$ 59 g of a solution of ^{232}Th in sulfuric acid with an activity of 1045.0 Bq. The solution was held in a round plastic container with a diameter of 50 mm and a thickness of 30 mm. This container was placed directly in front of the carbon window of the Ge-detector. Table 3.7 on Page 61 shows the results of the efficiency measurement compared with the simulated efficiencies. Also in this case the simulation was able to reproduce the measured values within the quoted uncertainties, see Figure 3.16 on Page 60.

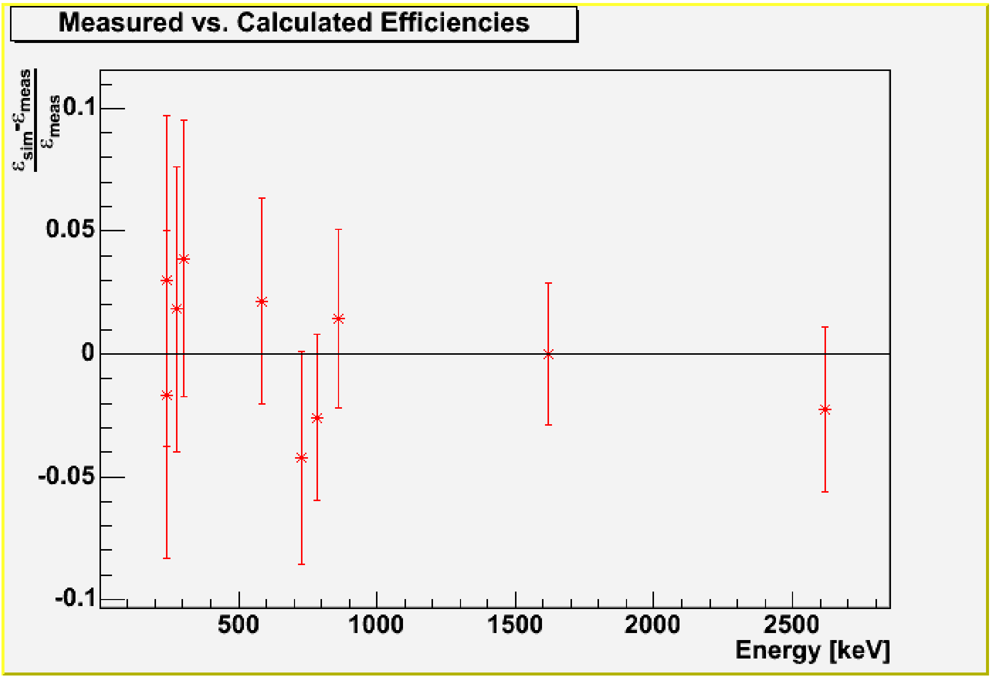

Figure 3.16: Comparison between simulated and measured detector efficiencies for a ^{232}Th-solution. Plotted on the x-axis is the energy of the respective gamma line, on the y-axis the deviation of the simulated efficiency ε_sim from the mesaured efficiency ε_meas, calculated as $\frac{\varepsilon_{sim}-\varepsilon_{meas}}{\varepsilon_{meas}}$. It can be seen that the efficiencies obtained by Monte Carlo simulation agree with the measured values within the quoted uncertainties.

In conclusion, the Monte Carlo simulation of the detector efficiencies ε produces reliable results with an accuracy of better than 2%. The efficiency ε can be measured, yet its value depends on the sample material and geometry, therefore it would be necessary to have a reference sample with known radioactive contents of the same shape and material as the sample to be analyzed in order to measure the correct value of ε. As this is not available in most cases, the Monte Carlo simulation is mandatory for measuring radioactive contaminations with the Ge-detector.

Energy	Isotope	Efficiency $\varepsilon_{measured}$	Efficiency $\varepsilon_{simulation}$
238.6 keV	^{212}Pb	$(5.38 \pm 0.11)\,\%$	$(5.54 \pm 0.11)\,\%$
241.0 keV	^{224}Ra	$(5.41 \pm 0.11)\,\%$	$(5.32 \pm 0.11)\,\%$
277.4 keV	^{208}Tl	$(3.84 \pm 0.08)\,\%$	$(3.91 \pm 0.08)\,\%$
300.1 keV	^{212}Pb	$(3.61 \pm 0.07)\,\%$	$(3.75 \pm 0.08)\,\%$
583.2 keV	^{208}Tl	$(1.85 \pm 0.04)\,\%$	$(1.89 \pm 0.04)\,\%$
727.3 keV	^{212}Bi	$(1.67 \pm 0.04)\,\%$	$(1.60 \pm 0.04)\,\%$
785.4 keV	^{212}Bi	$(1.55 \pm 0.03)\,\%$	$(1.51 \pm 0.03)\,\%$
860.6 keV	^{208}Tl	$(1.37 \pm 0.03)\,\%$	$(1.39 \pm 0.03)\,\%$
1620.5 keV	^{212}Bi	$(0.96 \pm 0.03)\,\%$	$(0.96 \pm 0.02)\,\%$
2614.5 keV	^{208}Tl	$(0.44 \pm 0.02)\,\%$	$(0.43 \pm 0.01)\,\%$

Table 3.7: Comparison between measured and simulated efficiencies ε for different gamma lines of a ^{232}Th solution. The values for ε calculated in the Monte Carlo simulation are in agreement with the measured values.

3.4.2.3 Results

Unfortunately, the Borexino light guides had to be produced from two different types of aluminum. Type 1 is the purest aluminum found during the field measurements. It was produced in the 1970's and had been kept on stock in one of the companies we were in contact with. We purchased the complete batch of about 400 Kg which was just enough to produce $\approx$ 350 light guides (of 1840 total). Type 2 aluminum is standard pure (99.8%) aluminum which was used to produce the rest of the light guides. A third kind, here called Type 3 was investigated but not used for practical reasons. It was highly purified aluminum marketed as “Kryal 5N5” with a purity of 99.9995 %. Its radioactive contamination was in between the Types 1 and 2, but it was enormously expensive and also very difficult to machine, as it is unalloyed and therefore extremely soft.

In the gamma spectroscopy measurements it was found that the equilibrium in the ^{232}Th as well as the ^{238}U decay chain is broken, which probably happened during the production process. Most important for the light guides is the content of ^{208}Tl from the thorium chain, as it emits a 2615 keV gamma ray with a high branching ratio (99%) in its decay (see Table 3.1 on Page 55). Due to the high energy this gamma ray can penetrate the shielding in Borexino, more quantitative information about this is given later on in Chapter 3.4.3.

All mass concentrations and activities quoted here are so called equivalent values, that means the concentration or activity of the decay chain's mother isotope under the assumption the decay chain is in equilibrium. Table 3.8 on Page 63 gives a summary of the results. The mass concentration thorium was 7 ng/g ($\triangleq$ 28 μBq/g) in the Type 1 aluminum. Type 2 aluminum was considerably higher at 220 ng/g ($\triangleq$ 890 μBq/g) for thorium. Type 3 showed $\approx$ 30 ng/g ($\triangleq$ 120 μBq/g). Both Type 1 and Type 2 aluminum was used to manufacture the light guides, and the mass weighted average thorium concentration is 180 ng/g ($\triangleq$ 730 μBq/g).

In all three types of aluminum, only an upper limit on the concentration of uranium daughter isotopes below ^{226}Ra could be found. It was less than 1 ng/g ($\triangleq$ 12 μBq/g). The concentration of uranium and its daughters above the ^{226}Ra was $\approx$ 100 ng/g ($\triangleq$ 1.2 mBq/g) in all three types of aluminum. This result shows clearly how the equilibrium in the decay chain is broken and that the isotopes below ^{226}Ra are depleted. Fortunately the prominent gamma lines of higher energy occur in the lower part of the decay chain, so that the higher concentrations of isotopes above ^{226}Ra will not create measurable external background in Borexino.

For the isotopes of the ^{235}U chain also only an upper limit on the concentration could be measured. It is $<$ 2 ng/g ($\triangleq$ 130 μBq/g).

Another isotope which is potentially dangerous for Borexino is ^{40}K. In its decay a gamma ray of 1461 keV can be emitted (Table 3.1 on Page 55). Only an upper limit on the concentration of K could be measured for all three types of aluminum. It is $<$ 10 μg/g for natural Potassium K_{nat} which is equivalent to $<$ 300 μBq/g (with 0.0117 % ^{40}K in K_{nat}). Although this would be a considerable activity, the background contribution expected is negligible due to the lower energy of the gamma ray compared to the 2.6 MeV line from

^{208}Tl. This has also been investigated in Monte Carlo calculations and will be quantified in Chapter 3.4.3.

In principle, ^{26}Al, which is produced in reactions of cosmic rays in the atmosphere, could create background in Borexino as it emits a 1809 keV gamma ray. However, only an upper limit of $< 4 \cdot 10^{-13}$ g/g ($\hat{=}$ 27 μBq/g) for ^{26}Al was measured. Therefore a background contribution in Borexino is excluded.

	Type 1	Type 2	Type 3
^{232}Th daughters	7 ng/g	220 ng/g	30 ng/g
^{238}U daughters, from ^{226}Ra and above	$\approx$ 100 ng/g	$\approx$ 100 ng/g	$\approx$ 100 ng/g
^{238}U daughters below ^{226}Ra	$<$ 1 ng/g	$<$ 1 ng/g	$<$ 1 ng/g
^{235}U daughters	$<$ 2 ng/g	$<$ 2 ng/g	$<$ 2 ng/g
K_{nat}	$<$ 10 μg/g	$<$ 10 μg/g	$<$ 10 μg/g
^{26}Al	$< 4 \cdot 10^{-13}$ g/g	$< 4 \cdot 10^{-13}$ g/g	$< 4 \cdot 10^{-13}$ g/g

Table 3.8: Mass concentrations of radioactive isotopes in aluminum. Type 1 aluminum was used for $\approx$ 350 light guides and Type 2 aluminum for the remaining 1490. Type 3 was considered but not used. The mass concentrations for the daughters of the thorium and uranium chains are equivalent concentrations, for explanation see Chapter 3.4.2.

Some measurements were repeated at MPIK Heidelberg to confirm the results. The measurements done there agree with these measurements within the quoted uncertainties.

3.4.3 Monte Carlo Simulation of Background Introduced in Borexino by the Light Guides

The total external gamma ray background in Borexino caused by the light guides has been determined by a Monte Carlo Simulation. The simulation toolkit EGS was used, as for the determination of the Ge detector efficiencies. For more details on the EGS toolkit see Chapter 3.4.2.

In the simulation, the detector is modeled as a sphere with a radius of 425 cm, containing 322 m^3 of scintillator, the Inner Vessel. It is surrounded by another sphere filled with the same solvent (Pseudoumene) as the Inner Vessel, yet non-scintillating due to the addition of DMP as a quenching agent. The gamma rays are started at a random point inside a spherical shell of which the inner radius is 629 cm (the front end of the light guide) and the outer radius is 652 cm (the rear end of the light guide). The direction in space in which the gamma rays start is chosen randomly and uniformly. All isotopes found in the aluminum samples are taken into account, with their respective activities. The characteristic gamma lines are produced with their branching ratios, only lines with branching well below 1% have been neglected. Table 3.9 on Page 65 summarizes all isotopes and their characteristic gamma lines taken into account from the ^{232}Th decay chain and Table 3.10 on Page 66 the ones from the ^{238}U decay chain. Also the 1461 keV gamma line from ^{40}K with an emission probability of 10.66% has been taken into account. Due to the massive shielding in Borexino, the simulation is very demanding in terms of computing time. Tracking the gamma rays which are created within one day inside the light guides takes approximately 4 weeks of computer time (at $\approx$ 1 GFLOP).

The external background in the fiducial volume (i.e. in the inner 100t of scintillator) due to the aluminum used in the light concentrators was determined to be $n_{conc} = (0.08 \pm 0.04)/day$ in the window between 250 keV and 800 keV ("^{7}Be-neutrino window"). This corresponds to $\approx$ 0.3 % of the neutrino signal assuming neutrino oscillations with the current best fit parameters for for the squared mass difference $\Delta m^2_{12} = 8.2 \cdot 10^{-5} eV^2$ and the mixing angle $\tan^2 \Theta_{12} = 0.39$ [BAH 04].

The contribution in this window is a little lower than the background introduced by the photomultipliers themselves, which is $(0.15 \pm 0.05)/day$. As the amplification factor for the light yield that the light guides produce is $\approx$ 2.5 the use of light guides is justified also from this point of view: in order to achieve the same light yield without light guides by additional photomultipliers the total external background would increase to $\approx 0.4\ /day$. Hence the background specifications for the light guides have been fulfilled.

The background contribution of the light guides is lower than the unavoidable in-situ cosmogenic background due to the production of radioactive ^{7}Be-nuclei ($\approx 0.35/day$) [HAG 00] which occurs in spallation processes

Isotope	γ Energy [keV]	Emission probability p [%]
^{232}Th	63.83	0.267
	140.86	0.018
^{228}Ac	209.253	3.88
	270.243	3.43
	338.322	11.3
	794.947	4.34
	911.205	26.6
	964.77	5.11
	968.971	16.2
^{228}Th	84.373	1.266
	131.613	0.136
	215.985	0.263
^{224}Ra	240.987	3.97
^{220}Rn	549.73	0.11
^{212}Pb	238.632	43.3
	300.087	3.28
^{212}Bi	727.33	6.58
	785.37	1.102
	1620.5	1.49
	39.858	1.091
^{212}Po	583.191	2
	2614.533	2.6
^{208}Tl	277.351	6.31
	510.77	22.6
	583.191	84.5
	860.564	12.42
	2614.533	99.0

Table 3.9: Gamma lines and their emission probabilities from the ^{232}Th decay chain that have been taken into account in the simulation of the background caused by the Borexino light guides. See Table 3.10 on Page 66 for the isotopes of the ^{238}U decay chain.

Isotope	γ Energy [keV]	Emission probability p [%]	Isotope	γ Energy [keV]	Emission probability p [%]
^{238}U	49.55	6.40	^{214}Bi	609.312	44.8
^{234}Th	63.29	4.8378		768.356	4.8
	92.38	2.8116		806.174	1.12
	92.8	2.772		934.061	3.03
^{234}Pa	766.38	0.294		1120.287	14.8
	1001.03	0.837		1155.19	1.64
^{234}U	53.2	0.123		1238.11	5.86
^{226}Ra	186.1	3.50		1280.96	1.44
^{214}Pb	53.226	1.11		1377.669	3.92
	241.981	7.50		1401.5	1.55
	258.79	0.55		1407.98	2.80
	295.213	18.5		1509.228	2.12
	351.921	35.8		1729.595	2.86
	785.91	0.85		1764.494	15.36
	839.03	0.63		1847.42	2.04
^{210}Pb	46.539	4.25		2118.55	1.14
				2204.21	4.86
^{210}Pb	46.539	4.25			

Table 3.10: Gamma lines and their emission probabilities from the ^{238}U decay chain which have been taken into account in the simulation of the background caused by the Borexino light guides. See Table 3.9 on Page 65 for the isotopes of the ^{232}Th decay chain.

with high energy muons intersecting the scintillator sphere.

	^{7}Be-ν window [counts/day]	pep-ν window [counts/day]
Lightguides	0.08 ± 0.04	0.20 ± 0.05
Photomultipliers	0.15 ± 0.04	0.54 ± 0.08
Expected rate	≈ 36	$0.7 - -3.5$

Table 3.11: Background in Borexino: Comparison between the contributions of the lightguides and the photomultipliers. The ^{7}Be-ν window will be 250 – 800 keV and the pep-ν window 800 – 1300 keV.

In the so called pep-neutrino window (0.8 - 1.5 MeV) the background introduced by the light guides is $n_{conc} = (0.20 \pm 0.05)$/day and accounts only for $\approx$ 25 % of the total background of photomultipliers plus light guides. Since the pep-neutrino flux is much lower, the background to signal ratio here is $\approx$ 5.7 % for no-oscillations and $\approx$ 11 % for the current best fit oscillation parameters. With that, the radiopurity of the light guides is good enough to allow solar neutrino measurements also in this energy region. It should be expected though that contributions from other sources (like the photomultiplers) to the total external background will increase this number. In addition the in-situ cosmogenic background due to ^{11}C-decays will dominate with $\approx$ 11 counts/day [HAG 00]. Also the requirements to the internal radiopurity of the scintillator are very challenging. In order to allow pep-neutrino measurements the concentrations in uranium and thorium should be below 10^{-17} g/g or 10^{-13} Bq/g. Due to this, the feasibility of a solar pep-neutrino measurement is not clear yet.

Table 3.11 on Page 67 gives a summary of the background introduced by the light guides compared to the expected neutrino signal and other sources of background.

The background simulation was also performed for a different scintillator (PXE) which was considered for use in Borexino instead of the Pseudocumene (PC) based scintillator. PXE has the great advantage that its density is 0.99 g/cm^3 compared to 0.889 g/cm^3 for PC, resulting in a 11.4% higher target mass. In addition, as the density of the buffer liquid has to be matched to the density of the scintillator to avoid buoyant forces on the Inner Vessel, the use of PXE scintillator would have also increased the shielding capacity of the buffer considerably. The background introduced by the light guides in the ^{7}Be ν-window in 100t fiducial volume is only 0.04 ± 0.02 counts/per in the case of PXE scintillator. However, the decision was taken to use Pseudocumene.

3.5 Conclusion

Light collection mirrors ("Light Guides") with high photon collection efficiency have been realized for the Borexino solar neutrino experiment the CTF experiment. The use of light guides allows both experiments to achieve good energy and position resolution and alpha-beta separation with a relatively small number of photomultipliers. The light yield amplification achieved in the CTF is 8.8 and in Borexino it is 2.5. A CTF light guide costs only about 12% and a Borexino light guide 5% of a fully equipped photomultiplier, therefore a substantial amount of money could be saved by using light guides. In addition, the background introduced by the light guides is negligible, which is a great advantage over the use of more photomultipliers. The light guides have shown to be compatible with the organic solvent Pseudocumol and with ultra pure water for a long period of time ($\approx$ 10 years).

Chapter 4

Source Calibration System for Borexino

4.1 Motivation

As there is no tag to the neutrino signal in Borexino, radioactive background presents the main difficulty in the experiment. In addition to shielding by water and the buffer liquid a fiducial volume cut on the scintillator volume suppresses external gamma-ray background. This fiducial volume cut reduces the active detector mass to approximately 100 tons. In order to be able to apply a fiducial volume cut, event-by-event position information is required, which can be achieved by analyzing the signal timing across all PMTs. This is a fairly complicated analysis which needs to be verified and also calibrated with calibration sources at different, but known locations within the detector.

Radioactive nuclei, dissolved or suspended, in the scintillator present another source of background for Borexino. Although very powerful purification techniques specially developed for the Borexino scintillator are used (distillation, water extraction and filtering with silica gel), further background suppression is still necessary. A means to achieve this is to distinguish between α- and β-particles by pulse shape analysis, which also requires calibration by radioactive sources with precisely known properties. To further disentangle the signal from the background in Borexino, a precise energy calibration of the detector is needed , which is dependent on the spatial position of an event, and therefore, requires the use of a radioactive source at various known positions in the detector.

4.2 System Overview

Different approaches to placing a radioactive source at exactly known locations in the detector have been considered. One is to have a mechanical system accurate enough so that it is possible to move the source exactly to a desired point in space. Due to cost considerations we pursued a second approach though: a system that has only limited mechanical accuracy in placing the source, combined with a measuring system that is able to exactly determine the location where the source has been put (see Figure 4.1 on Page 71) For our purpose, the main goal is to know the exact location of the calibration source, rather than being able to move it to an exact location.

4.3 Source Insertion System

4.3.1 Overview

The source insertion system (Figure 4.1 on Page 71), consists of 1 meter long rigid interconnecting stainless steel rods that are neutrally buoyant in the scintillator. To achieve the same average density as the scintillator, the stainless steel rods are hollow, with steel wire as balancing weight inside. One of the stainless steel rods has a hinge that can bend up to 90 degrees. This allows to move the source off of the vertical axis. The arm that holds the source at its end can be lifted with a teflon tube that exits the detector in the clean room on top of the water tank.

The source insertion system is operated from and also stored in a glove box in a class 10 cleanroom on top of the Borexino water tank in order to avoid contamination of the scintillator.

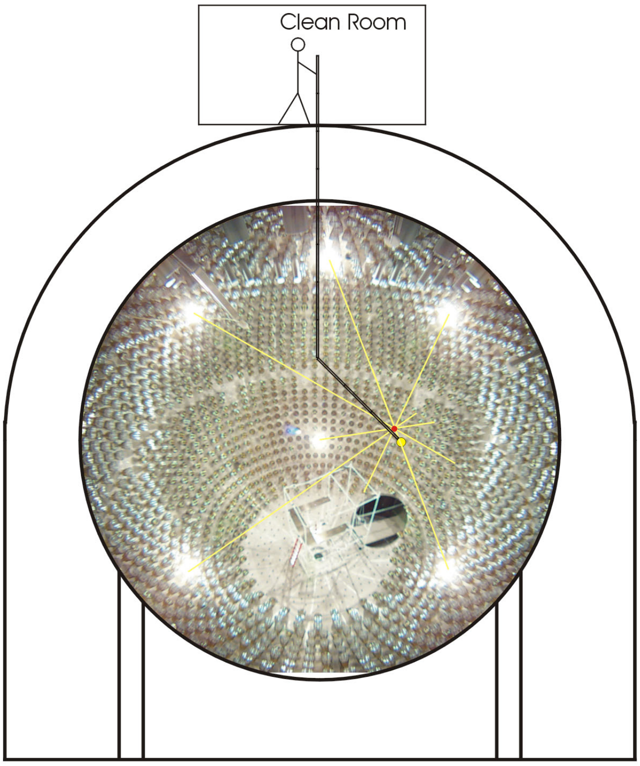

Figure 4.1: Illustration of the source calibration system. The operator can insert a radioactive source (yellow) from the clean room on top of the Borexino detector. The source insertion rod consists of 1 m long pieces that can be disconnected for storage in the cleanroom. The source LED (red) is mounted close to the source. Triangulation of the LED from seven cameras (yellow lines) allows the determination of the source's position. Only six cameras can be seen in this picture. The cameras appear as bright spots, as they provide the light source for this picture. While the picture was taken, that camera's lights have been turned off. The source insertion rod has a hinge that allows movement of the source off the vertical axis.

4.3.2 Positioning Accuracy

The seasonal variation of the solar neutrino flux on earth due to the eccentricity of the earth's orbit around the sun may help to disentangle the neutrino signal from background in Borexino. While there is a 7 % amplitude in the annual variation of the solar neutrino counting rate due to $1/r^2$, the background signal stays unaffected. In order to perform this signal-background separation, uncorrelated variations in the signal + background counting rate need to be considerably smaller than the 7 % change in the neutrino counting rate.

A main cause for the long-term variation of signal and background will be the definition of the fiducial volume (see Chapter 2. The fiducial volume cut relies on the position reconstruction of each event, i.e. it is a software cut. The accuracy of the position reconstruction (and its stability in time) will be tested with the internal source system and, if necessary, the position reconstruction process can be calibrated with it. We aim for a 2 % error in the fiducial volume, which implies a 2 % error in the total signal + background rate. With the radius of the fiducial volume of 300 cm, this means an error of ±2 cm in the radius. Therefore the design goal for the positioning accuracy of the internal source calibration system was decided to be ± 2 cm.

While the source insertion system can give some information on the location of the inserted source, it cannot provide this ± 2 cm resolution required. Therefore we built the "Source locating system", which will be discussed in the following chapter.

4.4 Source Locating System

4.4.1 Overview

The Source Locating System is designed to find the position of the radioactive source inside the detector with an accuracy of ± 2 cm. The source insertion rod (see Chapter 4.3) carries a red LED (*L*ight *E*mitting *D*iode) at its tip, very close to where the actual radioactive source is mounted. This LED can be turned on and then photographed by the seven digital cameras of the

Source Locating System. The cameras look inside the detector from different vantage points, thus one can project a ray in space from each camera to the LED and find the LED at the point where all seven rays intersect (Figure 4.1 on Page 71).

Although only two cameras would be required to give the information, we used seven cameras to increase the spatial resolution and to have redundancy in the system in case a camera fails during the operational period of Borexino. Replacing a camera is not feasible as it would require the Borexino water tank to be emptied and refilled afterwards, which takes approximately one year.

The cameras used are standard Kodak digital cameras "DC290" and each is equipped with a Nikon FE-8C fisheye lens. The fisheye lens increases the field of view enough so that the cameras can see the entire IV. The camera-lens system is mounted in a stainless steel housing on the SSS. Each camera sits behind a glass dome used for underwater photography. The glass dome is spherical to minimize the effect of refraction which has to be corrected in the analysis of the pictures. An illustration of the camera housing and mounting design can be seen in Figure 4.2 on Page 74.

A computer located in the cleanroom on top of the Borexino water tank controls the cameras via a relay system. The cameras normally use a universal serial bus (USB) connection, but as this is limited to a maximum cable length of $\sim$6 meters, we incorporated USB extenders in the system that are capable of transmitting the USB signal up to 100 meters via an ethernet cable.

To avoid condensation on the optical components of the system, the camera housings can be flushed with nitrogen from the outside to remove residual water vapors or scintillator.

4.4.2 Radiopurity

As mentioned in Chapter 2, external gamma rays are of concern in Borexino. Despite heavy shielding by water and the buffer liquid, high energy gamma rays can still reach the fiducial volume of Borexino. Especially those detector components which are inside the SSS (Stainless Steel Sphere) can be dangerous sources of gamma rays in this respect because they are inside the water shield.

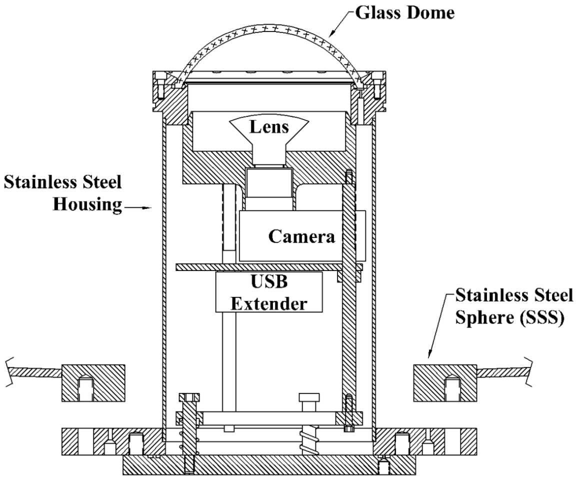

Figure 4.2: Illustration of the camera housing and mounting design.

The camera system which is used to locate the internal source (also referred to as the *Source Locating System*) is mounted on the SSS with the same shielding depth as the photomultiplier tubes. This allows us to estimate the background contribution of the Source Locating System by scaling the Monte-Carlo results for the gamma ray background caused by radioactive impurities in the photomultiplier tubes [CAD 01].

The nuclides of greatest concern here are ^{238}U, ^{232}Th and ^{40}K, because of their natural abundances and the fact that either these nuclides themselves or their daughters create high energy gamma rays (i.e. > 1 MeV). The activities of these isotopes in the different parts of the source locating system are shown in Table 4.1.

	^{238}U	^{232}Th	^{40}K
Cameras	9.1 ± 1.4 Bq	14.0 ± 1.4 Bq	42 ± 11 Bq
Fisheye lens	≈ 0 Bq	≈ 0 Bq	980 ± 175 Bq
Glass Dome	21 ± 4 Bq	3.5 ± 0.7 Bq	6.8 ± 1.1 kBq
USB extender	1.6 ± 0.2 Bq	1.9 ± 0.3 Bq	2.1 ± 0.1 Bq
Camera System total	32 ± 4 Bq	19.4 ± 1.6 Bq	7.8 ± 1.1 kBq

Table 4.1: Activities of the radioactive isotopes ^{238}U, ^{232}Th and ^{40}K in the Camera System. For ^{238}U and ^{232}Th secular equilibrium is assumed.

The Source Locating System thus will contribute to the background counting rate in Borexino with 0.02 ± 0.01 counts/day in the fiducial volume and the energy window between 250 keV and 800 keV. The total external gamma ray background counting rate expected in Borexino in this energy window (without the contribution of the Source Locating System) is 0.18 ± 0.05 counts/day [CAD 01], and the expected neutrino signal is 33 counts/day. In conclusion, the Source Locating System contributes 10 % to the external gamma ray background in Borexino. Table 4.2 summarizes this result.

	^{7}Be-ν window [counts/day]
Camera System	0.02 ± 0.01
Other Detector Components	0.18 ± 0.05
Solar ν rate	≈ 36

Table 4.2: External gamma ray background in Borexino compared to the expected solar ν counting rate. The event rates are in counts/day in the fiducial volume and in an energy window between 250 keV and 800 keV.

4.4.3 Locating Method

As mentioned in Chapter 4.4.1, triangulation of the LED mounted at the end of the source insertion rod determines the location of the calibration source. All seven cameras simultaneously take a picture of the inside of the SSS with the Source LED turned on.

An automatic image analysis process (see the description of the software in Chapter 4.4.5.4) then finds the pixel coordinates of the LED on each of the seven pictures:

$$(x_j, y_j)\,, j = 1, 2, ...7 \tag{4.1}$$

In order to be able to project a ray from a camera it would be necessary to track the light through the camera's lens system. This requires detailed information about the lenses, i.e. their shapes, relative positions and indexes of refraction. Unfortunately, the camera manufacturers do not disclose this information. Additionally, it would be necessary to know the position and orientation in space of each camera very precisely. To overcome all these difficulties, we used a different approach.

The passage of the light through the optical system of the camera is accounted for by a radial image transformation using five free parameters. Six additional free parameters account for the camera's orientation in space, the CCD position and the pixel size of the CCD. These eleven parameters are determined by analyzing pictures taken by each camera that show the inside of the SSS. The known mounting positions of Borexino's 2214 Pmts are used in a fit routine that optimizes all eleven parameters until the transformation from pixel coordinates on the image to a direction in space $(x, y) \longrightarrow (\vartheta, \varphi)$ can be performed accurately enough.

The four steps in this transformation are: image shift, radial correction, scaling and finally coordinate transformation. These steps will be described below in detail.

First, the image is shifted along the x- and y-axes by x_0 and y_0 to account for a misalignment of the camera's CCD chip with the optical axis (Figure 4.3 on Page 76). The resulting shifted pixel coordinates then are:

$$\begin{pmatrix} x_s \\ y_s \end{pmatrix} = \begin{pmatrix} x - x_0 \\ y - y_0 \end{pmatrix} \tag{4.2}$$

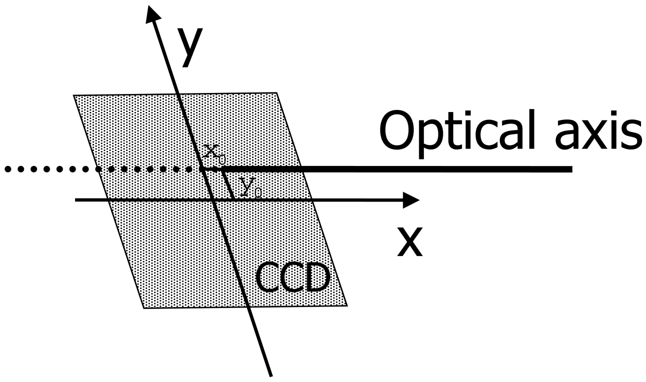

Figure 4.3: Misalignment of the CCD imager and the optical axis. The CCD is shifted by x_0 and y_0

Each picture taken is then transformed using a radial correction, which accounts for the mapping of the 3-dimensional space onto a 2-dimensional plane through the lens system. This introduces five additional parameters c_1, c_3, c_5, c_7 and c_9.

$$r_{corr} = \sum_{i=1,3,5,9} c_i r^i \tag{4.3}$$

c_i: *lens correction parameters*

with

$$r = \sqrt{(x_s^2 + y_s^2)} \tag{4.4}$$

The resulting pixel coordinates after the radial and CCD shift corrections are:

$$\begin{pmatrix} x \\ y \end{pmatrix}_{corr} = r_{corr} \begin{pmatrix} cos\delta \\ sin\delta \end{pmatrix} \tag{4.5}$$

with

$$cos\delta = \frac{x_s}{\sqrt{x_s^2 + y_s^2}} \tag{4.6}$$

$$sin\delta = \frac{y_s}{\sqrt{x_s^2 + y_s^2}} \tag{4.7}$$

The complete transformation function $\binom{x}{y}_{corr} = f\binom{x}{y}$, using equations (4.1) through (4.7), is then:

$$\begin{pmatrix} x \\ y \end{pmatrix}_{corr} = \begin{pmatrix} x - x_0 \\ y - y_0 \end{pmatrix} \sum_{i=1,3,5,9} c_i \left(\sqrt{(x - x_0)^2 + (y - y_0)^2} \right)^{i-1} \tag{4.8}$$

nachrechnen!

After this transformation, a ray can be projected in space from the center of the optical system (the idealized pinhole) through the LED's coordinates in the picture, (x_{corr}, y_{corr}). This requires information about the distance of the CCD to the pinhole and the size of a pixel on the CCD (Figure 4.4 on Page 78). The two angles φ and ϑ that define the ray are calculated as follows:

$$\cos\varphi = \frac{x_{corr}}{\sqrt{x_{corr}^2 + y_{corr}^2}} \tag{4.9}$$

$$\tan\vartheta = \sqrt{x_{corr}^2 + y_{corr}^2} \cdot \frac{d_{pixel}}{z_{CCD}} \tag{4.10}$$

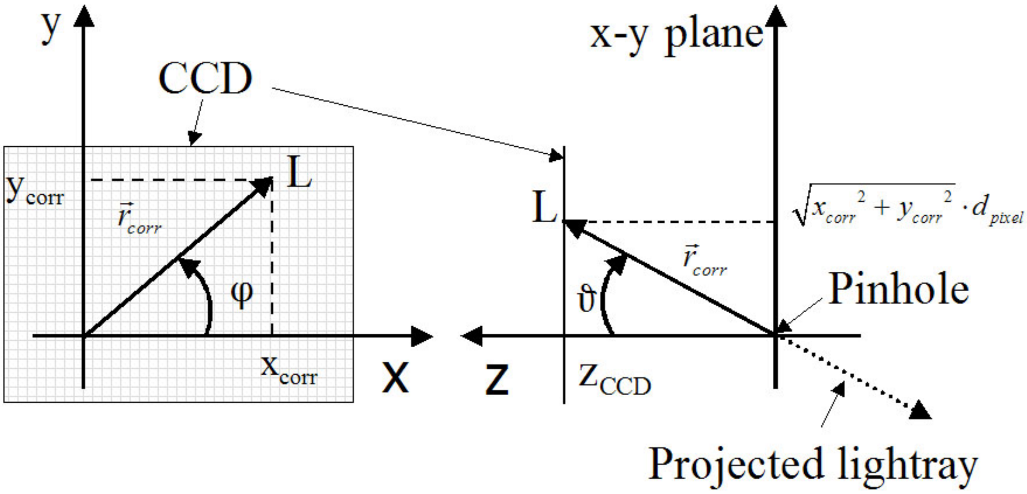

Figure 4.4: The path of a lightray in the camera system. Point L is the LED's picture. It is at the coordinates (x_{corr}, y_{corr}) in the CCD plane. The light ray is projected from the pinhole of the optical system, which is at the origin of the coordinate system, through point L. The CCD plane is parallel to the x-y plane at a distance z_{CCD} from the pinhole. The light ray is then defined by its origin (the pinhole), and the two angles φ and ϑ.

The physical size of a pixel on the CCD d_{pixel} and the distance of the CCD to the pinhole z_{CCD} are both unknown. As only their ratio $\frac{d_{pixel}}{z_{CCD}}$ is needed, see equation (4.10), it will be replaced in the following by one more fit parameter named d.

$$d = \frac{d_{pixel}}{z_{CCD}} \tag{4.11}$$

This ray in space, which is defined by its point of origin, namely the center of the optical system, and the two angles φ and ϑ, needs to be transformed from the camera's coordinate system into the absolute coordinates system of the Borexino Detector. Each camera's mounting position (x_c, y_c, z_c) on the SSS is known accurately enough to do this. The camera's orientation in space however can not be measured accurately enough. All cameras point to the center of the SSS, and the deviation from this ideal orientation is described by three additional fit parameters α_{yaw}, α_{pitch} and α_{roll} (Figure 4.5 on Page 80). The coordinates are transformed to correct for this misalignment of the camera by rotating the coordinate system around the three axes:

$$\begin{aligned} \begin{pmatrix} x' \\ y' \\ z' \end{pmatrix} = &\underbrace{\begin{pmatrix} \cos(\alpha_{yaw}) & \sin(\alpha_{yaw}) & 0 \\ 0 & 1 & 0 \\ -\sin(\alpha_{yaw}) & \cos(\alpha_{yaw}) & 0 \end{pmatrix}}_{\text{undo yaw}} \cdot \underbrace{\begin{pmatrix} 1 & 0 & 0 \\ 0 & \cos(\alpha_{pitch}) & \sin(\alpha_{pitch}) \\ 0 & -\sin(\alpha_{pitch}) & \cos(\alpha_{pitch}) \end{pmatrix}}_{\text{undo pitch}} \\ &\cdot \underbrace{\begin{pmatrix} \cos(\alpha_{roll}) & -\sin(\alpha_{roll}) & 0 \\ \sin(\alpha_{roll}) & -\cos(\alpha_{roll}) & 0 \\ 0 & 0 & 1 \end{pmatrix}}_{\text{undo roll}} \cdot \begin{pmatrix} x \\ y \\ z \end{pmatrix} \end{aligned} \tag{4.12}$$

After this correction for the misalignment of the cameras, a standard coordinate transformation from each camera's coordinate system to the detector's coordinate system can be done. By taking two arbitrary points on a ray in the camera's system and transforming them to detector's system one obtains the ray in the detector's reference frame. The source LED ideally is at the intersection of all seven rays form the cameras. As there is an inaccuracy in the determination of each ray (error analysis in Chapter 4.4.6), the seven rays won't intersect in one point. Therefore the point in space which is closest to all seven rays is taken as the location of the source LED.

Each camera has been calibrated using between 100 and 200 Pmts as points of reference. A description of the calibration process is given in the following Chapter 4.4.4.

4.4.4 Calibration of the System

Before the system can be used to locate sources it has to be calibrated. Each camera is given a set of reference points that connect pairs of pixel coordinates (x_i, y_i) with a direction in space (ϑ_i, φ_i). This set of reference points can then be used to find and optimize the 11 transformation parameters x_0, y_0, c_1, c_3, c_5, c_7, c_9, d, α_{yaw}, α_{pitch} and α_{roll}, see Chapter 4.4.3. As there are more than

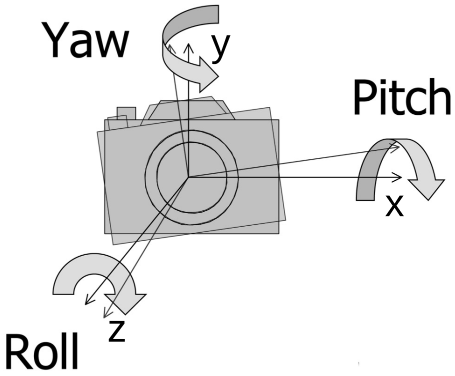

Figure 4.5: Each camera's position in space is determined by its coordinates x_c, y_c, z_c and its orientation. All cameras are mounted to point to the center of the Stainless Steel Sphere. The deviation from this ideal orientation is accounted for by the three rotation angles α_{roll}, α_{pitch} and α_{yaw}.

100 reference points used for each camera, defining them is a tedious process. A software was created for this purpose which provides a graphical interface that lets the user match up reference points, see Figures 4.6 and 4.7.

Using the transformation parameters described above, a raytracing routine calculates for each pixel of a picture the corresponding point on the SSS, where the light ray originated. In the first step this is done with estimated values for each parameter. The raytracing program draws a blue circle in the picture where the opening of a light guide is. This picture is then overlaid to a real photograph. The software allows the user to drag the generated picture over the real photograph to align the blue circles with the light guides. When a point matches up very well, the user can define this point as a reference point and the software stores this points coordinates. After defining a few reference points, the user starts a fitting routine that optimizes the transformation parameters so that these calibration points match up as good as possible. Then a new raytracing picture can be generated, which will be closer to the real photograph than the first one. Now the user can continue to add more reference points. This process has to be repeated several times until the whole raytraced image matches up with the real picture (Figure 4.7 on Page 82).

Performing this calibration of the system is a lengthy procedure despite the help of the software. It has to be noted though, that this calibration only

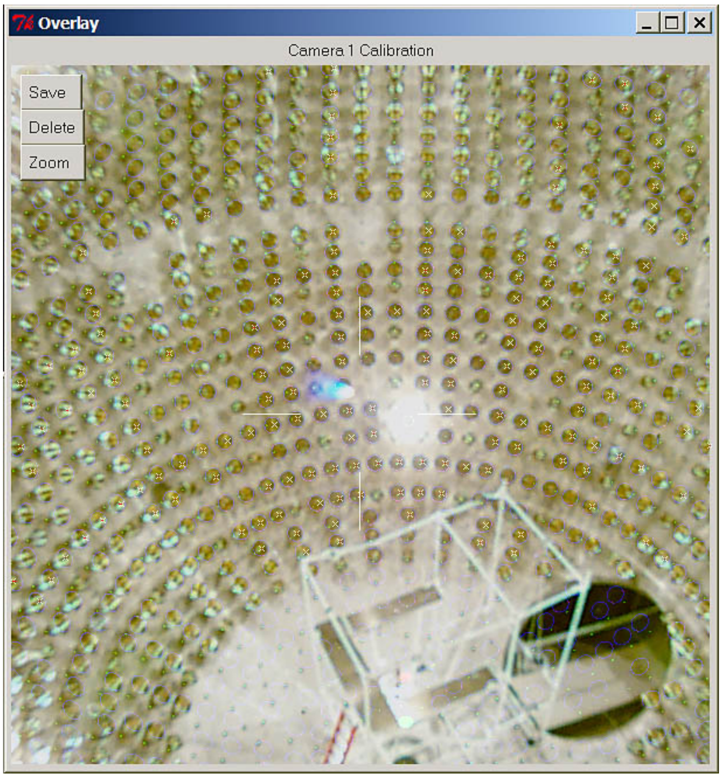

Figure 4.6: The user interface to calibrate the Source Locating System. A real picture is overlaid with a picture generated through raytracing. The generated picture has blue circles that represent the opening of the light guides. This picture can be shifted manually to match up with the photograph. After the user has matched up the two pictures in one point, this point is saved as a reference. For each camera approximately 100 calibration points have been determined.

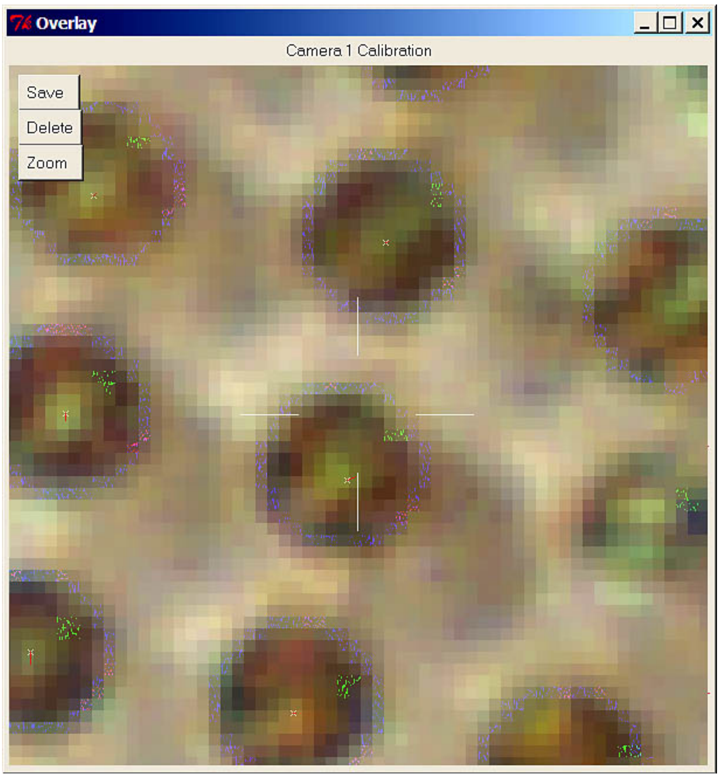

Figure 4.7: A zoomed in view of the calibration user interface. It can be seen that the blue circles of the computer generated picture line up very well with the real picture.

has to be done once, after the whole camera system is installed in its final state. Only in case a camera has to be replaced, this camera would have to be calibrated again.

4.4.5 The Operation of the Source Locating System

The process of finding the position of the radioactive calibration source in the Borexino detector is very complex. It requires a series of actions to be performed:

- Simultaneous operation of 7 cameras to take the pictures
- Controlling the lights and LEDs of the system
- Transferring the pictures to a computer
- Analysis of the pictures to find the source LED on them
- Calculate the transformation of pixel coordinates to a direction in space $(x, y) \longrightarrow (\vartheta, \varphi)$, (Chapter 4.4.3)
- Find the intersection of the seven rays and determine the source LED's position
- Calculate the actual source position from the LED position

A software has been developed which performs all the necessary actions and calculations and provides a graphical user interface for finding the source position. The main window of the software is shown in Figure 4.8 on Page 84. From here, the user can open different windows for the various functions of the software. These are: the actual locating of the source, adjustment of camera settings, taking pictures, associating the cameras with a drivename and calibrating the system.

4.4.5.1 Operation of the Cameras

All seven cameras can be operated from the Camera Control window (Figure 4.9 on Page 84). It allows to power up the system and the cameras, and

Figure 4.8: The main window of the Source Locating software. It has buttons for the different applications of this software. From left to right: find the calibration source in the detector, adjust various settings of the seven digital cameras, operate the cameras, associate each camera with a drivename, start the tools for calibrating the Source Locating System (Chapter 4.4.4)

to take pictures with one camera or several cameras at the same time. The user has to turn on the power supply, and then press the power button for each camera to turn them on. Then a number of cameras can be selected, and by pressing “Take picture” these cameras will take a picture.

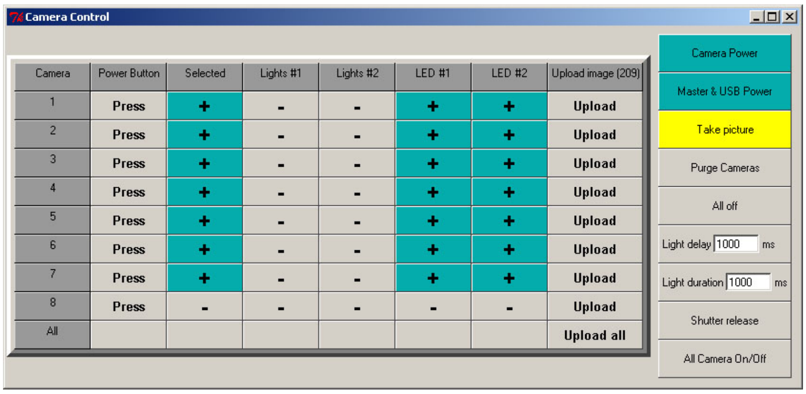

Camera	Power Button	Selected	Lights #1	Lights #2	LED #1	LED #2	Upload image (209)
1	Press	+	-	-	+	+	Upload
2	Press	+	-	-	+	+	Upload
3	Press	+	-	-	+	+	Upload
4	Press	+	-	-	+	+	Upload
5	Press	+	-	-	+	+	Upload
6	Press	+	-	-	+	+	Upload
7	Press	+	-	-	+	+	Upload
8	Press	-	-	-	-	-	Upload
All							Upload all

Light delay 1000 ms
Light duration 1000 ms

Figure 4.9: The Camera Control window. It controls the power supply and allows to turn the cameras on and off. Cameras, lights and LEDs can be selected individually to take pictures. Also, the picture files are transferred to the computer via this window.

4.4.5.2 Controlling the Lights and LEDs of the System

Each camera housing contains a set of lamps that can be used to illuminate the detector. Although not necessary for the locating of the source, it can be useful to take real pictures of the inside of the SSS for monitoring purposes. Also, the calibration of the Source Locating system needs a set of reference

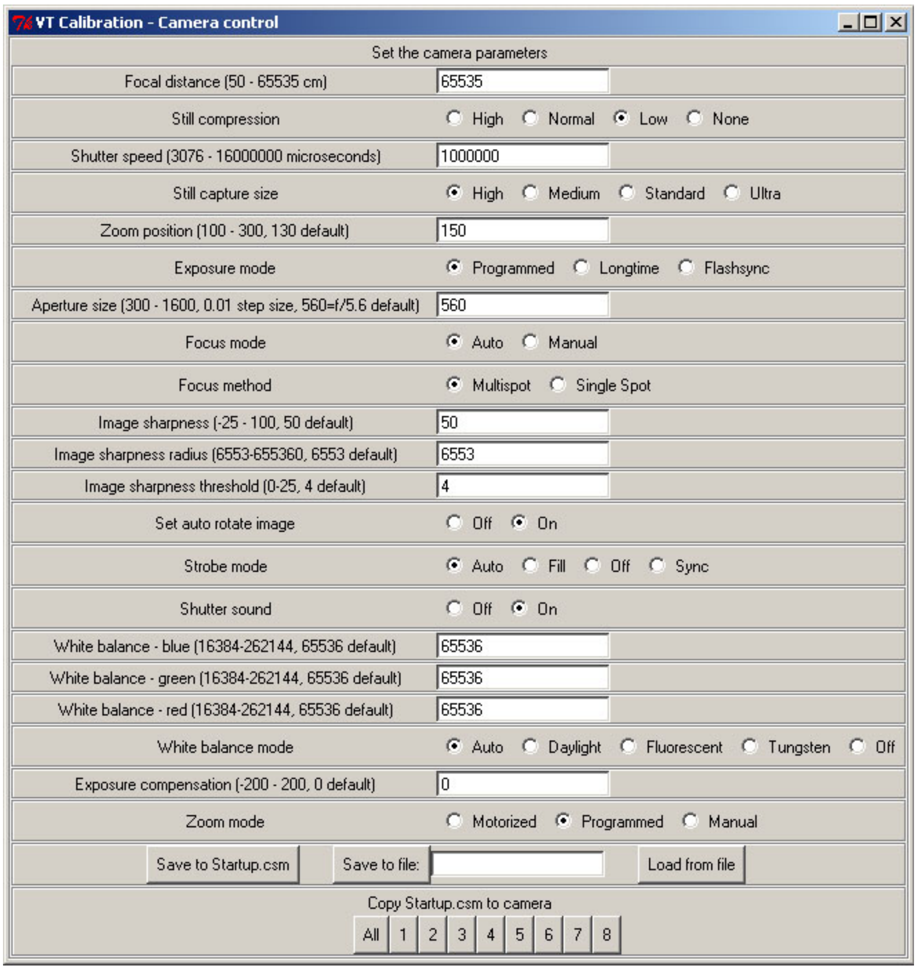

VT Calibration - Camera control

Set the camera parameters

Focal distance (50 - 65535 cm)	65535
Still compression	○ High ○ Normal ● Low ○ None
Shutter speed (3076 - 16000000 microseconds)	1000000
Still capture size	● High ○ Medium ○ Standard ○ Ultra
Zoom position (100 - 300, 130 default)	150
Exposure mode	● Programmed ○ Longtime ○ Flashsync
Aperture size (300 - 1600, 0.01 step size, 560=f/5.6 default)	560
Focus mode	● Auto ○ Manual
Focus method	● Multispot ○ Single Spot
Image sharpness (-25 - 100, 50 default)	50
Image sharpness radius (6553-655360, 6553 default)	6553
Image sharpness threshold (0-25, 4 default)	4
Set auto rotate image	○ Off ● On
Strobe mode	● Auto ○ Fill ○ Off ○ Sync
Shutter sound	○ Off ● On
White balance - blue (16384-262144, 65536 default)	65536
White balance - green (16384-262144, 65536 default)	65536
White balance - red (16384-262144, 65536 default)	65536
White balance mode	● Auto ○ Daylight ○ Fluorescent ○ Tungsten ○ Off
Exposure compensation (-200 - 200, 0 default)	0
Zoom mode	○ Motorized ● Programmed ○ Manual

Figure 4.10: The camera parameters adjustment window. The user can adjust several camera features, including the focal distance, picture compression, aperture, shutter speed, picture size, etc. The parameters are stored in a file on the computer and can be copied to each camera. The next time a camera is turned on it will read this file and change these settings to the desired values.

pictures that are taken with light, see Chapter 4.4.4. The operation of lamps inside the SSS is very dangerous because light would damage the PMTs when they are under high voltage, i.e. in operation. For safety, the lamps have a separate power supply that can only be activated with a key. Another safety issue when operating the lamps is their heat output. There are eight halogen lamps with 50 Watts each in every camera housing, i.e. a total heat output of 400 Watts. To avoid damage to the camera by overheating, the lamps can only be turned on for a limited period of time ($\approx$ 1 minute). The software controls the lamps automatically to avoid possible operation errors. The user can set the time the detector will be illuminated in the Camera Control window (Figure 4.9 on Page 84), the software then turns the lamps on when a picture is taken and turns them off afterwards. The software only allows a maximum of 10 seconds for the lamps to be turned on. Additionally, because of the severe possible damage to the system, a hardware safety relay turns the power supply to the lamps off when they stay on for more than 15 seconds.

4.4.5.3 Transferring the Pictures to the Computer

In the normal source locating process each of the seven cameras takes a picture. All seven pictures can be simultaneously transferred to the computer by pressing the “Upload all” button in the camera control window (Figure 4.9 on Page 84). The software automatically converts the pictures to the format that is needed for the ensuing image analysis during this process. The user also has the option of directly transferring single pictures without any conversion applied to them by pressing the “Upload” button for that camera.

The cameras are connected to the computer via USB. They appear as external drives in the Windows environment. Each camera has a drive letter, which depends on the order in which the cameras were turned on, because Windows assigns the drive letters in alphabetical order by itself. For the source locating process it is crucial though for each camera to have a unique identifier. This is achieved by putting a unique file on each camera that contains that camera’s identifying number. By pressing the button “Associate cameras” in the main control window (Figure 4.8 on Page 84), the software looks for that file on each camera and associates each drive letter with the corresponding camera number. This means that for correct operation of the system, the user has to press the “Associate cameras” button once after all the cameras have been turned on.

4.4.5.4 Analysis of the Pictures and Determination of the Source Position.

The next step in the source locating process is to analyze each of the seven pictures, find the source LED on them and determine its pixel coordinates $(x_j, y_j), j = 1, 2, ...7$. This is done automatically for all seven pictures by pressing “Auto find LED” in the Source Locating window, Figure 4.11 on Page 88. After this, by pressing the “Reconstruct” button, the transformation of pixel coordinates to a direction in space $(x, y) \longrightarrow (\vartheta, \varphi)$ is performed for each picture, and the resulting seven rays are intersected to find the LED’s coordinates, as described in detail in Chapter 4.4.3. The software then will display the result in (x, y, z) coordinates for the source LED, and also for the actual calibration source, which is at a distance of $\approx$ 2.5 cm from the source LED, see also Figure 4.1 on Page 71. The software also lets the user verify the result in several ways. It is possible to display each of the seven pictures zoomed in on the source LED to see whether the automatic image analysis process found the LED in the right spot. This may be important in the case there was a second source of light present and the image analysis recognized this other light source as being the source LED, which would lead to a false result later on. The user can also interfere with the image analysis to manually correct it, and even override it.

Another feature of the software is to display a certain point inside the detector. The user can enter the coordinates of a point inside the detector in the Source Locating window and after pressing “Calculate”, the software calculates the corresponding pixel coordinates for each of the seven cameras and centers the displayed image on these coordinates.

As the Source Locating Software might be used during the initial filling of the Borexino detector with water, there is a possibility to enter the water level in the Source Locating window. The raytracing algorithm will then account for the refraction of light on the water surface. More details on this will be given in Chapter 4.5.

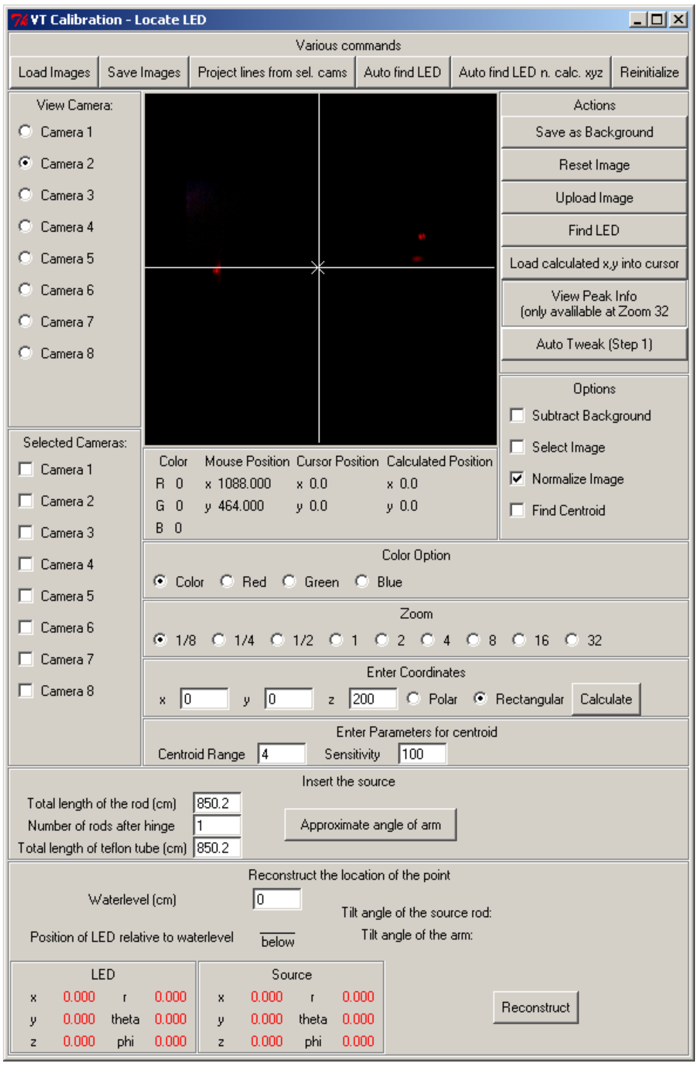

View Camera: ○ Camera 1 ● Camera 2 ○ Camera 3 ○ Camera 4 ○ Camera 5 ○ Camera 6 ○ Camera 7 ○ Camera 8

Selected Cameras: ☐ Camera 1 ☐ Camera 2 ☐ Camera 3 ☐ Camera 4 ☐ Camera 5 ☐ Camera 6 ☐ Camera 7 ☐ Camera 8

Color	Mouse Position	Cursor Position	Calculated Position
R 0	x 1088.000	x 0.0	x 0.0
G 0	y 464.000	y 0.0	y 0.0
B 0			

Options: ☐ Subtract Background ☐ Select Image ☑ Normalize Image ☐ Find Centroid

Color Option: ● Color ○ Red ○ Green ○ Blue

Zoom: ● 1/8 ○ 1/4 ○ 1/2 ○ 1 ○ 2 ○ 4 ○ 8 ○ 16 ○ 32

Enter Coordinates: x 0 y 0 z 200 ○ Polar ● Rectangular

Enter Parameters for centroid: Centroid Range 4 Sensitivity 100

Insert the source
Total length of the rod (cm) 850.2
Number of rods after hinge 1
Total length of teflon tube (cm) 850.2

Reconstruct the location of the point
Waterlevel (cm) 0
Position of LED relative to waterlevel below

LED				Source			
x	0.000	r	0.000	x	0.000	r	0.000
y	0.000	theta	0.000	y	0.000	theta	0.000
z	0.000	phi	0.000	z	0.000	phi	0.000

Figure 4.11: The source locating window. It provides a range of features for locating the calibration source. In normal operation though, the user only has to press "Auto find LED" and the software will find the coordinates of the source LED on all seven pictures. By pressing "reconstruct" the software will perform the the transformation of pixel coordinates to a direction in space $(x, y) \longrightarrow (\vartheta, \varphi)$, see Chapter 4.4.3 for all seven cameras and also intersect the seven rays to find the coordinates of the source LED. As the source and the source LED are not exactly at the same point on the source insertion rod, Figure 4.1 on Page 71, the actual source coordinates are also calculated and displayed.

4.4.5.5 “Tweaking” of the System.

As mentioned earlier, due to cost considerations, the cameras used are consumer grade Kodak digital cameras with a zoom lens. This created a problem that had not been foreseen in the early design phase of the project. Each time a camera is turned off, the lens will retract into the camera, and extend when the camera is turned on again. Naturally, the position of the lens after retracting and extending it again will not be exactly the same. As a result, the pictures will be shifted and scaled (slightly enlarged or smaller). An example of this is shown in Figure 4.12 on Page 89.

We overcame this problem by measuring the lens displacement after the cameras have been turned on and then correct the pictures taken for the lens displacement.

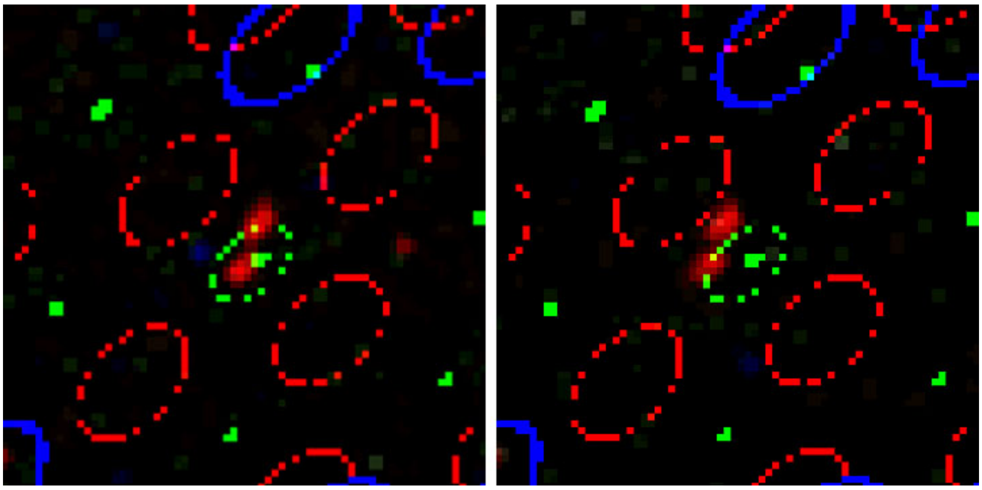

Figure 4.12: These pictures illustrate the lens displacement after turning a camera off and on again. Both pictures show the two tweaking LEDs of a camera on the opposite side on the SSS. They can be seen as red spots in the center of the pictures. The camera has been turned off after taking the first picture. A calculated reference image shows the outer rims of the concentrators (blue circles), the rim of the mu-metal shield (red circles) and the PMT mounting positions (green dots). It can be clearly seen that there is an offset of several pixels between the two pictures.

For this purpose, each camera housing is equipped with two extra LEDs (*tweaking LEDs*), see Figure 4.13 on Page 90. After turning on a camera, a picture is taken while the tweaking LEDs of all the other cameras are turned on. As the position in space of the tweaking LEDs is fixed, they can be used as a reference points. The tweaking procedure has to be done each time a camera is turned on. It is a semi-automatic process that the user initiates by pressing the button “Auto tweak” in the source locating window, see Figure 4.11 on Page 88. The software will analyze the picture to find one LED on the opposite side of the SSS. It will zoom in on it and let the user check if it is the correct LED. The pixel coordinates of that LED on the picture will then be stored. After the user accepts this first LED position, the software searches for a second one and stores these pixel coordinates also. By comparing these two coordinate pairs with the stored reference positions of the respective LEDs, the software calculates two offset parameters that allow for a shift of the picture along the y- and x-axis and one scaling parameter which allows for a linear scaling of the picture. These parameters are stored and in all further analysis processes all the pictures taken with this camera will be shifted and scaled accordingly.

maybe some formulas here

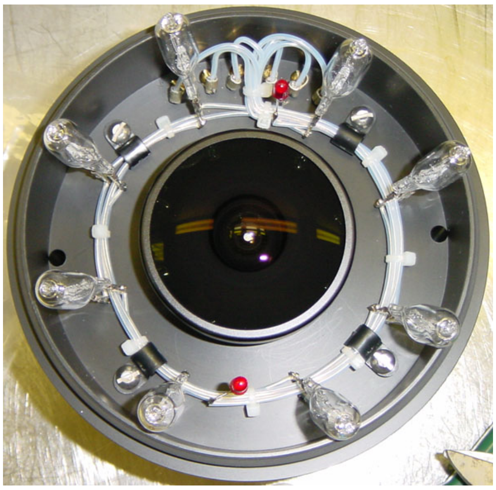

Figure 4.13: A view of the camera system. The camera itself is integrated and cannot be seen. The fisheye lens is surrounded by eight halogen lamps, which can provide illumination for observational pictures (illumination is not needed for the locating of the source). The two “tweaking” LEDs can also be seen.

4.4.6 Performance of the Source Locating System

The performance of the Source Locating System has been tested by putting a vertical string with 10 LEDs in 1 m intervals inside the SSS. Each LED's position was directly determined (independently from the Source Locating System) and then its position was measured using the Source Locating System for error analysis. A total of 130 pairs of data points $(x, y, z) \leftrightarrow (x, y, z)^{meas}$ were obtained. In the analysis of this data we found an offset of the detector's coordinate system of about 2 cm along the z-axis, which was then corrected.

The radial error u$_k$ for each data point, i.e. the distance between the measured coordinates of the point and its actual coordinates is:

$$u_k = \sqrt{\left(x_k - x_k^{meas}\right)^2 + \left(y_k - y_k^{meas}\right)^2 + \left(z_k - z_k^{meas}\right)^2} \qquad (4.13)$$

For the ensuing analysis it is assumed that the distribution of the error for each of the reconstructed coordinates x, y, z is Gaussian (this assumption will be tested later), and centered on the average value, in the form:

$$f\left(u_x\right) = \frac{1}{\sigma_x\sqrt{2\pi}} e^{-\frac{u_x^2}{2\sigma_x^2}} \qquad (4.14)$$

with

$$u_x = x - x_{meas} \qquad (4.15)$$

The same equations are valid for the cartesian coordinates y and z:

$$f\left(u_y\right) = \frac{1}{\sigma_y\sqrt{2\pi}} e^{-\frac{u_y^2}{2\sigma_y^2}} \qquad (4.16)$$

and

$$f\left(u_z\right) = \frac{1}{\sigma_z\sqrt{2\pi}} e^{-\frac{u_z^2}{2\sigma_z^2}} \qquad (4.17)$$

with

$$u_y = y - y_{meas} \quad \text{and} \quad u_z = z - z_{meas} \tag{4.18}$$

To apply this to the data, the error distribution function for each cartesian coordinate$f(u_j)$, j = x, y, z is transformed to spherical coordinates in order to obtain the radial error distribution function $f(u_r)$. It is assumed that the width of each distribution is the same, i.e. $\sigma_x = \sigma_y = \sigma_z$.

This yields:

$$f(u_r) \propto f\left(u_j\right) \cdot r^2 \quad \text{with} j = x, y, z \tag{4.19}$$

or

$$f\left(u_r\right) = \frac{C}{\sigma\sqrt{2\pi}} e^{-\frac{u_r^2}{2\sigma_r^2}} \cdot u_r^2 \tag{4.20}$$

Note here that σ is the width of the original Gaussian distribution for each cartesian coordinate.

Figures 4.14 through 4.16 show the error distributions for each cartesian coordinate x, y, z. A Gaussian fit to each dataset according to equations (4.14), (4.16) and (4.17) yields $\sigma_x = 0.78$ cm, $\sigma_y = 0.62$ cm and $\sigma_z = 0.64$ cm.

The distribution of the radial error u_r is shown in Figure 4.17 on Page 94. Fitting the distribution function $f(u)$ according to equation (4.20)to this data results in $\sigma_r = 0.67$ cm.

In conclusion the accuracy of the Source Locating System is on average ± 0.67 cm per Cartesian coordinate x$_j$, which yields an asymmetric radial error distribution

$$f\left(u\right) = \frac{C}{\sigma\sqrt{2\pi}} e^{-\frac{u^2}{2\sigma^2}} \cdot u_r^2 \tag{4.21}$$

with $\sigma = 0.67$ cm and an average error of 1.1 cm.

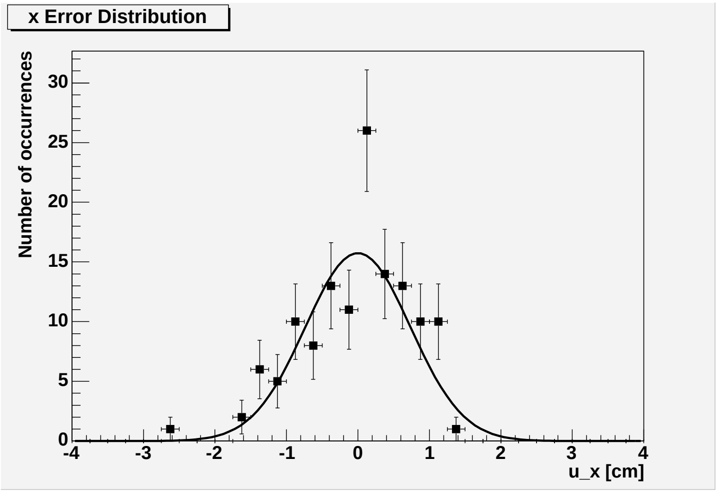

Figure 4.14: The distribution of the error u_x. A Gaussian fit yields $\sigma_x = 0.78$ cm.

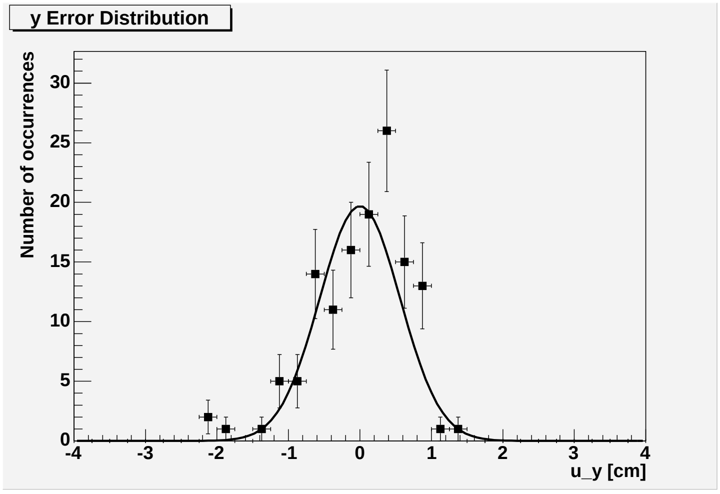

Figure 4.15: The distribution of the error u_y. A Gaussian fit yields $\sigma_y = 0.62$ cm.

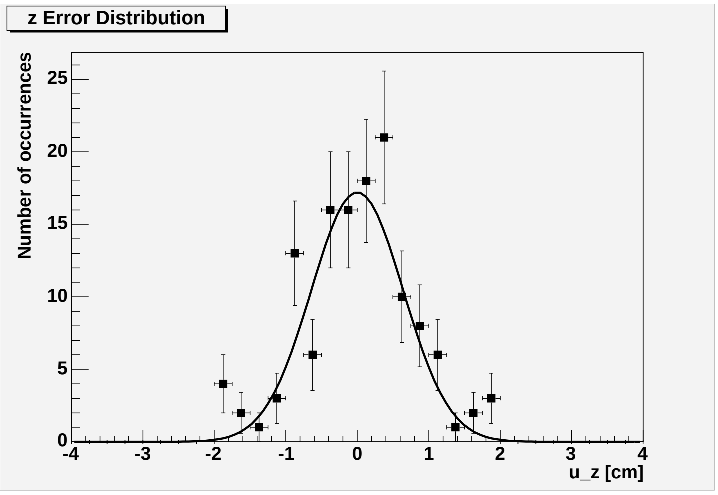

Figure 4.16: The distribution of the error u_z. A Gaussian fit yields $\sigma_z = 0.64$ cm.

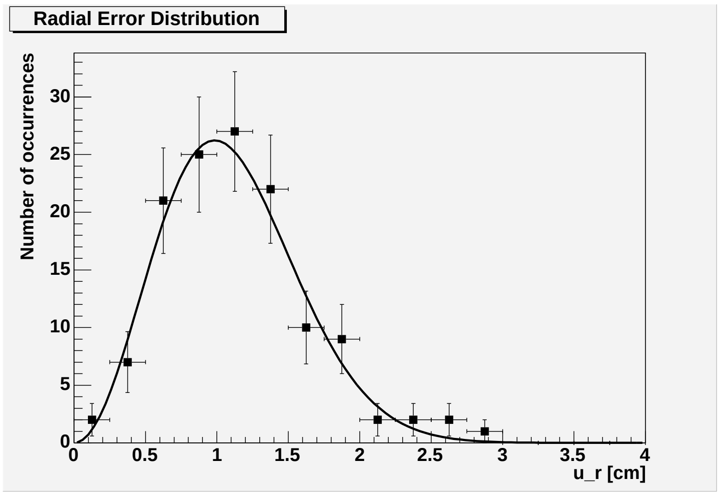

Figure 4.17: The distribution of the error u_r. A Gaussian fit yields $\sigma_z = 0.67$ cm.

4.5 Additional Benefits of the System

In addition to being used as a locating system for internal source calibration, the camera system has several other uses, most prominently monitoring of the Borexino detector during the initial filling procedure and also the operational phase.

4.5.1 Measurement of the Water Level in the SSS During the Filling Procedure of Borexino

As described in Chapter 2, the Inner Vessel of the Borexino Detector will be filled with approximately 300 tons of scintillator, surrounded by more then 1000 tons of non-scintillating buffer liquid. The initial filling of the detector will be done with ultra pure water though. Once the Inner Vessel and the buffer volume are filled with water, small amounts of this water can be taken out of the Inner Vessel and be replaced with scintillator. The benefit of this procedure compared to a direct scintillator filling is that in this way the detector is operable with full available shielding after insertion of a small amount of scintillator. Should this show that there is a purity problem with the scintillator, the operation can be reversed and additional scintillator purification can be considered. In the other scenario where the detector is filled directly with scintillator and Pseudocumene buffer, the detector can only be operated at it's full capabilities once it is completely filled and therefore has the full shielding. This operation could not be reversed though, because there is not enough storage capacity in the underground laboratory to unload the 1000 tons of Pseudocumene buffer.

Due to the difference in density between water and Pseudocumene of about 10%, approximately 20 tons of scintillator could be filled into the inner vessel with a surrounding water buffer. This would result in a buoyant force of about two tons on the Inner Vessel, which is the safety limit. After this amount, water from the buffer region has to be replaced with Pseudocumene buffer liquid to match the scintillator level in the Inner Vessel.

Accordingly, during the initial filling of the Inner Vessel and the buffer volume with water, and later during the replacement of the water with scintillator and Pseudocumene buffer, the water level in the two volumes has

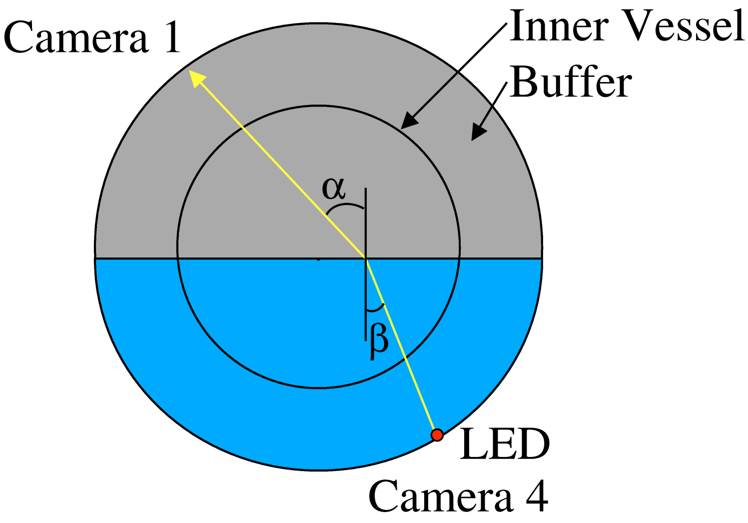

Figure 4.18: The light from a “tweaking LED” of one camera (here Camera 4) passes through the water/air interface to reach the other camera (Camera 1). The refraction on the interface shifts the position in which Camera 4 appears. This effect can be used to measure the water level in the Inner Vessel as well as the buffer region.

to be monitored precisely so that it always matches up. This monitoring is done by measuring the pressure in both volumes precisely. Yet the Source Locating System provides us with an independent measure that can be used either as a backup system or as a means of cross checking.

The principle of this water level measurement is the refraction of light on the water surface (Figure 4.18 on Page 96).

The tweaking LEDs, as described in Chapter 4.4.5.5, are used as light source. The light coming from an LED of a camera which is under water has to pass the water surface to get to one of the opposite cameras. Due to the refraction at the interface (water/air in the initial filling, later water/Pseudocumene during the replacement procedure) the position at which the LED appears as seen from that camera moves as the water level changes. This is illustrated in Figure 4.19 on Page 98. It shows the shifting of an LEDs position in the image as a function of the water level for two different cameras.

This technique can be used for measuring the water levels in the Inner Vessel as well as the buffer region. There is a restriction though, which is that it can only be used as long as the water level is in between the line of sight of two cameras. This results in the following ranges: The Inner Vessel water level can be measured between -185 cm and 365 cm, the buffer region water level between -370 cm and 365 cm.

The accuracy of this water level measurement is shown in Figure 4.20 on Page 99. It is a results of the accuracy with which each camera can determine the position of an LED and the combination of the seven measurements.

For each of the seven cameras the water level is a function of the measured pixel shift of the LED:

$$h = f\left(dp\right) \tag{4.22}$$

with h being the water level and dp the distance in pixels between where the LED is in the image and where it would be without refraction.

The error u_h of the water level is defined by:

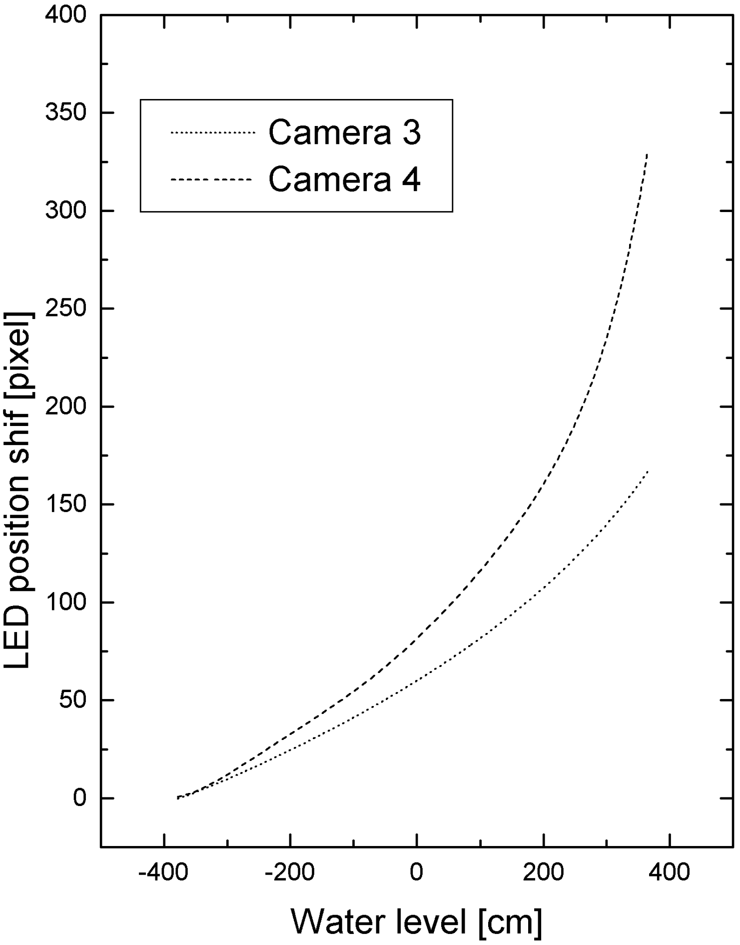

Figure 4.19: This graph shows the amount of pixels that an LED is shifted due to refraction on the water surface as a function of the water level. Due to geometric reasons there are different curves for the cameras above and under the water's surface. This is an examplary dataset for a camera above the surface (Camera 3) and one below the surface (Camera 4). Note that the range on the x-axis is -400 cm to 400 cm, these are the mounting positions of the cameras. A measurement beyond these levels is not possible because the refractive surface has to be in between the light source and the camera.

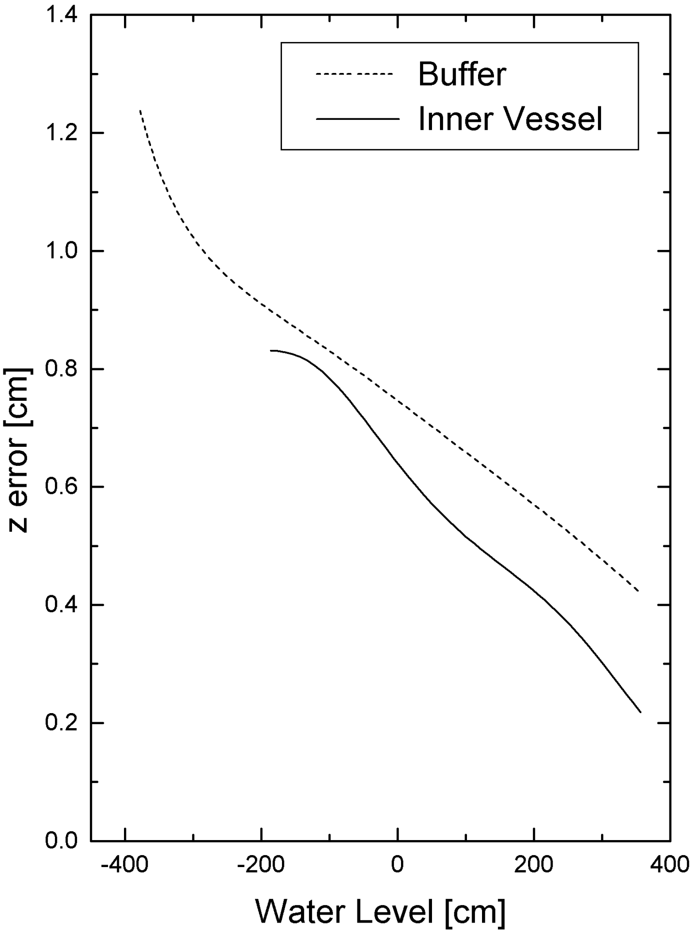

Figure 4.20: This graph shows the accuracy of the water level measurement with the Source Locating System as a function of the water level itself. The different level ranges in which a measurement can be performed can be seen. The water level can be measured with an accuracy of between 0.2 cm and 1.3 cm.

$$u_h = u_{dp} \cdot \frac{\partial f}{\partial dp} \tag{4.23}$$

where u_{dp} is the error in pixels on the position of the LED in the image.

As there are 7 cameras to measure the water level with, the measurements can be combined to a weighted average:

$$\bar{h} = \frac{\sum\limits_{i=1}^{7} w_i h_i}{\sum\limits_{i=1}^{7} w_i} \tag{4.24}$$

where the individual weight for each camera is:

$$w_i = \frac{1}{u_{p_i}} \tag{4.25}$$

The resulting error on the water level measurement combining all 7 cameras is then:

$$\bar{h} = \frac{1}{\sum\limits_{i=1}^{7} w_i} \tag{4.26}$$

This error is displayed as a function of the water level in Figure 4.20 on Page 99.

In conclusion, it is possible to use the Source Locating System to measure the water level in the Borexino Inner Vessel as well as the buffer during the filling procedure. This measurement can be done with an accuracy of between $\pm 0.2cm$ and $\pm 1.3cm$, depending on the water level. Due to geometric restrictions a measurement is only possible for a certain range of water levels, see above or Figure 4.20 on Page 99.

4.5.2 Monitoring of the Detector

The Borexino prototype detector CTF [ALI 98-1] already had a camera system installed. In this detector it was not possible though to use it as a positioning system, like in Borexino. The CTF has nylon vessel with 4 tons of Pseudocumene scintillator on the inside, surrounded by 1000 tons of water for shielding. Due to the different indices of refraction between the scintillator and the water, refraction occurs at the interface (the nylon vessel). This would not be a problem were the vessel a perfect sphere, however its shape is fairly distorted from that ideal case. As the shape can not be determined exactly enough, raytracing through the detector is impossible in the case of the CTF. However, the camera system proved to very useful during the various filling and emptying procedures in the CTF. Three volumes had to be filled at the same time, the scintillator vessel, a surrounding volume delimited by a nylon radon barrier, and the water tank. During the filling process (and also the emptying), the liquid levels in these three volumes had to always be kept at the same level so not to rupture the nylon vessels. The pictures taken with the camera system (see Figure 4.21 on Page 102) allowed to visually inspect the detector during these dangerous procedures and could be used as a cross check for the barometric level measurements.

As in the CTF, Borexino can use the Source Locating Camera System for visual inspection. Monitoring the vessels periodically will give valuable information about the shape and overall condition of the vessels, see Figure 4.22 on Page 103.

4.5.3 Raytracing Images

The software that has been developed for the Source Locating System is capable to perform raytracing inside the Borexino SSS including refraction, reflection and total reflection of visible light. This is necessary to follow a light ray from the Source LED in order to determine the direction it is coming from, and ultimately determine the position of the Source LED as described in Chapter 4.4.3.

These raytracing capabilities can also be used to generate artificial images that depict the inside of the SSS as it would look like at a certain filling level. To do this, a picture is taken from the empty detector. Then each pixel from that image is raytraced to the point of the SSS where the light ray originated, assuming an empty detector still. From this point in the detector then the light ray is traced back into the camera, this time assuming a certain filling

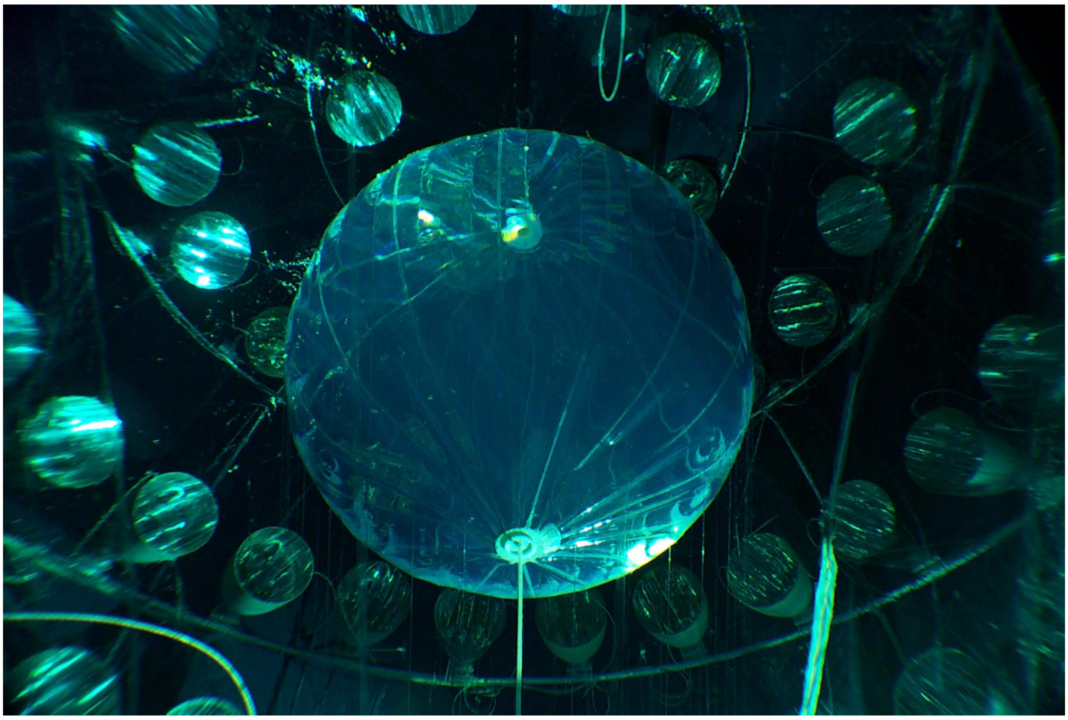

Figure 4.21: Picture of the interior of the Borexino Counting Test Facility (CTF). Taken with one of the cameras installed in CTF. In the center is the nylon vessel holding 4 tons of Pseusocumene based scintillator, the photomultipliers with their light guides (see Chapter 3) can be seen surrounding it.

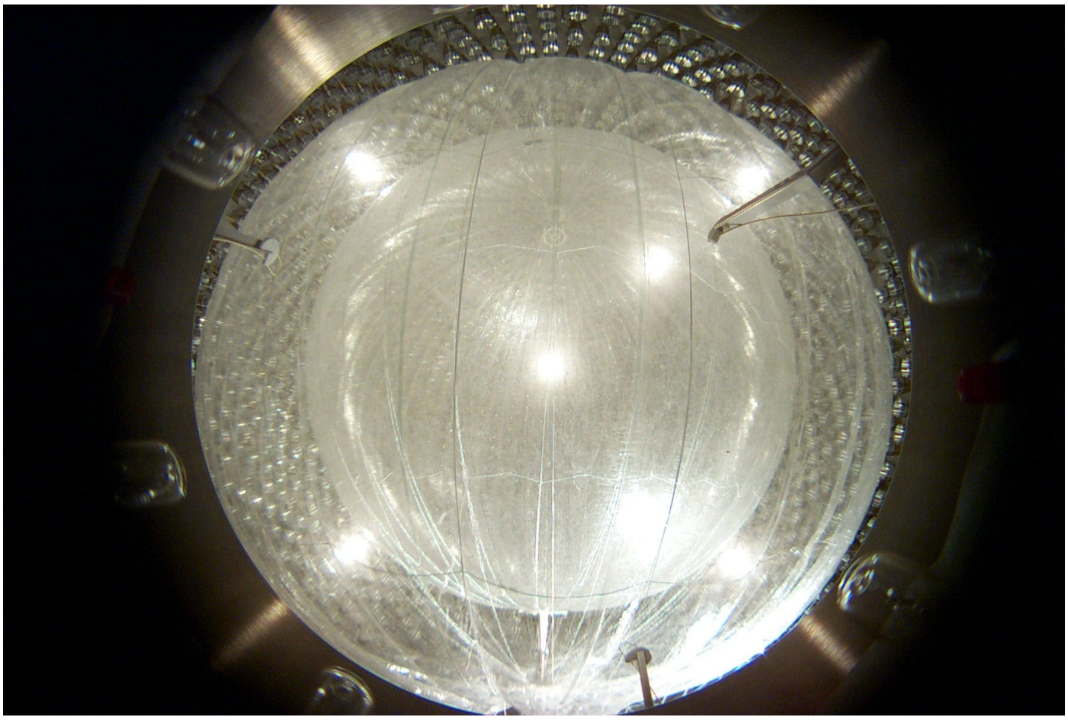

Figure 4.22: Interior view of the Borexino Detector. The picture was taken with the Source Locating Camera System. The nylon Inner Vessel and the radon shroud are already inflated.

level to find the image pixel that represents this point in the detector at this water level. This image pixel is then colored as the original starting pixel was to generate the artificial image.

This is not a one-to-one transformation in the mathematical sense though. A light ray might end up outside the field of view of the camera after it has been back traced.

Figure 4.23 on Page 105 shows a series of generated images at different filling levels. A jagged line in the images indicates that this is the end of the original image (with the empty detector), and beyond this line no information was available to create the raytraced image.

This feature will prove to be very useful when it comes to analyzing pictures taken of the filling procedure of Borexino. The experience with the CTF has shown that due to optical effects caused by refraction and reflection, and even more so by total reflection, the images seen can be very confusing and hard to understand. Raytraced images will predict these effects and help with analyzing the real images.

4.6 Conclusions

The Borexino Source Calibration System has been installed and successfully tested. The reconstruction of the position of an LED inside the Borexino Inner Vessel has an average error of 1.1 cm, which exceeds the design goal. It will allow the calibration of the Borexino detector with the desired accuracy, and it will be an essential part in the fulfillment of the detector's physics goals.

The success of the source locating system, and the added benefits of vessel positioning, in addition to being able to see the filling process makes this system invaluable to Borexino and it's physics program.

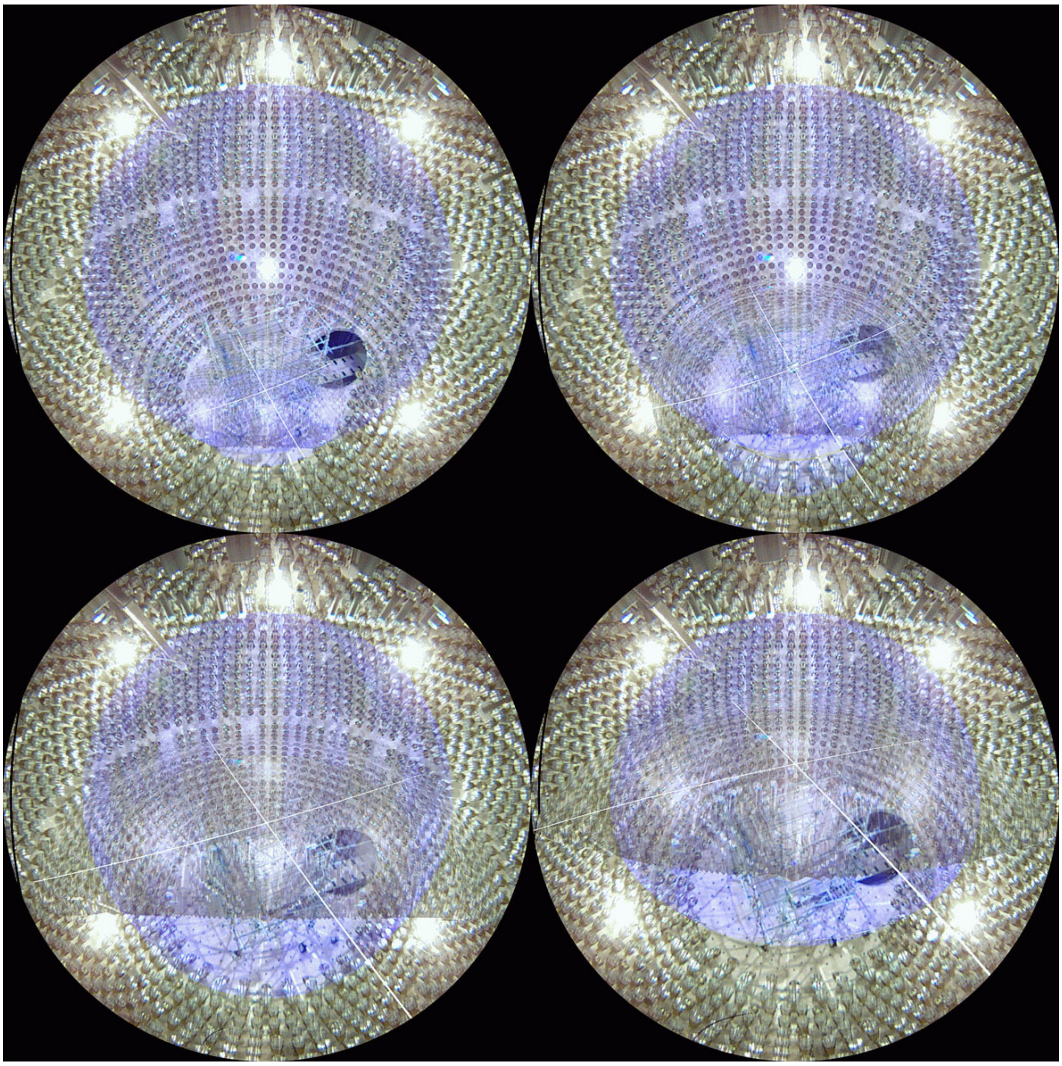

Figure 4.23: Raytracing images of the inside of the Borexino SSS. These pictures are computer generated and simulate the filling of the detector. The Inner Vessel is shown as a blue shadow. From top left to bottom right it can be seen how the water level(indicated by the white pair or crossing lines) rises. Visual effects from refraction and total reflection of the light that would otherwise be hard to understand can be seen very well. The jagged line is an artefact from raytracing, see Chapter 4.5.3 for more explanation.

Chapter 5

The Future Double Chooz Detector

5.1 Goal

Whereas the two neutrino mixing angles θ_{sol} and θ_{atm} have been measured (see Chapter 1), for the remaining neutrino mixing angle θ_{13} only an upper bound has been found so far. It is $\sin^2 2\theta_{13} < 0.2$ (at 90 % C.L. for $\Delta m^2_{atm} = 2.0 \cdot 10^{-3} eV^2$), found by the Chooz experiment ([CHO 98], [CHO 99], [CHO 00] and [CHO 03]). The new Double-Chooz experiment aims at probing $\sin^2 2\theta_{13}$ in the range between 0.2 and 0.03. This should be achieved after three years of data taking.

The Double-Chooz experiment is an augmented version of the original Chooz experiment. It will have higher statistics, a better control of the systematic errors and improved suppression of cosmic ray induced background. The use of two identical detectors, one at a distance of ≈ 150 m and one at a distance of 1.05 km from the reactor allows to eliminate the systematic uncertainty in the anti-neutrino flux generated in the reactor.

5.2 Measurement of $\sin^2 2\theta_{13}$ with Double Chooz

5.2.1 Antineutrino Production

Nuclear reactors are a very powerful source of antineutrinos. The neutron-rich fission products undergo β^--decays and emit $\bar{\nu}_e$:

$$n \longrightarrow p + e^- + \bar{\nu}_e \tag{5.1}$$

On average, 6 $\bar{\nu}_e$ are emitted per fission. The fission rate is related to the reactor power by:

$$N_f = 6.241 \cdot 10^{18} \frac{1}{s} \cdot \frac{P_{th}\,[MW]}{W\,[MeV]} \tag{5.2}$$

N_f: Number of fissions per second
P_{th}: Thermal power of the reactor
W: Mean energy release per fission

The mean energy release per fission depends on the fuel composition of the reactor. For the Chooz reactor, the average value is W = 203.87 MeV with a fuel compositon of 55.6% ^{235}U, 32.6% ^{239}Pu, 7.1% ^{238}U and 4.7% ^{241}Pu [ARD 04].

The two Chooz nuclear reactors with a combined thermal power output $P_{th} \approx 8.5$ GW thus create a total $\bar{\nu}_e$ flux of $\Phi_{\bar{\nu}_e} \approx 15.6 \cdot 10^{20} \frac{1}{s}$.

The $\bar{\nu}_e$s created in nuclear rectors have energies below 10 MeV. The actual energy spectrum depends on the fuel composition, which changes during a reactor cycle. The $\bar{\nu}_e$ energy spectrum has been carefully studied for the Chooz experiment (see Figure 5.1 on Page 109), and is known with an accuracy on the few percent level [CHO 03].

5.2.2 Detection Principle

The Double-Chooz detector will measure electron antineutrinos generated in a nuclear reactor. The detection principle is inverse beta-decay:

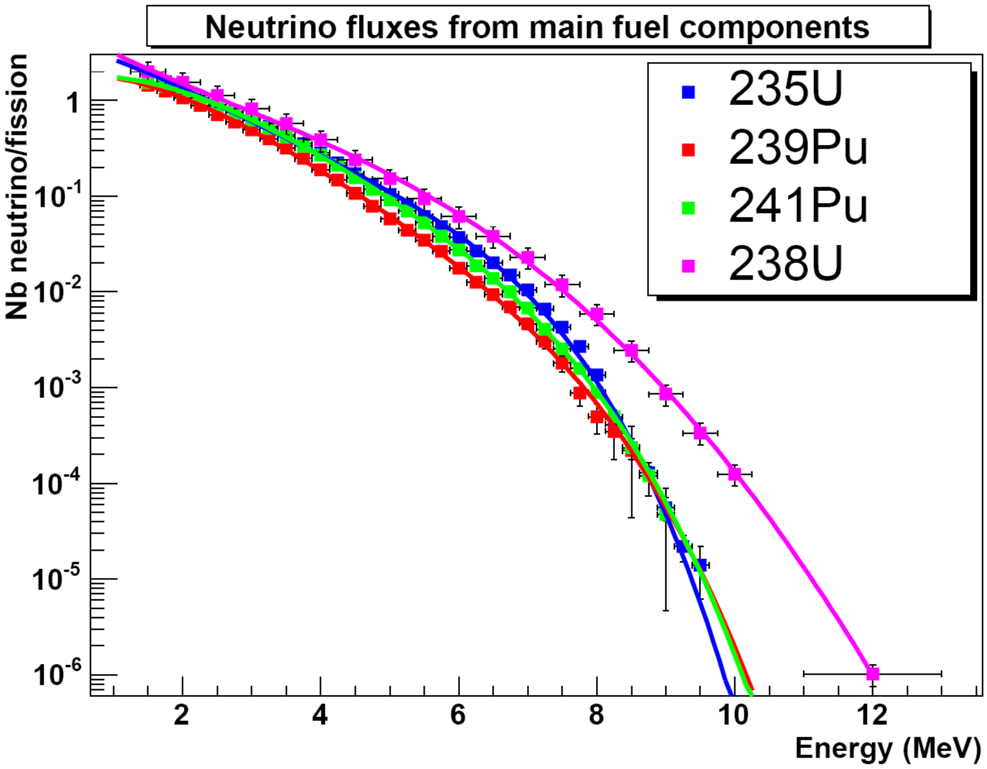

Figure 5.1: $\bar{\nu}_e$ spectra for the dominant isotopes. The spectra for ^{235}U, ^{239}Pu and ^{241}Pu have been measured, the spectrum for ^{238}U is only calculated [ARD 04].

$$\bar{\nu}_e + p \longrightarrow e^+ + n \tag{5.3}$$

The energy threshold for this reaction is 1.806 MeV. The target used is liquid scintillator with an addition of ≈ 1 g/l Gadolinium. The positron emitted in the inverse beta decay gives rise to a prompt signal in the scintillator, with the visible energy $E_{vis} = E_{e^+} + 511$ keV. The additional 511 keV are due to the annihilation of the positron. The energy of the electron antineutrino can be determined from the positron energy:

$$E_{\bar{\nu}_e} = E_{e^+} + (m_n - m_p) + O\left(E\bar{\nu}_e/m_n\right) \tag{5.4}$$

The prompt positron signal is followed by the capture of the neutron on Gadolinium with consequent gamma emission:

$$n + Gd \longrightarrow Gd^\star \longrightarrow Gd + \sum_i \gamma_i \tag{5.5}$$

This allows tagging of the neutrino signal and therefore strong background suppression. The total energy released after the neutron capture is 8 MeV with a mean gamma multiplicity of 3 - 4.

The cross section for the inverse beta decay is approximately:

$$\sigma\left(E_{e^+}\right) \approx \frac{2\pi^2\hbar^3}{m_e^5 f \tau_n} p_{e^+} E_{e^+} \tag{5.6}$$

E_{e^+}: Sum of the rest mass and kinetic energy of the positron
f: Free neutron decay phase space factor (f ≈ 1.71465) [WIL 82]
τ_n: Life time of the free neutron $\tau = (886.7 \pm 1.9)$ s [PDG 00]
p_{e^+}: Momentum of the positron

Assuming a typical fuel composition of the reactor the mean energy release per fission is 203.87 Mev (see Chapter 5.2.1). The energy weighted cross section per fission is then:

$$\langle\sigma\rangle_{fission} = 5.825 \cdot 10^{-43}\text{cm}^2 \qquad \text{per fission} \tag{5.7}$$

Note here that as this cross section is per fission, the antineutrino multiplicity is already added in.

Using Equation 5.6, the inverse beta decay event rate at a distance L from the reactor can be calculated (assuming no neutrino oscillations) as follows:

$$R_L = N_f \cdot \langle\sigma\rangle_{fission} \cdot n_p \cdot \frac{1}{4\pi L^2} \tag{5.8}$$

R_L:	Inverse beta decay event rate at distance L from the reactor
N_f:	Fission rate in the reactor
$\langle\sigma\rangle_{fission}$:	Energy weighted cross section per fission
L:	Distance from the reactor
n_p:	Number of protons in the target

With N_f from Equation 5.2, and a thermal power output of 4.27 GW$_{th}$ for each of the two Chooz reactors, the inverse beta decay event rate in Double Chooz with $\approx$ 10.2 tons of target will be $\approx 950 \cdot 10^3$ events/year for the near detector at a distance of 150 m and $\approx 19.3 \cdot 10^3$ events/year for the far detector at a distance of 1.05 Km.

5.2.3 Neutrino Oscillations

The Double Chooz experiment will measure the survival probability $P_{\bar{\nu}_e \to \bar{\nu}_e}$ of $\bar{\nu}_e$ after travelling the distance L = 1.05 Km from their point of creation in the reactor. Appearance of other neutrino flavors can not be seen because the energy of the reactor antineutrinos is too low (see Chapter 5.2.1) to create a μ or τ in a charged-current reaction.

The survival Probability $P_{\bar{\nu}_e \to \bar{\nu}_e}$ of $\bar{\nu}_e$ can be written as (assuming a normal mass hierarchy with $m_1 < m_2 < m_3$):

$$\begin{aligned}P_{\bar{\nu}_e\to\bar{\nu}_e} = \;& 1-2\sin^2\theta_{13}\cos^2\theta_{13}\sin^2\left(\frac{\Delta m^2_{31}L}{4E}\right)\\ & -\frac{1}{2}\cos^4\theta_{13}\sin^2(2\theta_{12})\sin^2\left(\frac{\Delta m^2_{21}L}{4E}\right)\\ & +2\sin^2\theta_{13}\cos^2\theta_{13}\sin^2\theta_{12}\cdot\\ & \cdot\left(\cos\left(\frac{\Delta m^2_{31}L}{2E}-\frac{\Delta m^2_{21}L}{2E}\right)-\cos\left(\frac{\Delta m^2_{31}L}{2E}\right)\right)\end{aligned} \tag{5.9}$$

Due to the low energy of the reactor antineutrinos and the short baseline of the experiment, the effects off matter enhanced neutrino flavor transitions can be neglected [MIN 02]. The last term in Equation 5.9 is not present in the two-neutrino mixing model. With $\alpha = \frac{\Delta m^2_{21}}{\Delta m^2_{31}}$ the survival probability $P_{\bar{\nu}_e\to\bar{\nu}_e}$ of $\bar{\nu}_e$ can be approximated up to the second order in $\sin 2\theta_{13}$ and α by:

$$\begin{aligned}P_{\bar{\nu}_e\to\bar{\nu}_e} \approx \;& 1-\sin^2 2\theta_{13}\sin^2\left(\frac{\Delta m^2_{31}L}{4E}\right)\\ & +\alpha^2\left(\frac{\Delta m^2_{31}L}{4E}\right)^2\cos^4\theta_{13}\sin^2 2\theta_{12}\end{aligned} \tag{5.10}$$

The last term of this equation is small and can be neglected when considering the current best fit values for the mixing parameters found in neutrino oscillation experiments [ARA 04], [ISH 04]:

$\Delta m^2_{12} = 7.9^{+0.6}_{-0.5}\cdot 10^{-5}eV^2$
$\tan^2\theta_{12} = 0.40^{+0.10}_{-0.07}$
$\Delta m^2_{23} = 2.4^{+0.6}_{-0.5}\cdot 10^{-3}eV^2$
$\sin^2 2\theta_{23} = 1^{+0}_{-0.1}$

The survival probability $P_{\bar{\nu}_e\to\bar{\nu}_e}$ is then:

$$P_{\bar{\nu}_e\to\bar{\nu}_e} \approx 1-\sin^2 2\theta_{13}\sin^2\left(\frac{\Delta m^2_{31}L}{4E}\right) \tag{5.11}$$

Therefore, the reactor neutrino Double Chooz experiment will provide a measurement of $\sin^2 2\theta_{13}$ without the influence of matter effects or parameter correlations [MIN 02], [HUB 02]. This is a great advantage over super beam experiments planned for the future, see Capter 5.5.

5.3 The Planned Design of the Double Chooz Detector

The Double Chooz detector design will be based on the original Chooz detector [CHO 03]. Improved sensitivity on $\sin^2 2\theta_{13}$ is reached by reducing the statistical as well as systematic errors. A higher target mass will produce more $\bar{\nu}_e$-events and improve the statistics. The most significant reduction of the systematic error will be achieved by using two identical detectors, a close one to monitor the $\bar{\nu}_e$-flux from the reactor (oscillation effects will be negligible due to the short distance of 150m) and a second detector at a distance of 1.05 Km which will observe the disappearance of the $\bar{\nu}_e$. Thus the systematic uncertainty in the primary $\bar{\nu}_e$-flux which at 1.9% was the biggest contribution to the systematic error in the original Chooz experiment [CHO 03] can be reduced to a negligible level.

The detector will be composed of the following elements (from the inside to the outside), see also Figure 5.2 on Page 114 and 5.3 on Page 116:

- Target

  The target for the $\bar{\nu}_e$s will be 12.7 m^3 of a liquid scintillator mixture. The development of the scintillator is still in progress, but currently a mixture of 80% dodecane and 20% PXE for the solvent is considered. Alternatives with mineral oil instead of the dodecane and pseudocumene instead of the PXE are being studied. The scintillator will be contained in an acrylic vessel of cylindrical shape (radius 120 cm, height 280 cm) which is transparent for the scintillation light.

  Added to the scintillator will be $\approx$ 0.1% of Gadolinium. It serves as a neutron capturing agent with consecutive gamma emission, see Chapter 5.2.2. Two different approaches of dissolving Gadolinium in the scintillator have been investigated with promising results: using beta-diketonates and carboxylic acids [BUC 04].

- γ-Catcher

  Due to the high energy of the gamma rays emitted after the capture of a neutron on Gadolinium (up to 8 MeV, in case of a single gamma emission), a large fraction of the gamma ray's energy could be deposited

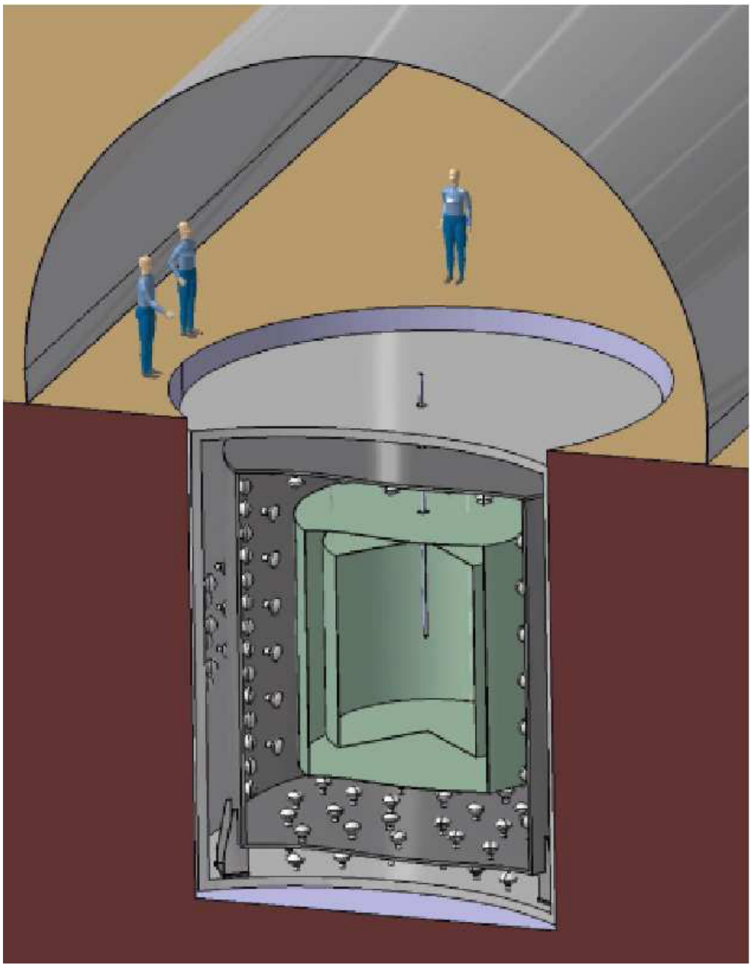

Figure 5.2: The Double Chooz far detector. The target of 12.7 m^3 dodecane+PXE based liquid scintillator loaded with $\approx$ 1 g/l Gadolinium is contained in a transparent acrylic cylinder. Surrounding the target cylinder is the γ-catcher, also dodecane+PXE based liquid scintillator, but without the addition of Gadolinium. Between the γ-catcher and the photomultipliers is $\approx 100m^3$ of non-scintillating liquid buffer. The outermost tank is filled with scintillator and equipped with photomultipliers to act as and active muon veto.

outside the target region in case the capture takes place close to the edge of target. Therefore the target volume will be surrounded by scintillator without added Gadolinium, the so called "γ-catcher". With a radius of 180 cm and a height of 400 cm this acrylic vessel will contain 28.1 m^3 of scintillator.

In addition, this scintillating buffer around the target is necessary to capture the positron annihilation photons. Due to the lower energy of these compared to the neutron capture gammas, the required thickness for this is only $\approx$ 35 cm. This value has been found in Monte-Carlo simulations.

The γ-Catcher will also be helpful in reducing the background due to fast neutrons, see Chapter 5.4. A neutron which reaches the target region from the outside must have an energy of at least 20 MeV to be able to cross the γ-catcher. Yet, at this energy it is likely that the neutron deposits more than 8 Mev in the sensitive volumes, which allows for this event to be rejected. This has been carefully studied with Monte-Carlo simulations, see Chapter 5.4.2.2.

- Buffer

  100 m^3 of non scintillating buffer will reduce the rate of uncorrelated external background, mainly due to gamma rays emitted by the photomultipliers. The size of this buffer has been determined by Monte-Carlo studies.

- Photomultipliers and Supporting Structure

  The total number of photomultiplers has not been determined yet. It is mainly a compromise between cost, background introduced by the phototubes, and and optical coverage (i.e. photoelectron yield) as it has been discussed in great detail for Borexino, see Chapter 3.

- Veto

  An active veto will be necessary for Double Chooz as discussed in Chapter 5.4 to reduce cosmic ray background. At the moment 110 m^3 of liquid scintillator are planned, but a water Čerenkov version is also being considered.

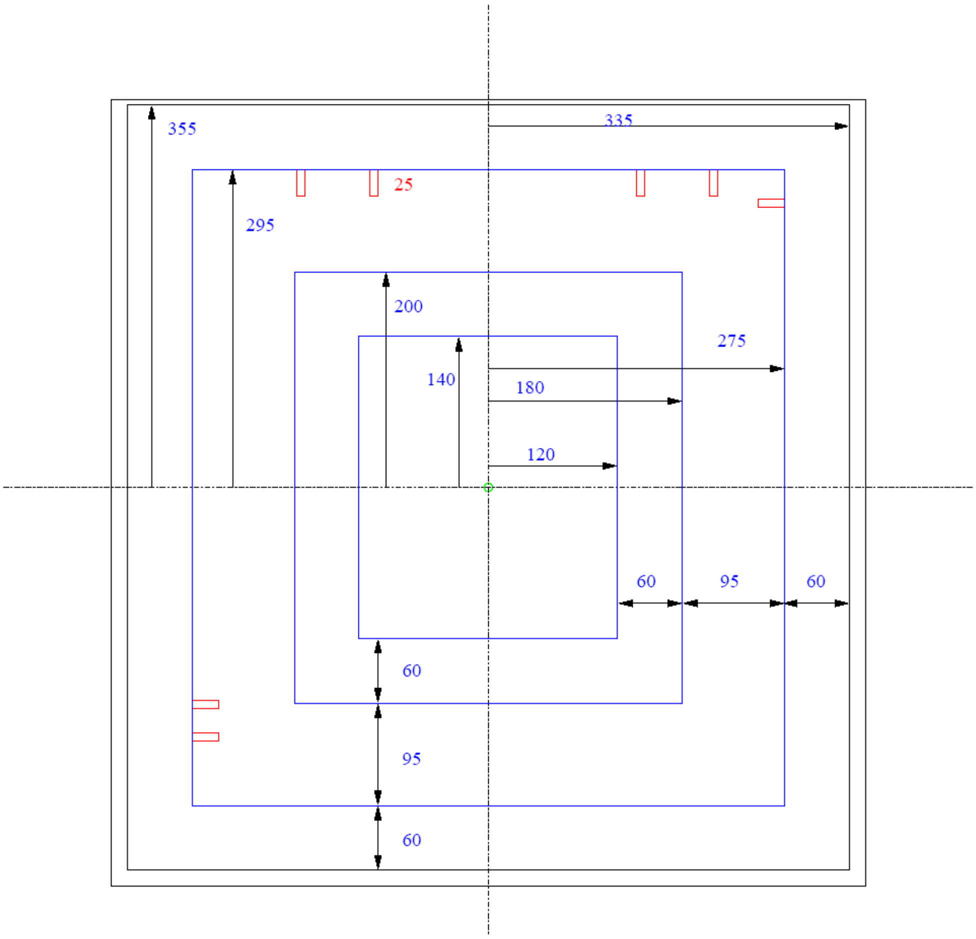

Figure 5.3: The dimensions of the Double Chooz far detector. All sizes are given in cm. From inside to outside there is: 12.7 m^3 Gadolinium loaded liquid scintillator target, 28.1 m^3 unloaded liquid scintillator (γ-Catcher), 100 m^3 non scintillating buffer, a photomultiplier support structure and a 110 m^3 veto. The near detector will have a slightly larger muon veto for improved cosmic ray background reduction (the shielding depth of the near detector will be less than for the far detector).

5.4 Background in Double Chooz

As it was described in Chapter 5.2.2, the $\bar{\nu}_e$-events can be tagged in Double Chooz: the signature is a prompt signal between $\approx$ 1 MeV and $\approx$ 8 - 10 MeV from the positron and a delayed signal from the neutron capture on Gadolinium with about 8 MeV. An event can falsely be identified as $\bar{\nu}_e$-event if a neutron type event falls into the time window (a few 100 μs) after an event with an energy deposition in the energy range between $\approx$ 1 MeV and $\approx$ 8 - 10 MeV (positron type event). This can either happen by accident ("accidental background") or through mechanisms which provide a correlation between the two events ("correlated background"). There are two sources of correlated background, one being cosmogenically produced isotopes with a certain decay scheme (beta-neutron cascades) and the second being fast neutrons penetrating the detector from the outside and creating the positron type signal by scattering in the scintillator before they are captured on the Gadolinium. Both types of background will be discussed in the following.

5.4.1 Accidental Background

If an event in the target deposits between 1 MeV and 8 MeV in the scintillator and this event is accidentally followed within a few 100 μs by an 8 MeV event, these two will be falsely identifed as a $\bar{\nu}_e$-event. Sources for these events are radioactive isotopes either in the scintillator or the acrylic vessels ("internal background") or outside the active regigion ("external background").

The most important feature though of the accidental background is that its rate can be measured and then subtracted from the results. If positron type events occur at a rate r_{e^+}, neutron type events occur at a rate r_n and a coincidence is created when the latter occurs within a time window τ after the positron type event, the rate of accidental coincidences can be written as:

$$r_{acc} = r_{e^+} \cdot r_n \cdot \tau \qquad (5.12)$$

The accidental coincidence rate can also be measured by shifting the time window of acceptance to a much later time after the positron type event (yet leaving the width of the window the same). This way correlated events can not be detected, and only accidental correlations remain.

5.4.1.1 Internal Background

Contributors to the internal background are radioactive decays with gamma emission and also beta decays. Alpha decays are not dangerous because the alpha energy of typically several MeV is quenched down to below 1 MeV in the scintillator. The uranium and thorium decay chains both have a short Bismuth - Polonium coincidence which allows event event by event rejection. Therefore only three isotopes remain as potential background sources from the uranium and thorium decay chains: ^{234}Pa (beta decay with Q = 2.2 MeV), ^{228}Ac (beta decay with Q = 2.13 MeV) and ^{208}Tl (beta decay with Q = 4.99 MeV). Another potential source of internal background is ^{40}K (beta decay with q = 1.31 MeV or electron capture with consecutive 1.461 MeV gamma emission). The design goal is to keep the total internal beta/gamma rate of these isotopes below 1 count/sec. The concentration limits for radioactive contaminations in the scintillator and the acrylic vessels necessary to achieve this rate are shown in Table 5.1 on Page 119. In the Borexino CTF concentrations of $c_{U,Th} < 10^{-15} g/g$ and $c_{^{40}K} < 10^{-12} g/g$ have been measured for two liquid scintillators, one Pseudocumene based and the other PXE based. The SNO collaboration has reported concentrations of $c_{U,Th} < 3 \cdot 10^{-12} g/g$ for acrylic [SNO 02]. Gamma spectroscopy measurements of acrylic have shown a potassium concentration of $c_{^{40}K} < 10^{-9} g/g$. These concentrations are well below the allowed concentrations listed in Table 5.1 on Page 119, therefore the design goal of $b_{int} < 1$ count/sec intrinsic gamma/beta background should be safely reached.

Another source of internal background are neutrons created by spontaneous fission of heavy elements and by (α, n)-reactions. The neutron rate n_{int} via these processes can be calculated from the uranium and thorium concentration $c_{U,Th}$ in the scintillator as follows:

$$n_{int} \approx 0.4 \frac{1}{s} \cdot \frac{c_{U,Th}}{10^{-6}} \tag{5.13}$$

With the values given in Table 5.1 on Page 119 it can be seen that this contribution to the internal accidental background is negligible.

Contamination	Allowed concentration (g/g)
U and Th in the scintillator	$\sim 10^{-12}$
U and Th in the acrylic vessel	$\sim 10^{-10}$
^{40}K in the scintillator	$\sim 10^{-10}$
^{40}K in the acrylic vessel	$\sim 10^{-8}$

Table 5.1: Approximate upper limits for the concentrations of U, Th, and ^{40}K in the scintillator and the acrylic vessel to achieve a single gamma/beta background rate of below 1 count/sec in Double Chooz. Secular equilibrium in the decay chains is assumed.

5.4.1.2 External Background

For the external radiactive background only gamma emission is important as only high energy gamma rays can penetrate the detector and reach the active region, not alphas and betas though. The dominant background contribution is expected from the photomultipliers and their support structure (glass typically has high concentrations of Uranium and especially Potassium). Due to the massive shielding, only the highest energy gamma rays have to be considered, i.e. the 2.6 MeV gamma line from the decay of ^{208}Tl. Scaling the background contribution of the photomultipliers in the Borexino CTF to the Double Chooz detector geometry yields a background rate of $b_{ext} \approx \frac{counts}{s} \cdot \frac{N_{Pmt}}{500}$. The total number of photomultipliers N_{Pmt} has not been determined yet.

Another source of external background are neutrons produced by cosmic ray muons inside the detector, either by spallation processes or by stopped negative muons that are captured on nuclei. The number of neutrons created by spallation scales with the muon flux and with $E^{0.75}$ where E is the mean muon energy, which itself depends on the shielding depth. Measured values for the muon flux and the mean muon energy by different experiments in the Gran Sasso underground laboratory (LVD [DEM 99], MACRO [AMB 98], CTF [ALI 98-2]) have been extrapolated to different shielding depths, yielding the spallation neutron production rates shown in Table 5.2 on Page 120.

Stopped negative muons can be captured on nuclei and then cause neutron emission. The neutron production rates for this process have been estimated

Shielding depth $[m.w.e.]$	Muon rate $[1/s]$	Mean muon energy $[GeV]$	Neutrons $[1/s]$
40	$1.1 \cdot 10^3$	14	2
60	$5.7 \cdot 10^2$	19	1.4
80	$3.5 \cdot 10^2$	23	1
100	$2.4 \cdot 10^2$	26	0.7
300	$2.4 \cdot 10^1$	63	0.15

Table 5.2: Neutron production rates in the active region of the Double Chooz detector due to spallation processes caused by cosmic ray muons traversing the detector.

[ARD 04] and are summed up in Table 5.3 on Page 120.

Shielding depth $[m.w.e.]$	Muon stopping rate $[1/s]$	Neutrons $[1/s]$
40	$5 \cdot 10^{-1}$	0.7
60	$3 \cdot 10^{-1}$	0.4
80	$1.2 \cdot 10^{-1}$	0.2
100	$6 \cdot 10^{-2}$	0.08
300	$2.5 \cdot 10^{-3}$	0.003

Table 5.3: Neutron production rates in the active region of the Double Chooz detector due to capture of stopped negative cosmic ray muons.

The neutron production rate due to spallation processes exceeds the rate due to capture of stopped negative muons. Both contributions do not endanger the experiment as they coincide with the muon passing through the detector and therefore can be vetoed. Only for a very small fraction where the neutron capture takes place after the veto time window they would appear as background, yet their accidental nature allows measurement of the rate and subtraction from the signal, as explained in the introduction to this chapter.

5.4.2 Correlated Background

The correlated background can not be measured directly and then subtracted like the accidental background. Therefore correlated background is potentially much more dangerous. Two sources for correlated background have been identified: cosmogenically produced isotopes which emit a neutron after a beta decay (beta-neutron cascades) and fast external neutrons created by cosmic ray muons outside the detector.

5.4.2.1 Beta-Neutron Cascades

Muon spallation on ^{12}C creates a variety of radioactive isotopes which are shown in Table 5.4 on Page 122 with their respective production rates. Three of these isotopes, ^{8}He, ^{9}Li and ^{11}Li undergo beta decay with Q-values of 8.6 MeV, 11.9 MeV and 20.1 MeV, respectively, and a neutron emission. The decay schemes for ^{9}Li and ^{8}He are shown in Figure 5.4 on Page 123 and Figure 5.5 on Page 124, respectively. The beta decay of the mother isotope followed by a neutron mimics the signature of a real $\bar{\nu}_e$-event. In this case vetoing through the muon signal is not feasible as the lifetimes of the mother isotopes range between 0.1 s and 1 s, which would result in too much dead time for the detector.

The cross section for the production of ^{8}He and ^{9}Li has been measured [HAG 00] with muon energies of 190 GeV at the SPS at CERN. Only the sum of the production (^{8}He + ^{9}Li) has been measured though. The production rate in Double Chooz has been estimated by scaling this value with the muon flux and the $E^{0.75}$-law for the mean muon energy. It is 31 ± 12 per day for the near detector (at only 60 m.w.e. shielding depth) and 3.3 ± 1.3 per day for the far detector (at 300 m.w.e.), see Table 5.4 on Page 122. There is a cascade in the decay of ^{8}He ($^{8}He \rightarrow {}^{8}Li \rightarrow {}^{8}Be$, see Figure 5.5 on Page 124), which can allow the measurement of the ^{8}He production rate in situ. The ^{9}Li production rate can then be determined by subtracting the ^{8}He production rate from the expected value for the sum of both. The production cross section for ^{11}Li has not been measured yet.

Isotope	Production rate near detector at 60 m.w.e. [$1/day$]	Production rate far detector at 300 m.w.e [$1/day$]
^{12}Be	not measured	not measured
^{11}Be	< 18	< 2.0
^{11}Li	not measured	not measured
^{9}Li	17 ± 3	1.7 ± 0.3
^{8}Li + ^{8}He	31 ± 12	3.3 ± 1.2
^{6}He	126 ± 12	13.2 ± 1.3
^{11}C	$(7.1 \pm 0.5) \cdot 10^3$	$(7.5 \pm 0.5) \cdot 10^2$
^{10}C	$(9.0 \pm 1.1) \cdot 10^2$	$(9.5 \pm 1.2) \cdot 10^1$
^{9}C	$(3.8 \pm 1.2) \cdot 10^1$	4.0 ± 1.2
^{8}B	$(6.0 \pm 1.1) \cdot 10^1$	5.9 ± 1.2
^{7}Be	$(1.8 \pm 0.2) \cdot 10^3$	$(1.9 \pm 0.2) \cdot 10^2$

Table 5.4: Radioactive isotopes produced by cosmic ray muons and their secondary shower particles in the liquid scintillator target of the Double Chooz near and far detectors. The production rates are calculated for 12.7 m^3 liquid scintillator as used in Double Chooz. They are conservative estimates from measured values scaled with E$^{0.75}$ (E: mean muon energy) [ARD 04]. Only the sum of the ^{9}Li and ^{8}He rate has been measured [HAG 00].

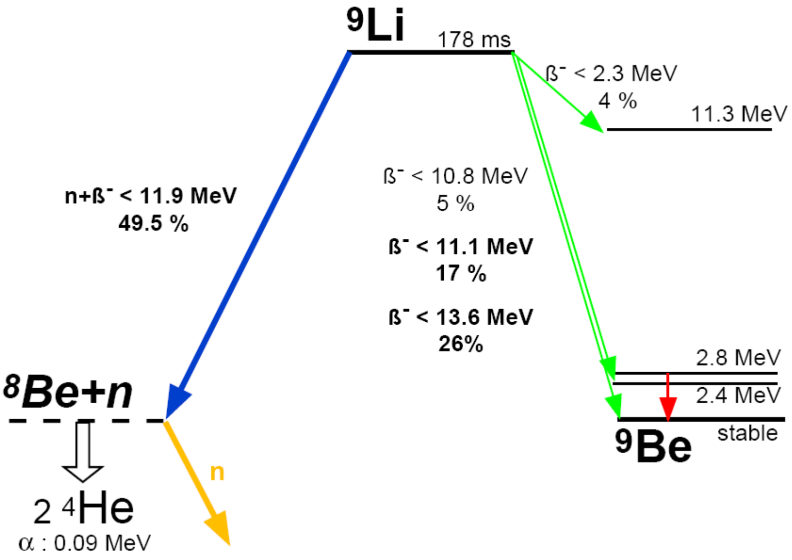

Figure 5.4: Decay scheme for ^{9}Li. The Q-values of the β-decays are quoted, as well as half-life times and braching ratios. The emitted neutrons typically have an energy of ∼1 MeV. After the decay to ^{8}Be, the ^{8}Be immediately breaks up into two low energy α-particles.

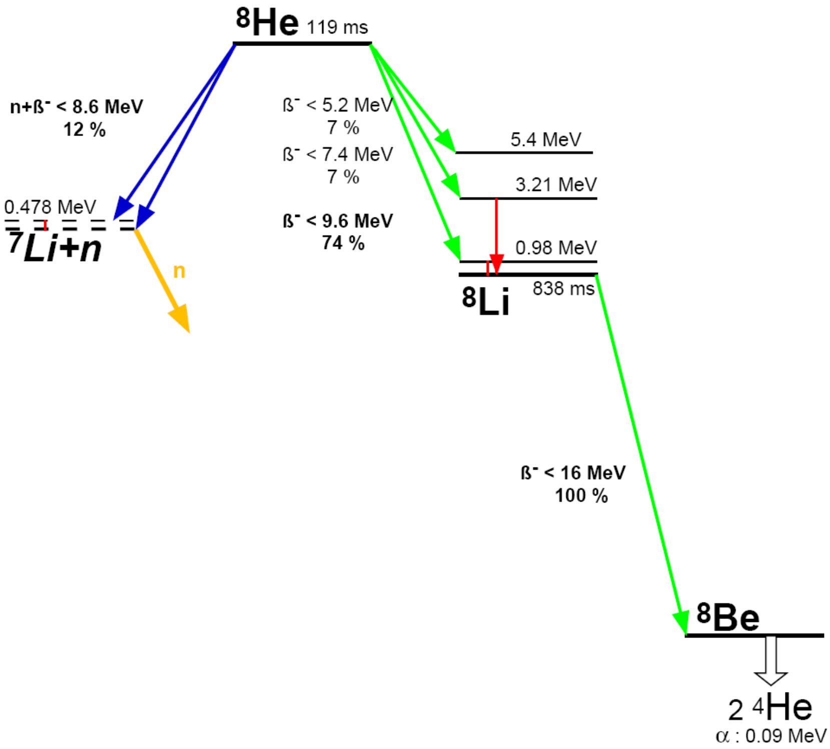

Figure 5.5: Decay scheme for ^{8}He. The Q-values of the β-decays are quoted, as well as half-life times and branching ratios. The emitted neutrons typically have an energy of ∼1 MeV.The decay cscade $^8He \rightarrow {}^8Li \rightarrow {}^8Be$ (green arrows) might offer a way to measure the ^{8}He production rate in situ.

5.4.2.2 Fast External Neutrons

Another source of correlated background are fast external neutrons produced by cosmic ray muons. Created in the surrounding rock, these neutrons can enter the detector and be slowed down by multiple scattering in the scintillator. The recoil protons give rise to a prompt signal which can be in the energy range of the positron type signal. After having slowed down, the neutron can then be captured on Gadolinium, and therefore create the coincidence signal which leads to a false identification as a $\bar{\nu}_e$-event. Although, in most cases, the muon which produced the neutron will also cross the detector and therefore allow tagging by the muon veto, this is not necessarily always the case. A muon can cross the rock several meters away from the detector and still create a neutron that has a high enough energy to penetrate the detector. In principle, the signal created by the recoil protons could be distinguished from the β-signal via pulse shape discrimination, but this would also introduce a new source of systematic error into the experiment. Therefore, pulse shape discrimination will not be used in Double Chooz.

In order to estimate the background introduced by these fast external neutrons, a Monte Carlo simulation has been developed based on the GEANT4 [AGO 03] simulation toolkit. The detector has been modeled in the simulation as it is shown in Figure 5.3 on Page 116, with an overburden of 100 m.w.e. rock. The simulation starts tracking cosmic ray muons through the rock from a distance of 20 m above the detector. All secondary particles created by the muon with energies greater than 1 MeV are followed and the interaction of the muon and its secondary particles with the detector is calculated. The muon tracking is started inside the rock and not at the earth's surface to save computing time, a distance of 20 m from the detector ensures there is enough rock (which serves as the target for muons) for a full shower of secondary particles to develop.

The energy spectrum, the angular distribution the total flux and the charge ratio of the muons from where their tracking is started (where they are "created" in the simulation) is calculated as a function of the shielding depth h [HEI 98]:

$$I_V\left(h\right) = \frac{258.5}{\left(h+210\right)\left(\left(h+10\right)^{1.66}+75\right)} \cdot e^{-5.5 \cdot 10^{-4} h} \qquad \frac{1}{cm^2 s} \tag{5.14}$$

I_V: Vertical muon intensity in $\frac{1}{cm^2 s}$
h : Shielding depth in m.w.e.

This assumes a flat topology of the surface. The equation is in valid for h < 2000 m.w.e.. The muon intensity as a function of the zenith angle θ can be calculated from the vertical muon intensity I_V:

$$I\left(h,\theta\right) = I_V\left(h\right)\cos^{n(h)}\theta \tag{5.15}$$

n(h): Parameter accounting for the dependence of the angular distribution of the muon flux on h

The parameter n(h), which accounts for the dependence of the angular distribution of the muon flux on the shielding depth can be approximated as follows:

$$n\left(h\right) = 2.09 + 8.34\cdot 10^{-4}h + 8.06\cdot 10^{-9}h^2 - 7.45\cdot 10^{-2}\ln\left(h+1.1\right) \tag{5.16}$$

h : Shielding depth in m.w.e.

The total muon intensity follows from integration of Equation (5.15):

$$I_{tot}\left(h\right) = \frac{2\pi}{n\left(h\right)+1}\cdot I_V\left(h\right) \tag{5.17}$$

The differential energy spectrum $\frac{dN_\mu^v}{dE_\mu}\left(E_\mu,h\right)$ of the muons assumed in the simulation has the following form [HEI 98]:

$$\frac{dN_\mu^v}{dE_\mu}\left(E_\nu,h\right) = C\cdot e^{-\gamma bh}\left(E_\mu + \frac{a}{b'}\left[1-e^{-b'h}\right]\right)^{-(\gamma+1)} \tag{5.18}$$

$\frac{dN_\mu^v}{dE_\mu}(E_\mu, h)$: Differential energy spectrum for vertical muons
h : Shielding depth in m.w.e.
C : Normalization constant
b : Effective energy loss coefficient, $b = 3.81 \cdot 10^{-6} cm^2/g$
b' : Effective energy loss coefficient, $b' = 3.74 \cdot 10^{-6} cm^2/g$
γ : Exponent $\gamma = 2.70$
a: Constant with $\frac{a}{b'} = 647$ GeV

The relative amount of positive muons in the total muon flux n^+ with

$$n^+ = \frac{N_{\mu^+}}{(N_{\mu^+} + N_{\mu^-})} \tag{5.19}$$

depends on the muon energy, a detailed description can be found in [HEI 98]. For the simulation, a value of $n^+ = 0.43$ was used which is a good approximation for the shielding depths relevant for Double Chooz.

The detector response was evaluated in the simulation by calculating the *visible* energy deposition of charged particles in the scintillator. This accounts for quenching, i.e. a reduced light yield per MeV for heavier charged particles compared to electrons. The quenching in scintillators has been well studied for various experiments (e.g. Borexino [ALI 02]). The visible energy deposition can be expressed as:

$$E_{vis} = q \cdot E \tag{5.20}$$

E_{vis}: Visible energy deposition in the scintillator
q: Quenching factor
E: Energy of the charged particle

The quenching factor q depends on the type of particle. In this simulation six types of charged particles were taken into account for interaction with the scintillator: e$^-$, e$^+$, μ^-, μ^+, protons and ^{12}C-nuclei, as they are the lightest particles occurring in this case and therefore the ones with the least quenching. Recoil ^{16}O-nuclei from the organic solvent the scintillator is based on (PXE)have been studied and can be safely neglected. The quenching factors used are ([MAI 70], [CEC 79]):

$$q_{e^-} = q_{e^+} = 1$$
$$q_{\mu^-} = q_{\mu^+} \approx 1$$
$$q_{^{12}C} = 0.007$$

The quenching factor for the electron is defined as 1. The light yield of a β-event in the scintillator defines the energy calibration of the detector.

In the case of the proton the quenching factor is energy dependent, here Equation (5.20) is replaced by:

$$E_{vis}\left(E_p\right) = \begin{cases} 0.138 \cdot E_p^{1.5} & \text{if } E_p < 5.25 \text{ MeV} \\ (0.63 \cdot E_p) - 1.1 & \text{if } E_p > 5.25 \text{ MeV} \end{cases} \tag{5.21}$$

E_p: Proton energy in MeV

After the software was completed, some initial simple tests showed credible results. The number of neutrons produced by muons is in very good agreement with known values. The $E_\mu^{0.75}$ dependence of the number of neutrons N_n created [ZAT 65], could also be reproduced. Nonetheless, a more detailed test of the software has been undertaken. The background caused by fast external neutrons in the *original* Chooz detector [CHO 99], [CHO 03] has been simulated and compared with the measured result. The main difference between the original Chooz detector and the Double Chooz design is the sand shielding and the lack of a gamma catcher in the original Chooz detector, see Figure 5.6 on Page 129.

The simulation was run to reproduce 31.0 hours of detector time. The Monte Carlo data of the detector response was then analyzed to find correlated background events, where a neutron had entered the target and deposited between 1 MeV and 8 MeV visible energy in the scintillator and then was captured inside the target. The muon veto response was also taken into account, and if an event deposited more than 4 MeV visible energy in the muon veto it was discarded. One correlated background event was found, yielding 0.8 events/day for the most likely event rate. Using Poisson statistics, a background rate > 1.6 events/day can be excluded at 90% confidence level. The measured background rate from fast external neutrons in Chooz was $(1.01 \pm 0.04(stat) \pm 0.01(sys))$ events/day, in very good agreement with the Monte Carlo result.

After these tests proved the reliability of the simulation software, the

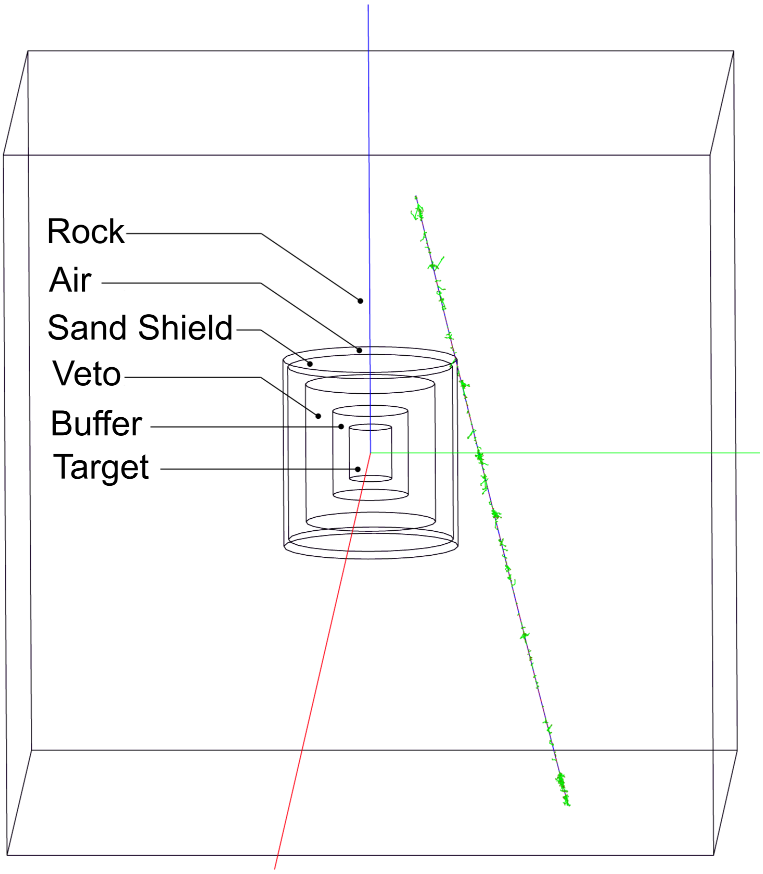

Figure 5.6: Geometry of the original Chooz detector taken from the simulation program. A muon track and its secondary particle tracks can be seen. The geometry is very similar to the Double Chooz design, differences are the sand shielding and the lack of the gamma catcher, and also the target volume is only 5.6 m^3 whereas for Double Chooz 12.7 m^3 are planned. The shielding depth for this detector was 300 m.w.e. For comparison with the Double Chooz detector see Figure 5.3 on Page 116, Figure 5.2 on Page 114 and Figure 5.7 on Page 131.

background in Double Chooz was calculated. Due to the large number of secondary particles the muons produce while crossing through the rock the simulation was very demanding in terms of computing power. In the final run of approximately 1.5 months (using two computers in parallel) a total detector time of 42.92 hours was simulated, see also Table 5.5 on Page 130. A picture of a muon track extracted from the simulation can be seen in Figure 5.7 on Page 131.

Computer time:	1985 hours
Simulated time:	42.92 hours
Muons tracked:	337,729,956
Neutrons tracked:	580,335
Neutrons thermalized in the target:	20642
Of these undetected by muon veto:	21
Backround events:	1

Table 5.5: The amount of data processed in the GEANT4 simulation of the external neutron background in Double Chooz.

Due to the large amount of computing time needed, only one simulation was performed for a shielding depth of 100 m.w.e., which is in between the shielding depths for the near (m.w.e.) and the far Double Chooz detector (m.w.e.). The results can be scaled to different shielding depths using the $E_\mu^{0.75}$-relation [ZAT 65] mentioned earlier. The energy spectrum of the primary muons, as they were created in the simulation, can be seen in Figure 5.8 on Page 132.

Of all the events created in the simulation, only those were selected where at least one neutron thermalized inside the target region (these are possible background events due to the neutron capture on Gadolinium following the thermalization). Figure5.9 on Page 132 and Figure 5.10 on Page 133 show the visible energy deposition in the target and gamma catcher region of these events.

Of a total 6797 events where at least one neutron thermalized inside the target, 17 events are in the energy window for the positron-type event

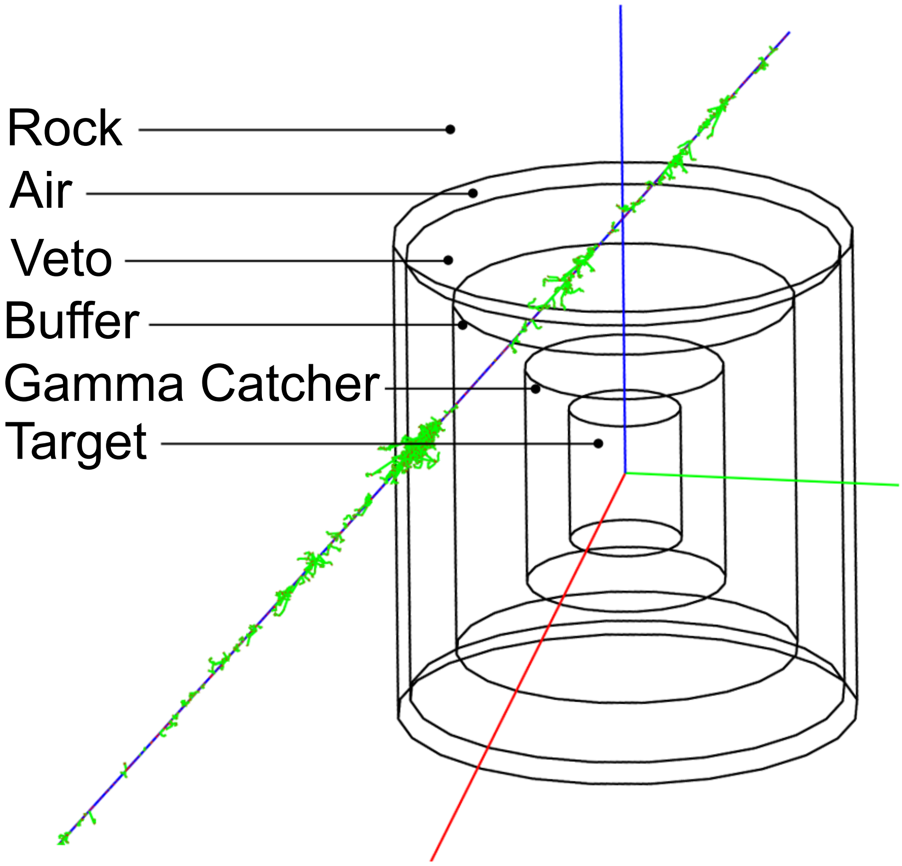

Figure 5.7: Geometry of the Double Chooz detector as it is used in the simulation program. A muon track and its secondary particle tracks can be seen.

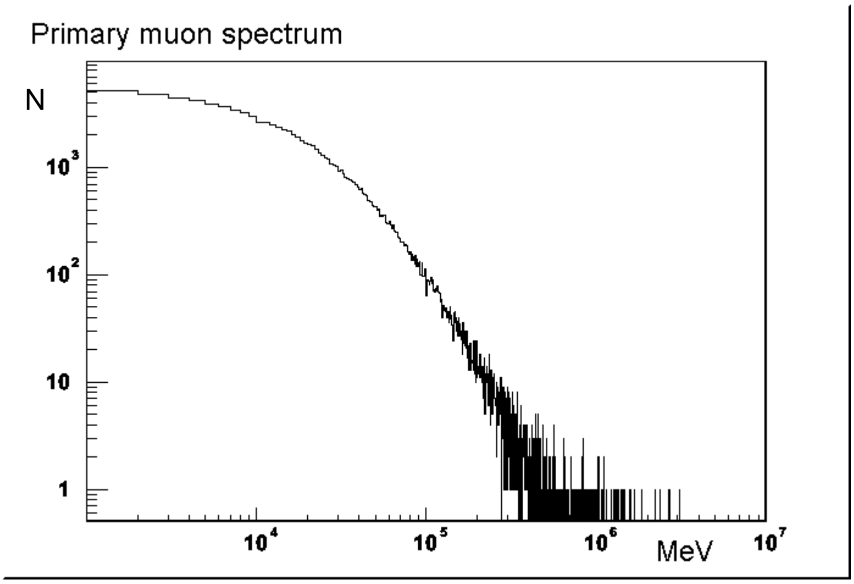

Figure 5.8: Energy spectrum of the muons as they were created in the simulation for the Double Chooz detector.

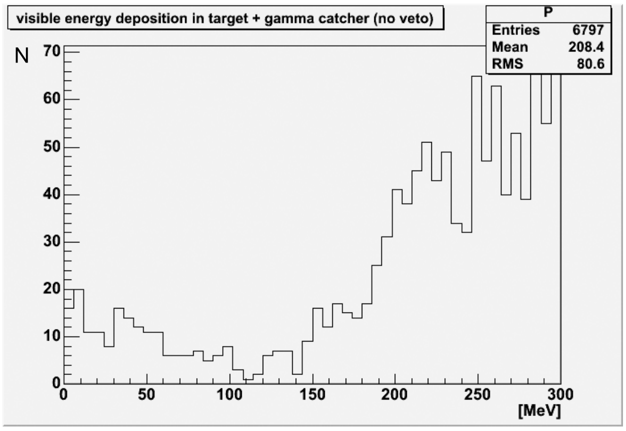

Figure 5.9: Visible energy deposition in the target and gamma catcher region of the Double Chooz detector by events in which at least one externally created neutron thermalized inside the target region. A muon veto cut has not been made. See Figure 5.10 on Page 133 for an enlarged view of the lower energy region.

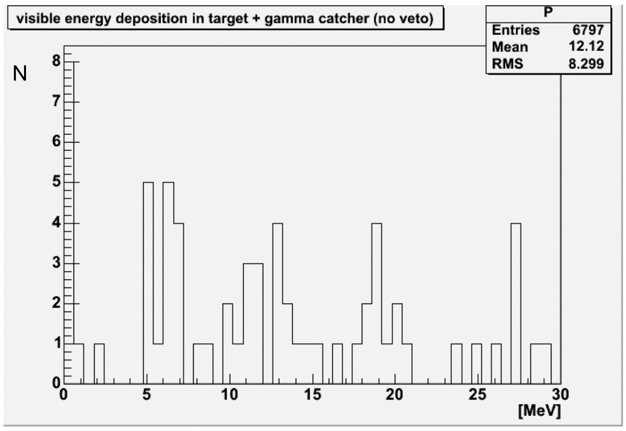

Figure 5.10: Visible energy deposition in the target and gamma catcher region of the Double Chooz detector by events in which at least one externally created neutron thermalized inside the target region. This graph shows only energies up to 30 MeV, as the energy window for background events is between 1 MeV and 8 MeV. A muon veto cut has not been made.

between 1 MeV and 8 MeV. Of course, there is also the muon veto, which has not yet been taken into account. If one discards all events which produce a visible energy deposition in the muon veto of > 4 MeV, only one event remains in the energy window between 1 MeV and 8 MeV. The spectra for the visible energy deposition of all events where at least one neutron thermalized inside the target *and* the visible energy deposition in the muon veto was < 4 MeV can be seen in Figure 5.11 on Page 134 and Figure 5.12 on Page 134.

The result of the simulation, i.e. 1 event in 42.92 hours at 100 m.w.e., now has to be scaled to the shielding depths of the near and far Double Chooz detectors, 60 m.w.e. and 300 m.w.e., respectively. The scaling is done using the $E_\mu^{0.75}$ relation for the neutron production rate [ZAT 65], the mean muon energy and the muon flux. On one hand, the muon flux decreases with larger shielding depths (and accordingly the neutron production rate decreases), yet the mean energy of the muons increases which means and increase in the neutron production rate. The following relation was used for the scaling of the neutron production rate:

$$N_n \propto \Phi_\mu \cdot E_\mu^{0.75} \tag{5.22}$$

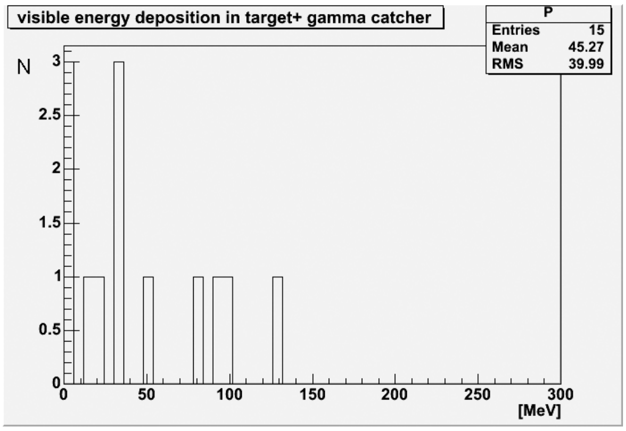

Figure 5.11: Visible energy deposition in the target and gamma catcher region of the Double Chooz detector by events in which at least one externally created neutron thermalized inside the target region. Events with a visible energy depositon > 4 MeV in the muon veto have been excluded. See Figure 5.12 on Page 134 for an enlarged view of the lower energy region.

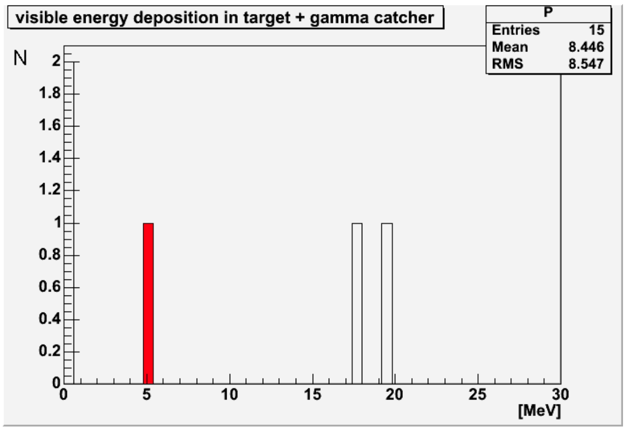

Figure 5.12: Visible energy deposition in the target and gamma catcher region of the Double Chooz detector by events in which at least one externally created neutron thermalized inside the target region. This graph shows only energies up to 30 MeV, as the energy window for background events is between 1 MeV and 8 MeV. Events with a visible energy deposition > 4 MeV in the muon veto have been excluded. The one remaining background event is highlighted in red.

N_n: Neutron production rate
Φ_μ: Muon flux
E_μ: Mean muon energy

The values for the mean muon energy E_μ and the Muon flux Φ_{mu} at different shielding depths are summarized in Table 5.6 on Page 135. With the scaling factors for each shielding depth one can estimate the neutron background at 60 m.w.e. and 300 m.w.e. from the Monte Carlo result for 100 m.w.e., assuming the background induced by external neutrons is proportional to the neutron production rate. Values for 40 m.w.e. and 80 m.w.e. have been included as the overburden for the near detector will still be built and variations might be considered.

Depth $[m.w.e]$	E_μ $[GeV]$	Φ_{mu} $[1/m^2s]$	est. Background $rate[1/day]$	Limit on background rate at 90% C.L. $[1/day]$
40	14	30.3	1.5	< 3.0
60	19	16.7	1.1	< 2.2
80	23	10.4	0.8	< 1.6
100	26	6.9	0.6	< 1.2
300	63	0.67	0.1	< 0.2

Table 5.6: Correlated Background induced by fast external neutrons. Muon fluxes and mean muon energies for different depths are also shown. With these and using Equation (5.22), the fast external neutron background rate of 0.6 / day which has been calculated in the Monte Carlo simulation for a depth of 100 m.w.e., can be extrapolated to the other depths listed. The resulting values are reported in the right column. The far Double Chooz detector will be at a depth of 300 m.w.e., for the near detector a shielding of 60 m.w.e. is intended.

As there was only one background event produced in the simulation, the background rates of 0.1 per day for the far detector and 1.1 per day for the near detector can only be seen as the most likely values due to the low statistical significance. Analysis using Poisson statistics yields upper limits at 90% C.L. for the background rate in the far detector of 0.2 per day and in the near detector of 2.2 per day. The results for other shielding depths are also shown in Table 5.6 on Page 135.

After estimating the background rates due to fast external neutrons in Double Chooz, the possibility of improving these by an extended muon veto was investigated. A ring of scintillator panels around the top of the Double Chooz tank (see Figure 5.13 on Page 137) could increase the efficiency of muon detection. For this purpose, for every event in which at least one neutron thermalized in the target region, the intersection point of the corresponding muon track with this additional muon veto was calculated. The distance r of this intersection point from the center of the detector's top then indicates the size of the additional veto panel necessary to detect this muon. Figure 5.14 on Page 138 shows the distribution of r for these events. Of course, in those events with r $<$ 335 cm the muon has to intersect the detector tank and will be detected by the muon veto inside the tank (Figure 5.2 on Page 114 shows this muon veto system).

Therefore, in Figure 5.15 on Page 139 the r distribution is shown again, this time after a cut using the main muon veto has been applied (evnets with a visible energy deposition $>$ 4 MeV in the muon veto have been discarded). The remaining events shown in Figure 5.15 on Page 139 are possible correlated background events, but no cut on the visible energy deposition in the gamma catcher + target region has been applied. For the one real background event the distance r of where the muon track intersects the the additional muon veto panels to the center is 435 cm. This means that from where the detector tank ends (at r = 335 cm) an additional 100 cm of scintillator panels would have been enough to identify the one correlated background event found in the Monte Carlo Simulation. Using Poisson statistics and the extrapolation to different shielding depths explained above, this results in an upper limit for the fast external neutron background of 1.1 counts/day at 90% C.L. for the near detector and 0.1 counts/day at 90% C.L. for the far detector.

5.4.3 Conclusion

One type of background sources identified for Double Chooz are internal beta/gamma decays, external gammas and neutrons created inside the detector either by cosmic ray muons or by radioactive decays. All of these

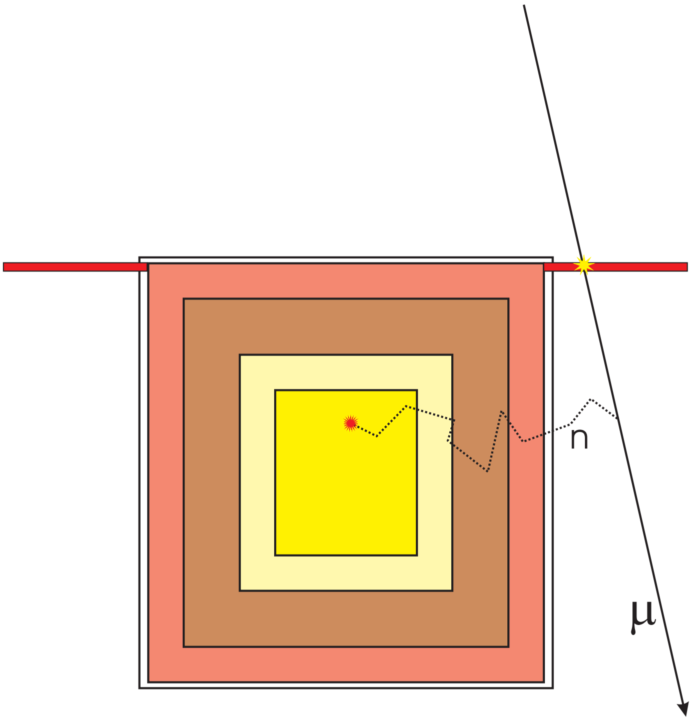

Figure 5.13: An additional muon veto for the Double Chooz detector could reduce the correlated background rate caused by fast external neutrons. A ring of scintillator panels around the top of the detector (shown red in the illustration) increases the muon detection efficiency.

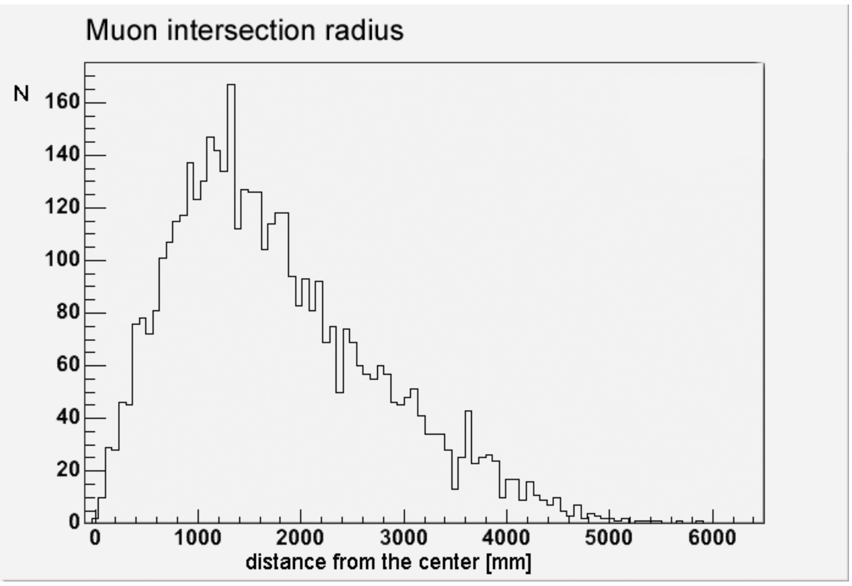

Figure 5.14: Distance r from where the muon track intersects the additional scintillator panel (see Figure 5.13 on Page 137) on the top of the Double Chooz detector to the center of the top. Selected were all events in which at least one neutron thermalized inside the target region. No energy cut or muon veto cut has been applied. See Figure 5.15 on Page 139 for the same distribution after a muon veto cut.

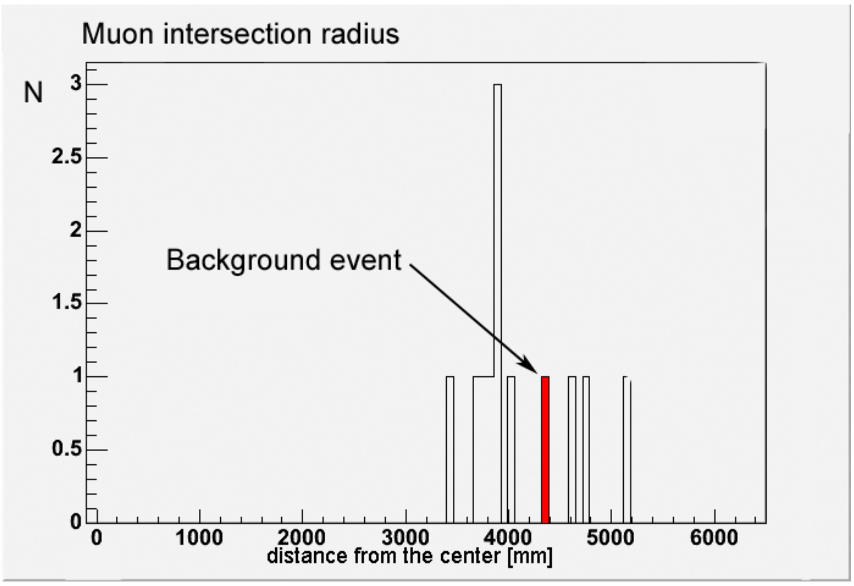

Figure 5.15: Distance r from where the muon track intersects the additional scintillator panel (see Figure 5.13 on Page 137) on the top of the Double Chooz detector to the center of the top. Selected were all events in which at least one neutron thermalized inside the target region. Events with a visible energy deposition > 4 MeV in the main muon veto have been discarded. No cut on the energy deposition in the gamma catcher + target region has been applied. The one event with an energy deposition between 1 MeV and 8 MeV (this is the one background event) is highlighted in red. Its corresponding muon track intersected the veto panels at r = 435 cm, i.e. 100 cm of additional muon veto panels would have been enough to be able to tag this event as an external neutron background event (see text for more explanation.)

backgrounds are accidental in nature, i.e. they do not inherently produce the coincidence signal used to tag the $\bar{\nu}_e$-events. Therefore the rates of these backgrounds can be measured and subtracted from the signal.

More dangerous though are two other types of background: beta-neutron cascades and neutrons produced outside the detector by cosmic ray muons can mimic the coincidence signal of $\bar{\nu}_e$-events, the former by emitting a neutron after a beta decay and the latter by creating a beta-like signal through multiple scattering when entering the detector. These two sources of background are therefore called correlated background. Of the isotopes resposible for beta-neutron cascades, ^{8}He, ^{9}Li and ^{11}Li, the production rate of ^{8}He might be measured in situ. The production rates of ^{9}Li and ^{11}Li will have to be determined, the current (very conservative) estimate for the sum of both is 31/day for the near detector and 3.3/day for the far detector.

The background induced by fast external neutrons has been estimated with a Monte Carlo simulation, and upper limits of 0.2 counts/day at 90% C.L for the far detector and 2.2 counts/day at 90% C.L. for the near detector have been determined. With an additional muon veto using comparatively inexpensive scintillator panels (100 cm wide) around the top the detectors these limits can be reduced to 0.1 counts/day at 90% C.L and 1.1 counts/day at 90% C.L, respectively.

5.5 Comparison with other Future Experiments

There are other experiments which will be able to improve our knowledge on θ_{13}: In the nearer future, there are the accelerator beam experiments OPERA [DUC 02], MINOS [ABL 95] and ICARUS [APR 02], which are currently under construction. These experiments are placed in the center of accelerator-produced neutrino beams which will be almost pure ν_μ with a small contamination of $\approx 1\%$ ν_e. Their main purpose is to improve the precision on the measurement of the "atmospheric" oscillation parameters by observing the $\nu_\mu \rightarrow \nu_\mu$ disappearance. The Gran Sasso experiments OPERA and ICARUS will be also able to measure the ν_τ-appearance in the $\nu_\mu \rightarrow \nu_\tau$ channel, as the mean energy of the CNGS ν_μ-beam from CERN to Gran

Sasso is 17 GeV, well above the production threshold of the τ. But, in addition, the appearance of $\nu_\mu \rightarrow \nu_e$ will provide information about $\sin^2 2\theta_{13}$, see Equation (5.23).

In the more distant future new accelerator "superbeam" experiments are planned, namely J-PARC to Super Kamiokande [ITO 01] and NuMI [AYR 01], for which letters of intent have been published. The primary goal of these experiments is the measurement of $\sin^2 2\theta_{13}$ via the appearance $\nu_\mu \rightarrow \nu_e$, and their design has been optimized for this purpose.

The conversion probability $P_{\nu_\mu \rightarrow \nu_e}$ with terms up to the second order, i.e. proportional to $\sin^2 2\theta_{13}$, $\sin 2\theta_{13} \cdot \alpha$ and α^2 is [HUB 04]:

$$\begin{aligned} P_{\nu_\mu \rightarrow \nu_e} \approx & \sin^2 2\theta_{13} \sin^2 \theta_{23} \sin^2 \Delta \\ & \mp \alpha \sin 2\theta_{13} \sin \delta_{CP} \sin 2\theta_{12} \sin 2\theta_{23} \Delta \sin^2 \Delta \\ & + \alpha \sin 2\theta_{13} \cos \delta_{CP} \sin 2\theta_{12} \sin 2\theta_{23} \Delta \cos \Delta \sin \Delta \\ & + \alpha^2 \cos^2 \theta_{23} \sin^2 2\theta_{12} \Delta^2 \end{aligned} \tag{5.23}$$

with:

α:	Mass hierarchy parameter, $\alpha = \Delta m^2_{21} / \Delta m^2_{23}$
Δm^2_{ij}:	$\Delta m^2_{ij} = \left(m_i^2 - m_j^2 \right)$
Δ:	$\Delta = \Delta m^2_{31} L / \left(4 E_\nu \right)$
L:	Distance from the point of creation
E_ν:	Energy of the neutrino
"$\mp$":	The sign of the the second term is "-" for neutrinos and "+" for antineutrinos
δ_{CP}:	CP-phase, see Equation(1.10) on Page 8

As it can be seen from Equation (5.23), measuring $\sin^2 2\theta_{13}$ is not as straightforward as it is with the Double Chooz reactor neutrino experiment, where $\sin^2 2\theta_{13}$ can be measured without the influence of θ_{23} or the CP-phase:

$$P_{\bar{\nu}_e \rightarrow \bar{\nu}_e} \approx 1 - \sin^2 2\theta_{13} \sin^2 \left(\frac{\Delta m^2_{31} L}{4E} \right) \tag{5.24}$$

see Equation 5.10 in Chapter 5.2.3.

The sensitivities on $\sin^2 2\theta_{13}$ of the accelerator beam experiments, the original Chooz experiment and the Double Chooz experiment are summarized in Table 5.7 on Page 142.

	Chooz	Double Chooz	Conventional Beams	J-PARK to SK	NuMI
Sensitivity Limit on $\sin^2 2\theta_{13}$ at 90% C.L.:					
$\sin^2 2\theta_{13}$	0.2	0.0032	0.061	0.023	0.024
Measurement if $\sin^2 2\theta_{13} = 0.1$ at 90% C.L.:					
$\sin^2 2\theta_{13}$	-	$0.1^{+0.034}_{-0.033}$	$0.1^{+0.104}_{-0.052}$	$0.1^{+0.067}_{-0.034}$	$0.1^{+0.083}_{-0.043}$

Table 5.7: Comparison of the sensitivites on $\sin^2 2\theta_{13}$ of future accelerator based experiments with the reactor experiments Chooz and Double Chooz [ARD 04], [HUB 04]. The column "Conventional Beams" gives the combined result for the MINOS, OPERA and ICARUS experiments for five years of data taking. The values reported for the superbeam experiments J-PARC to Super Kamiokande and NuMI are also for five years of data taking, whereas the numbers given for Double Chooz are for only three years data taking. All the results given for the beam experiments assume no further knowledge on other oscillation parameters than the current. These results might improve if parameter degeneracies can be resolved by other future measurements.

The sensitivity limit on $\sin^2 2\theta_{13}$ (at 90% C.L.) of 0.2 from the original Chooz experiment can be reduced down to 0.0032 by Double Chooz within 3 years of data taking. The other experiments available in this time frame which will be able to contribute to the measurement of $\sin^2 2\theta_{13}$ are OPERA, MINOS and ICARUS. If their results are combined, their sensitivity limit on $\sin^2 2\theta_{13}$ is just 0.061 at 90% C.L.. Only the future superbeam experiments J-PARC to Super Kamiokande and NuMI will be able to outperform Double Chooz in the sensitivity reached on $\sin^2 2\theta_{13}$ (see Table 5.7 on Page 142), yet on a comparatively longer time scale and at much greater effort. Their sensitivities are limited by degeneracies between different oscillation parameters in the oscillation probability $P_{\nu_\mu \to \nu_e}$, see Equation (5.23), if these degeneracies could be resolved by other measurements, the sensitivities reached for $\sin^2 2\theta_{13}$ could be as low as 0.004 (for the NuMI experiment at 90% C.L. [HUB 04]).

5.6 Conclusion

At this time, θ_{13} is the only neutrino mixing angle that has not been measured. The best limit on $\sin^2 2\theta_{13}$ of 0.2 (at 90% C.L. for $\Delta m^2_{32} = 2 \cdot 10^{-3}$ eV^2) comes from the Chooz reactor antineutrino experiment [CHO 98], [CHO 99], [CHO 00] and [CHO 03]. Whereas the solar and atmospheric mixing angles θ_{12} and θ_{23} have found to be maximal or large the smallness of θ_{13} remains mysterious. A measurement of $\sin^2 2\theta_{13}$ is of great interest. A nonzero value of θ_{13} can lead to interesting effects, like solar-atmospheric driven oscillation interferences [PET 02], [SCH 03] and if θ_{13} is large enough allow the measurement of the Dirac CP phase δ_{CP}, see also Chapter 1.2.2. The future Double Chooz experiment, for which a Letter of Intent has been published and partial funding has already been granted, will be able to provide the lowest upper limit on $\sin^2 2\theta_{13}$ of 0.0032 at 90% C.L. in the next five years (or a measurement, if θ_{13} is large enough). Better limits can only be achieved in the near future by the superbeam experiments J-PARC to Super Kamiokande and NuMI, in a time frame of approximately ten years though.

Chapter 6

Outlook: The LENA Detector

LENA is a planned large liquid scintillator detector for **L**ow **E**nergy **N**eutrino **A**stronomy. In a unique way it will simultaneously address topics from wide range in astrophysics, elementary particle physics and geophysics through the detection of galactic supernova neutrinos, supernova relic neutrinos, solar neutrinos, terrestrial neutrinos and accelerator produced neutrinos as well as proton decay.

6.1 Detector Design

The detector will have a large cylindrical liquid scintillator volume, approximately 30m in diameter and 90m long, which amounts to a target mass of $\approx$ 60 kt of liquid scintillator, see Figure 6.1 on Page 146. A geometrical coverage of $\approx$ 30% will be provided by 12,000 photomultipliers with a diameter of 50 cm each. To reduce background from cosmic rays the detector needs to be deep underground. So far two possible sites have been identified, one under water off the coast of Greece near Pylos at a depth of $\approx$ 5000 m and the other one at the Center for Underground Physics in Pyhäsalmi (CUPP, Finland) at a depth of 1400 m depth (i.e. $\approx$ 4060 m.w.e.). Both sites are far from nuclear power plants which could contribute to the $\bar{\nu}_E$ background in the search for relic supernovae neutrinos.

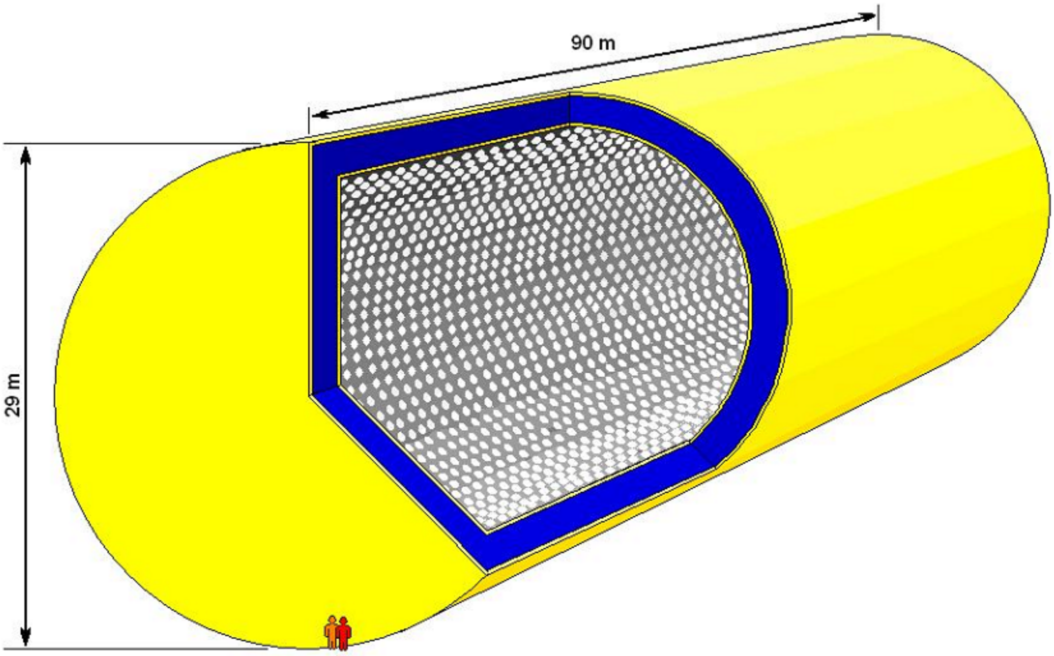

Figure 6.1: A schematic view of the LENA detector. It will use ≈ 60 kt liquid scintillator as target for neutrino detection. 12,000 photomultipliers provide a geometric coverage of ≈ 30%.

6.2 Physics Goals

6.2.1 Detection of Galactic Supernova Neutrinos

A supernova at the center of our galaxy would produce a total of ≈ 15,000 ν-events in LENA. Five different neutrino interaction in the organic scintillator will allow flavor specific neutrino/antineutrino detection:

	Reaction	Threshold	Events
1.	$\bar{\nu}_e + p \rightarrow e^+ + n$	Q = 1.8 MeV	7000
2.	$\bar{\nu}_e +^{12} C \rightarrow e^+ +^{12} B$	Q = 17.3 MeV	500
3.	$\nu_e +^{12} C \rightarrow^{12} N + e^-$	Q = 13.4 MeV	100
4.	$\nu_x +^{12} C \rightarrow^{12} C^* + \nu_x$		
	with $^{12}C^* \rightarrow^{12} C + \gamma$	E_γ = 15.1 MeV	4000
5.	$\nu_x + p \rightarrow \nu_x + p$	elastic scattering	2200

The charged current reactions (1) and (2) allow $\bar{\nu}_e$-spectroscopy. Reaction (1) can be tagged via the delayed coincidence between the prompt positron and the neutron capture on hydrogen, reaction (2) can be tagged through the decay of the daughter nucleus ^{12}B (β^-, $T_{1/2} = 20ms$). Spectroscopy of ν_es can be done with reaction (3). It can be tagged with the decay of the daughter nucleus ^{12}N (β^+, $T_{1/2} = 11ms$). The neutral current reaction (4) will provide information about the total Supernova-ν flux as all ν-flavors participate. Reaction (5) produces a low energy signal due to recoil protons.

If a supernova in the center of our galaxy could be observed with LENA, the time development of the specific ν-fluxes would give detailed insights about the explosion mechanism. Neutrino oscillations caused by matter effects as the supernova $\bar{\nu}_e$s cross the earth on their way to the detector would cause wiggles in the $\bar{\nu}_e$ energy spectrum. Observation of this spectral feature would give information about the neutrino oscillation parameters and the mass hierarchy ([LUN 01], [DIG 03]).

6.2.2 Detection of Supernova Relic Neutrinos

During the star formation history of the universe, supernovas have emitted a great number of neutrinos (so called supernova relic neutrinos, SRN). A measurement of the SRN-spectrum would provide a powerful handle to test models of the star formation history in the Universe. The Superkamiokande detector at this time provides the best limit on the SRN-flux of 1.2 $\mathrm{cm}^{-2}\mathrm{s}^{-1}$ for $\bar{\nu}_e$ with a threshold of 19.3 MeV [AND 03]. Due to the tagging of $\bar{\nu}_e$ interaction (see Chapter 6.2.1, reaction (1)), LENA will be able to suppress background well enough to reduce the energy threshold down to ≈9 MeV. A lower energy threshold than that will not be possible due to the ubiquitousness of $\bar{\nu}_e$'s from nuclear power plants. According to the current models of the star formation history an event rate of ≈ 4 SRN/year is expected in LENA.

6.2.3 Solar Neutrinos

Borexino and Kamland will be able to measure the solar ^{7}Be-ν flux, however the pep- and CNO-neutrinos will be difficult due to the low rates and the cosmic ray background [HAG 00]. LENA will measure rates of approximately 5400/day for ^{7}Be-νs, 150/day for pep-νs and 210/day for CNO-νs. This will allow to determine the ^{7}Be-ν flux with an accuracy of about 5% after only one year of measurement. If the ^{7}Be flux is known with this precision, together with the the solar luminosity and the oscillation parameters, the pp-ν flux can be inferred with an accuracy of better than 05% [BAH 03].

A very precise measurement of ^{7}Be-ν's with LENA would also allow to test temporal fluctuations of the solar density profile. Such temporal density fluctuations could be created by solar g-mode waves, which have not been observed so far by helioseismology. A density fluctuation of 1.5% would result in a ^{7}Be-ν flux change of about 10% [BAL 03].

6.2.4 Geoneutrinos

The thermal heat output of the Earth is about 40 TW (with a large uncertainty of ≈ 20%). It could be due to radioactivity in the Earth's crust, which could be measured with LENA by detecting the neutrinos from beta decays. How much of the thermal heat output is caused by radioactivity is largely unknown, but estimations are that LENA would see an event rate of geo-neutrinos in the range of (600 - 3000)/year.

6.2.5 Atmospheric Neutrinos

LENA will also allow to study the low energy part of atmospheric neutrinos between 100 MeV and 1 GeV via the following reactions:

$$\bar{\nu}_e + p \rightarrow e^+ + n$$
$$\bar{\nu}_\mu + p \rightarrow \mu^+ + n$$

The $\bar{\nu}_\mu$-events can be tagged by a threefold delayed coincidence between the prompt signal, the decay of the μ^+ and the neutron capture. The ratio between electron antineutrino and muon antineutrino events without oscillations should be $\bar{\nu}_e/\bar{\nu}_\mu = 0.5$. Any deviation from this is a sensitive probe for neutrino oscillations.

6.2.6 Long Baseline Experiment with LENA

Long baseline oscillation studies could be performed with LENA if a high energy neutrino beam were directed at it. LENA will be able to separate muon neutrino events from electron neutrino events via the different path lengths of the muon and the electron in the detector. For this purpose, the axis of the detector should be parallel to the neutrino beam. Muon events could also be tagged by the decay of the μ^+. The possible detector site Pylos is off-axis to CERN to Gran Sasso neutrino beam (coincidentally).

6.2.7 Proton Decay

The favored decay mode of the proton by SUSY models is $p \rightarrow K^+\nu$. As the energy of the Kaon is below the Čerenkov threshold, LENA would have a clear advantage over water erenkov detectors. LENA could detect this decay mode of the proton in the following way:

- The Kaon decay via $K^+ \rightarrow \mu^+\nu_\mu$ with a branching of 63.5% can be tagged with a threefold delayed coincidence:
    1. prompt mono-energetic K$^+$ (T=105 MeV)
    2. short delayed (τ=12.8 ns) mono-energetic μ^+ (T=152 MeV)
    3. long delayed (τ=2.2 ms) e^+ from the following μ^+ decay

- The Kaon decay via $K^+ \rightarrow \pi^+\pi^0$ with a branching of 21.2% can be tagged with a fourfold delayed coincidence:
    1. prompt mono-energetic K^+ (T=105 MeV)
    2. short delayed mono-energetic π^+ (T=108 MeV) accompanied by an electromagnetic shower due to the 2-γ decay of the π^0 (E=246 MeV)
    3. short delayed (τ=26 ns) mono-energetic μ^+ with T = 4 MeV from the π^+ decay
    4. long delayed (τ=2.2 ms) e^+ from the μ^+ decay

Therefore, LENA should be able to search for the proton decay in the channel $p \rightarrow K^+\nu$ practically background free. The expected sensitivity for this decay channel is a lifetime limit of between 10^{34} and 10^{35} years after a measuring time of 10 years. The minimal SUSY SU(5) model predicts the decay mode $p \rightarrow K^+\nu$ to be dominant with a partial lifetime varying from 10^{29} to 10^{35} years [BAB 97]. At this time the best limit on this decay mode from Super Kamiokande is 6.7×10^{32} years (at 90% C.L.) [HAY 99].

Chapter 7

Conclusion

Neutrino physics has made tremendous progress since the “problem of the missing neutrinos” was first discovered. Neutrino oscillations have been identified as the cause for a lack of neutrinos of a certain flavor after the neutrinos have traveled over a certain distance. The phenomenon is understood, and two neutrino mixing angles have been measured: $\tan^2\theta_{12} = 0.40^{+0.10}_{-0.07}$ and $\sin^2 2\theta_{23} = 1^{+0}_{-0.1}$, as well as the mass squared differences between the neutrino mass eigenstates. However, there are still numerous issues to be addressed in neutrino physics, the measurement of the solar ^{7}Be-ν flux as well as the pp-, pep- and CNO neutrino flux from the sun. The third mixing angle θ_{13} has not been measured yet, and an improvement in the precision of θ_{12} and θ_{23} will still be needed. The absolute masses of the neutrinos are still unknown as well as whether neutrinos are Dirac or Majorana particles. All of these issues are either currently investigated or will be addressed by experiments in the near future.

One of these experiments is Borexino. For Borexino (and the CTF), light guides have been developed, manufactured and installed which increase the light yield by a factor of 2.5 for Borexino (8.8 for the CTF). In Borexino, a light guide cost only $\approx 5\%$ of a fully equipped photomultiplier, therefore saving a substantial amount of money. At the same time, the radioactive background introduced by the light guides in Borexino is negligible. A Monte Carlo simulation has been developed to determine the efficiency of the Germanium detector used to measure the radioactive contamination of the light guides. This simulation has been tested with radioactive references and has proven to be very accurate. Consequently, the radioactive contaminations in the light guides could be measured with high accuracy. Another Monte Carlo simulation was developed then to determine the background caused in Borexino by the light guides and the photomultipliers. The simulation yielded a background contribution of (0.08 ± 0.04) events/day in the^{7}Be-ν window for the light guides, and (0.15 ± 0.05) events/day for the photomultipliers, compared to an expected ^{7}Be-ν event rate of ≈ 30/day. This technique of increasing the light yield will be of great value for future photomultiplier-based experiments.

Also, in Borexino a Source Calibration System will allow to insert radioactive sources into Borexino for calibration of the detector. These sources can be moved around freely and the Source Locating System is able to determine the source's position independently from the photomultiplier timing information, via optical triangulation of an LED mounted on the source. A software has been developed which reduces the fairly complicated triangulation process with digital cameras to a push-button system. It can automatically take pictures with seven cameras, download the pictures, process and analyze them to find the LED on each of them, apply lens corrections and then calculate the LED's position and the sources's position. The accuracy of the Source Locating System has been tested and exceeds the design specification. Additionally, the presence of remote controlled digital cameras inside the detector will allow visual inspection once the detector is sealed, which will be of great value during the complicated and dangerous filling procedure of Borexino.

The first future detector to further probe the third mixing angle θ_{13} will most likely be Double Chooz. It has a very promising potential finding an upper limit for $\sin^2 2\theta_{13}$ of 0.0032 at 90% C.L. in the next five years. Fast external neutrons could pose a serious threat to this experiment, as they can mimic the delayed coincidence used to tag the reactor $\bar{\nu}_e$-events. A Monte Carlo Simulation, which calculates this background starting form the cosmic ray muons, has been developed and successfully tested by comparison with the measurement of this type background in the original Chooz experiment. This simulation yields upper limits for the background introduced by fast external neutrons of 0.2 counts/day at 90% C.L for the far Double Chooz detector and 2.2 counts/day at 90% C.L. for the near Double Chooz detector.

Finally, the new LENA experiment, which is envisioned for the future, could use neutrinos as probes to address topics in astrohysics, cosmology and geophysics and particle physics. It could study solar, atmospheric and geo-neutrinos, supernova and supernova relic neutrinos as well as accelerator neutrinos. Moreover, it could be used to study proton decay. Therefore, LENA could start a new era in neutrino physics, moving from a mere neutrino detector to being a true observatory.

Abbreviations

BBN:	Big Bang Nucleosynthesis
bis-MSB:	1,4-bis-(2-Methylstyryl)-Benzol
CCD:	Charge Coupled Device (Imaging device in digital cameras)
CTF:	Counting Test Facility (The Borexino Prototype)
DMP:	Dimethylphtalate
EG:	Electron Gamma Shower (a simulation toolkit)
FLOP:	Floating Point Operations per second
IV:	Inner vessel
LED:	Light Emitting Diode
OV:	Outer Vessel
PC:	Pseudocumene (1,2,4-Trimethylbenzene)
PMT, PM:	Photomultiplier tube
PPO:	2,5-Diphenyloxazole
pTB:	p-Diphenylbenzol
PXE:	PXE, Phenyl-o-xylylethan
SDSS:	Sloan Digital Sky Survey
SNO:	Sudbury Neutrino Observatory
SSS:	Stainless steel sphere
WMAP:	Wilkinson Microwave Anisotropy Probe)

List of Figures

List of Tables

Bibliography

[AAL 99] C. E. Aalseth *et al.* [IGEX Collaboration], “Neutrinoless double-beta decay of Ge-76: First results from the International Germanium Experiment (IGEX) with six isotopically enriched detectors”, Phys. Rev. C 59 (1999) 2108.

[AAL 02-1] C. E. Aalseth *et al.* [IGEX Collaboration], “The IGEX Ge-76 neutrinoless double-beta decay experiment: Prospects for next generation experiments”, Phys. Rev. D 65 (2002) 092007 [arXiv:hep-ex/0202026].

[AAL 02-2] C. E. Aalseth *et al.*, “Comment on ’Evidence for neutrinoless double beta decay’ ”, Mod. Phys. Lett. A 17 (2002) 1475 [arXiv:hep-ex/0202018].

[AAL 02-3] C. E. Aalseth *et al.* [Majorana Collaboration], “The Majorana Ge-76 double-beta decay project”, arXiv:hep-ex/0201021.

[ABD 99] J. N. Abdurashitov *et al.* [SAGE Collaboration],“Measurement of the solar neutrino capture rate with gallium metal”, Phys. Rev. C 60 (1999) 055801 [arXiv:astro-ph/9907113].

[ABD 02] J. N. Abdurashitov *et al.* [SAGE Collaboration], “Measurement of the solar neutrino capture rate by the Russian-American gallium solar neutrino experiment during one half of the 22-year cycle of solar activity”, J. Exp. Theor. Phys. 95 (2002) 181 [Zh. Eksp. Teor. Fiz. 122 (2002) 211] [arXiv:astro-ph/0204245].

[ABL 95] MINOS Collaboration (E. Ables *et al.*), “Addendum To P-875: A Long Baseline Neutrino Oscillation Experiment At Fermilab”, FERMILAB-PROPOSAL-P-875-ADD, NUMI-L-79, Apr 1995. 241pp.

[ABT 04] I. Abt *et al.*, “A new Ge-76 double beta decay experiment at LNGS”, arXiv:hep-ex/0404039.

[AGO 03] S. Agostinelli *et al.*, “Geant4 - A Simulation Toolkit”, Nuclear Instruments and Methods A 506 (2003) 250.

[AGU 01] A. Aguilar *et al.* [LSND Collaboration], “Evidence for neutrino oscillations from the observation of anti-nu/e appearance in a anti-nu/mu beam”, Phys. Rev. D 64 (2001) 112007 [arXiv:hep-ex/0104049].

[AHM 02] Q. R. Ahmad *et al.* [SNO Collaboration], “Direct evidence for neutrino flavor transformation from neutral-current interactions in the Sudbury Neutrino Observatory”, Phys. Rev. Lett. 89 (2002) 011301 [arXiv:nucl-ex/0204008].

[AHM 02-2] Q. R. Ahmad *et al.* [SNO Collaboration], “Measurement of day and night neutrino energy spectra at SNO and constraints on neutrino mixing parameters”, Phys. Rev. Lett. 89 (2002) 011302 [arXiv:nucl-ex/0204009].

[AHM 03] S. N. Ahmed *et al.* [SNO Collaboration], “Measurement of the total active B-8 solar neutrino flux at the Sudbury Neutrino Observatory with enhanced neutral current sensitivity”, Phys. Rev. Lett. 92 (2004) 181301 [arXiv:nucl-ex/0309004].

[AHN 01] S. H. Ahn *et al.* [K2K Collaboration], “Detection of accelerator produced neutrinos at a distance of 250-km”, Phys. Lett. B 511 (2001) 178 [arXiv:hep-ex/0103001].

[AHN 02] M. H. Ahn *et al.* [K2K Collaboration], “Indications of neutrino oscillation in a 250-km long-baseline experiment”, Phys. Rev. Lett. 90 (2003) 041801 [arXiv:hep-ex/0212007].

[AKH 04] E. K. Akhmedov, R. Johansson, M. Lindner, T. Ohlsson and T. Schwetz, “Series expansions for three-flavor neutrino oscillation probabilities in matter”, JHEP 0404 (2004) 078 [arXiv:hep-ph/0402175].

[ALI 98-1] G. Alimonti *et al.*, “A large-scale low-background liquid scintillation detector: the counting test facility at Gran Sasso”, Nucl. Instrum. Meth. A 406 (1998) p.411.

[ALI 98-2] G. Alimonti *et al.*, Borexino Collaboration, "Ultra-low background measurements in a large volume underground detector", Astroparticle Physics 8 (1998) 141.

[ALI 00] G. Alimonti *et al.*, Borexino Collaboration, "Light propagation in a large volume liquid scintillator", Nucl. Instrum. Meth. A 440 (2000) p.360.

[ALI 02] G. Alimonti *et al.*, Borexino Collaboration, "Science and Technology of Borexino: A Real Time Detector for Low Energy Solar Neutrinos", Astroparticle Physics 16 (2002) p.205.

[ALL 96] W. W. M. Allison *et al.*, "Measurement of the atmospheric neutrino flavour composition in Soudan-2", Phys. Lett. B 391 (1997) 491 [arXiv:hep-ex/9611007].

[ALL 99] W. W. M. Allison *et al.* [Soudan-2 Collaboration], "The atmospheric neutrino flavor ratio from a 3.9 fiducial kiloton-year exposure of Soudan 2", Phys. Lett. B 449 (1999) 137 [arXiv:hep-ex/9901024].

[AMB 98] M. Ambrosio *et al.* [MACRO Collaboration], "Measurement of the atmospheric neutrino-induced upgoing muon flux using MACRO", Phys. Lett. B 434 (1998) 451.

[AMB 00] M. Ambrosio *et al.* [MACRO Collaboration], "Low energy atmospheric muon neutrinos in MACRO", Phys. Lett. B 478 (2000) 5 [arXiv:hep-ex/0001044].

[AMB 01] M. Ambrosio *et al.* [MACRO Collaboration], "Matter effects in upward-going muons and sterile neutrino oscillations", Phys. Lett. B 517 (2001) 59 [arXiv:hep-ex/0106049].

[AMB 03] M. Ambrosio *et al.* [MACRO Collaboration], "Atmospheric neutrino oscillations from upward throughgoing muon multiple scattering in MACRO", Phys. Lett. B 566, 35 (2003) [arXiv:hep-ex/0304037].

[AND 03] S. Ando, "Decaying neutrinos and implications from the supernova relic neutrino observation", Phys. Lett. B 570 (2003) 11 [arXiv:hep-ph/0307169].

[ANS 92] P. Anselmann *et al.* [GALLEX Collaboration], “Solar neutrinos observed by GALLEX at Gran Sasso”, Phys. Lett. B 285 (1992) 376.

[APR 02] P. Aprili *et al.*, (ICARUS Collaboration), “The ICARUS experiment: A second-generation proton decay experiment and neutrino observatory at the Gran Sasso laboratory. Cloning of T600 modules to reach the design sensitive mass. (Addendum)”, CERN-SPSC-2002-027 (2002).

[ARA 04] T. Araki *et al.* [KamLAND Collaboration], “Measurement of neutrino oscillation with KamLAND: Evidence of spectral distortion”, arXiv:hep-ex/0406035.

[ARD 04] F.Ardellier *et al.*, “Letter of Intent for Double-CHOOZ: a Search for the Mixing Angle θ_{13}”, hep-ex/0405032 (2004).

[ARI 86] K. Arisaka *et al.*, “Search For Nucleon Decay Into Charged Lepton + Mesons”, J. Phys. Soc. Jap. 54 (1985) 3213.

[ARM 02] B. Armbruster *et al.* [KARMEN Collaboration], “Upper limits for neutrino oscillations anti-nu/mu → anti-nu/e from muon decay at rest”, Phys. Rev. D 65 (2002) 112001 [arXiv:hep-ex/0203021].

[ARN 03] C. Arnaboldi *et al.* [CUORE Collaboration],“Physics potential and prospects for the CUORICINO and CUORE experiments”, Astropart. Phys. 20 (2003) 91 [arXiv:hep-ex/0302021].

[ASH 04] Y. Ashie *et al.* [Super-Kamiokande Collaboration], “Evidence for an oscillatory signature in atmospheric neutrino oscillation”, Phys. Rev. Lett. 93 (2004) 101801 [arXiv:hep-ex/0404034].

[ASR 03] A. Asratyan, G. Davidenko, A. Dolgolenko, V. Kaftanov, M. Kubantsev and V. Verebryusov, “Neutrino superbeams and the magic baseline”, arXiv:hep-ex/0303023.

[ATH 96] C. Athanassopoulos *et al.* [LSND Collaboration], “Evidence for anti-nu/mu → anti-nu/e oscillation from the LSND experiment at the Los Alamos Meson Physics Facility”, Phys. Rev. Lett. 77 (1996) 3082 [arXiv:nucl-ex/9605003].

[ATH 97] C. Athanassopoulos *et al.* [LSND Collaboration], “Evidence for nu/mu → nu/e neutrino oscillations from LSND”, Phys. Rev. Lett. 81 (1998) 1774 [arXiv:nucl-ex/9709006].

[AYR 01] D. Ayres *et al.* [Nova Collaboration], “Letter of intent to build an off-axis detector to study nu/mu → nu/e oscillations with the NuMI neutrino beam”, arXiv:hep-ex/0210005.

[BAB 97] K. S. Babu, J. C. Pati and F. Wilczek, “Suggested new modes in supersymmetric proton decay”, Phys. Lett. B 423 (1998) 337 [arXiv:hep-ph/9712307].

[BAC 04-1] H. Back, C. Grieb, B. Vogelaar, “Calibration Source Locating System for the Borexino Solar Neutrino Experiment”, submitted to Nucl. Instrum. Meth. A (2004).

[BAC 04-2] H. Back, “Internal Radioactive Source Calibration of the Borexino Solar Neutrino Experiment”, Ph.D. Thesis, Virginia Polytechnic Institute & State University (2004).

[BAH 95] J. N. Bahcall and M. H. Pinsonneault, “Solar models with helium and heavy element diffusion”, Rev. Mod. Phys. 67 (1995) 781 [arXiv:hep-ph/9505425].

[BAH 01] J. N. Bahcall, M. H. Pinsonneault and S. Basu, “Solar models: Current epoch and time dependences, neutrinos, and helioseismological properties”, Astrophys. J. 555 (2001) 990 [arXiv:astro-ph/0010346].

[BAH 03] J. N. Bahcall and C. Pena-Garay, “Global analyses as a road map to solar neutrino fluxes and oscillation parameters”, JHEP 0311 (2003) 004 [arXiv:hep-ph/0305159].

[BAH 04] J. Bahcall, M. Gonzalez-Garcia and C. Peña-Garay, “Solar Neutrinos Before and After Neutrino 2004”, hep-ph/0406294 (2004).

[BAL 03] A. B. Balantekin and H. Yuksel, “Do the KamLAND and solar neutrino data rule out solar density fluctuations?”, Phys. Rev. D 68 (2003) 013006 [arXiv:hep-ph/0303169].

[BAR 80] V. D. Barger, K. Whisnant, S. Pakvasa and R. J. N. Phillips, “Matter Effects On Three-Neutrino Oscillations”, Phys. Rev. D 22 (1980) 2718.

[BAR 98] V. D. Barger, S. Pakvasa, T. J. Weiler and K. Whisnant, "Variations on four-neutrino oscillations", Phys. Rev. D 58 (1998) 093016 [arXiv:hep-ph/9806328].

[BAR 01] V. D. Barger, D. Marfatia, K. Whisnant and B. P. Wood, "Earth regeneration of solar neutrinos at SNO and SuperKamiokande", Phys. Rev. D 64 (2001) 073009 [arXiv:hep-ph/0104095].

[BAR 03-1] V. Barger, D. Marfatia and K. Whisnant, "Progress in the physics of massive neutrinos", Int. J. Mod. Phys. E 12 (2003) 569 [arXiv:hep-ph/0308123].

[BAR 03-2] V. Barger, D. Marfatia and A. Tregre, "Neutrino mass limits from SDSS, 2dFGRS and WMAP", Phys. Lett. B 595 (2004) 55 [arXiv:hep-ph/0312065].

[BAR 03-3] V. Barger, J. P. Kneller, H. S. Lee, D. Marfatia and G. Steigman, "Effective number of neutrinos and baryon asymmetry from BBN and WMAP", Phys. Lett. B 566 (2003) 8 [arXiv:hep-ph/0305075].

[BET 39] H. A. Bethe, "Energy Production in Stars", Phys. Rev. Lett. 55, 434 (1939).

[BEN 03] C. L. Bennett *et al.*, "First Year Wilkinson Microwave Anisotropy Probe (WMAP) Observations: Preliminary Maps and Basic Results", Astrophys. J. Suppl. 148 (2003) 1 [arXiv:astro-ph/0302207].

[BIL98] S. M. Bilenky, C. Giunti and W. Grimus, "Phenomenology of neutrino oscillations", Prog. Part. Nucl. Phys. 43 (1999) 1 [arXiv:hep-ph/9812360].

[BOG 99] J. Boger *et al.* [SNO Collaboration], "The Sudbury Neutrino Observatory", Nucl. Instrum. Meth. A **449** (2000) 172 [arXiv:nucl-ex/9910016].

[BOR 03] L. Bornschein [KATRIN Collaboration], "KATRIN: Direct measurement of neutrino masses in the sub-eV region", eConf C030626 (2003) FRAP14 [arXiv:hep-ex/0309007].

[BUC 04] C. Buck, "Development of metal loaded liquid scintillators for future detectors to investigate neutrino properties", Dissertation, Ruperto-Carola Universität Heidelberg (2004).

[CAD 01] L. Cadonati, “The Borexino Solar Neutrino Experiment and its Scintillator Containment Vessel”, Ph.D. Thesis (2001).

[CEC 79] R. A. Cecil, B. D. Anderson and R. Madey, “Improved Predictions Of Neutron Detection Efficiency For Hydrocarbon Scintillators From 1-Mev To About 300-Mev”, Nucl. Instrum. Meth. 161 (1979) 439.

[CHO 98] M. Apollonio *et al.*, Chooz Collaboration, “Initial Results From The Chooz Long Baseline Reactor Neutrino Oscillation Experiment”, Phys. Lett. B420 397 (1998).

[CHO 99] M. Apollonio *et al.*, Chooz Collaboration, “Limits on Neutrino Oscillations from the Chooz Experiment”, Phys. Lett. B466 415 (1999).

[CHO 00] M. Apollonio *et al.*, Chooz Collaboration, “Determination of neutrino incoming direction in the Chooz experiment and Supernova explosion location by scintillator detectors”, Phys. Rev. D61 012001 (2000).

[CHO 03] M. Apollonio *et al.*, Chooz Collaboration, “Search for neutrino oscillations on a long base-line at the CHOOZ nuclear power station”, Phys. Eur. Phys. J. C27 331 (2003).

[COL 01] M. Colless *et al.* [The 2DFGRS Collaboration], “The 2dF Galaxy Redshift Survey: Spectra and redshifts”, Mon. Not. Roy. Astron. Soc. 328 (2001) 1039 [arXiv:astro-ph/0106498].

[CRI 99] M. Cribier [GALLEX Collaboration], “Results of the whole GALLEX experiment,” Nucl. Phys. Proc. Suppl. 70 (1999) 284.

[DAV 96] R. Davis, Nucl. Phys. B (Proc. Suppl.) 48 (1996) 284.

[DEM 99] A. Dementyev, V. Gurentsov, O. Ryazhskaya and N. Sobolevsky, “Production and transport of hadrons generated in nuclear cascades initiated by muons in the rock (exclusive approach)”, Nucl. Phys. B (Proc. Suppl.) 70 486 (1999).

[DIG 03] A. S. Dighe, M. T. Keil and G. G. Raffelt, “Identifying earth matter effects on supernova neutrinos at a single detector”, JCAP 0306 (2003) 006 [arXiv:hep-ph/0304150].

[DUC 02] D. Duchesneau [OPERA Collaboration], "The CERN - Gran Sasso neutrino program", eConf C0209101 (2002) TH09 [Nucl. Phys. Proc. Suppl. 123 (2003) 279] [arXiv:hep-ex/0209082].

[EIT 00] K. Eitel [KARMEN Collaboration], "Latest results of the KARMEN2 experiment", Nucl. Phys. Proc. Suppl. 91 (2000) 191 [arXiv:hep-ex/0008002].

[EJI 03] H. Ejiri *et al.* [MOON Collaboration], "MOON (Mo Observatory Of Neutrinos) for neutrino studies by double beta decays and low energy solar neutrinos", http://www.slac.stanford.edu/spires/find/hep/www?irn=6028500 *Prepared for 4th Workshop on Neutrino Oscillations and their Origin (NOON2003), Kanazawa, Japan, 10-14 Feb 2003*

[ELL 02] S. R. Elliott and P. Vogel, "Double beta decay", Ann. Rev. Nucl. Part. Sci. 52 (2002) 115 [arXiv:hep-ph/0202264].

[FAE 99] A. Faessler and F. Simkovic, "Double beta decay", J. Phys. G 24 (1998) 2139 [arXiv:hep-ph/9901215].

[FER 34] E. Fermi, Z. Phys. 88, 161 (1934), translated in F. L. Wilson, Am. J. Phys. 36, 1150 (1960).

[FIR 96] Richard B.Firestone, "Table of Isotopes", Wiley (1996).

[FUK 96] Y. Fukuda *et al.* [Kamiokande Collaboration], "Solar neutrino data covering solar cycle 22", Phys. Rev. Lett. 77 (1996) 1683.

[FUK 98-1] Y. Fukuda *et al.* [Super-Kamiokande Collaboration], "Measurement of a small atmospheric nu/mu / nu/e ratio", Phys. Lett. B 433 (1998) 9 [arXiv:hep-ex/9803006].

[FUK 98-2] Y. Fukuda *et al.* [Super-Kamiokande Collaboration], "Study of the atmospheric neutrino flux in the multi-GeV energy range", Phys. Lett. B 436 (1998) 33 [arXiv:hep-ex/9805006].

[GAV 89] V. N. Gavrin *et al.* [SAGE Collaboration], "The Baksan Gallium Solar Neutrino Experiment", Nucl. Phys. Proc. Suppl. 16 (1990) 483.

[GOL 58] M. Goldhaber, L. Grodzins and A. W. Sunyar, "Helicity Of Neutrinos", Phys. Rev. 109 (1958) 1015.

[GON 02] M. C. Gonzalez-Garcia and Y. Nir, "Developments in neutrino physics", Rev. Mod. Phys. 75 (2003) 345 [arXiv:hep-ph/0202058].

[GRI 69] V. N. Gribov and B. Pontecorvo, "Neutrino astronomy and lepton charge", Phys. Lett. B28 (1969), 493.

[GRI 00] C. Grieb, "Untersuchungen zu Szintillatorreinigung mit Kieselgel, Studien zum Untergrund und Vakuumneutrinooszillationen in Borexino", Diploma Thesis, Technische Universität München (2000).

[GUN 97] M. Gunther *et al.*, "Heidelberg - Moscow beta beta experiment with Ge-76: Full setup with five detectors," Phys. Rev. D 55 (1997) 54.

[HAG 00] T. Hagner *et al.*, "Muon-induced production of radioactive isotopes in scintillation detectors", Astroparticle Physics 14 (2000) 33.

[HAG 02] K. Hagiwara *et al.* [Particle Data Group Collaboration], "Review of particle physics", Phys. Rev. D 66 (2002) 010001.

[HAM 96] W. Hampel *et al.* [GALLEX Collaboration], "GALLEX solar neutrino observations: Results for GALLEX III", Phys. Lett. B 388 (1996) 384.

[HAM 98] W. Hampel *et al.* [GALLEX Collaboration], "GALLEX solar neutrino observations: Results for GALLEX IV", Phys. Lett. B 447 (1999) 127.

[HAY 99] Y. Hayato *et al.* [Super-Kamiokande Collaboration], "Search for proton decay through p → anti-nu K+ in a large water Cherenkov detector", Phys. Rev. Lett. 83 (1999) 1529 [arXiv:hep-ex/9904020].

[HEI 98] Bernhard Heisinger, "Myonen-induzierte Produktion von Radionukliden", Ph.D. Thesis Technische Universtität München (1998).

[HIN 03] G. Hinshaw *et al.*, "First Year Wilkinson Microwave Anisotropy Probe (WMAP) Observations: Angular Power Spectrum", Astrophys. J. Suppl. 148 (2003) 135 [arXiv:astro-ph/0302217].

[HIR 88] K. S. Hirata *et al.* [KAMIOKANDE-II Collaboration], "Experimental Study Of The Atmospheric Neutrino Flux", Phys. Lett. B 205 (1988) 416.

[HIR 92] K. S. Hirata *et al.* [Kamiokande-II Collaboration], “Observation of a small atmospheric ν_μ/ν_e ratio in Kamiokande”, Phys. Lett. B 280 (1992) 146.

[HOL 92] E. Holzschuh, “Measurement of the neutrino mass from tritium beta decay”, Rept. Prog. Phys. 55 (1992) 1035.

[HUB 02] P. Huber, M. Lindner, T. Schwetz and W. Winter, “Reactor neutrino experiments compared to superbeams”, Nucl. Phys. B 665 (2003) 487.

[HUB 03] P. Huber, M. Lindner and W. Winter, “Synergies between the first-generation JHF-SK and NuMI superbeam experiments”, Nucl. Phys. B 654 (2003) 3 [arXiv:hep-ph/0211300].

[HUB 04] P. Huber, M. Lindner, M. Rolinec, T. Schwetz and W. Winter, “Prospects of accelerator and reactor neutrino oscillation experiments for the coming ten years”, arXiv:hep-ph/0403068.

[ITO 01] Y. Itow *et al.*, “The JHF-Kamioka neutrino project”, arXiv:hep-ex/0106019.

[ISH 04] Masaki Ishitsuka, “L/E analysis of the atmospheric neutrino data from Super-Kamiokande”, Dissertation, University of Tokyo, (2004).

[KAJ 86] T. Kajita *et al.*, “Search For Nucleon Decays Into Anti-Neutrino + Mesons”, J. Phys. Soc. Jap. 55 (1986) 711.

[KAW 03] I. Kawrakow and D.W.O. Rogers, “The EGSnrc Code System: Monte Carlo Simulation of Electron and Photon Transport”, http://www.irs.inms.nrc.ca/inms/irs/EGSnrc/EGSnrc.html (2003).

[KEA 04] E. Kearns (Super-Kamiokande Collaboration), “Atmospheric neutrino results from SuperKamiokande, 2004.”, Neutrino 2004, 13-19 June 2004, Paris, France. http://neutrino2004.in2p3.fr/slides/tuesday/kearns.pdf.

[KLA 99] H. V. Klapdor-Kleingrothaus *et al.* [GENIUS Collaboration], “GENIUS: A supersensitive germanium detector system for rare events”, arXiv:hep-ph/9910205.

[KLA 00] H. V. Klapdor-Kleingrothaus *et al.*, “Latest results from the Heidelberg-Moscow double-beta-decay experiment”, Eur. Phys. J. A 12 (2001) 147 [arXiv:hep-ph/0103062].

[KLA 02] H. V. Klapdor-Kleingrothaus, “Reply to a comment of article ’Evidence for neutrinoless double beta decay’ ”, arXiv:hep-ph/0205228.

[KOD 00] K. Kodama *et al.* [DONUT Collaboration], “Observation of tau-neutrino interactions”, Phys. Lett. B 504 (2001) 218 [arXiv:hep-ex/0012035].

[KOS 92] M. Koshiba, “Observational neutrino astrophysics”, Phys. Rept. 220 (1992) 229.

[LOB 01] V. M. Lobashev *et al.*, “Direct search for neutrino mass and anomaly in the tritium beta-spectrum: Status of ’Troitsk neutrino mass’ experiment”, Nucl. Phys. Proc. Suppl. 91 (2001) 280.

[LOB 02] V. M. Lobashev, “Study of the tritium beta-spectrum in experiment ’Troitsk nu-mass’ ”, Prog. Part. Nucl. Phys. 48 (2002) 123.

[LUN 01] C. Lunardini and A. Y. Smirnov, “Supernova neutrinos: Earth matter effects and neutrino mass spectrum”, Nucl. Phys. B 616 (2001) 307 [arXiv:hep-ph/0106149].

[MAI 70] K. H. Maier and J. Nitschke, “Die lichtausbeute eines NE 213-szintillators fr protonen”, Nuclear Instruments and Methods 59 (1968) 227.

[MAK 62] Z. Maki, M. Nakagawa and S. Sakata, “Remarks On The Unified Model Of Elementary Particles”, Prog. Theor. Phys. 28 (1962) 870.

[MAL 02] M. Maltoni, T. Schwetz, M. A. Tortola and J. W. F. Valle, “Ruling out four-neutrino oscillation interpretations of the LSND anomaly?”, Nucl. Phys. B 643 (2002) 321 [arXiv:hep-ph/0207157].

[MAR 02] M. Maris and S. T. Petcov, “On the day-night effect and CC to NC event rate ratio predictions for the SNO detector”, Phys. Lett. B 534 (2002) 17 [arXiv:hep-ph/0201087].

[MCK 80] B. H. J. McKellar, “The Influence Of Mixing Of Finite Mass Neutrinos On Beta Decay Spectra”, Phys. Lett. B 7 (1980) 93.

[LED 78] C. Lederer, V. Shirley, "Table of Isotopes", Wiley (1978).

[MIK 85] S.P. Mikheev and A.Yu. Smirnov, "Resonant amplification of neutrino oscillations in matter and spectroscopy of solar neutrinos", Yad. Fiz. 42:1441-1448, (1985) [Sov.J. Nucl. Phys. 42:913-917, (1985).]

[MIK 86] S.P. Mikheev and A.Yu. Smirnov, "Resonant amplification of neutrino oscillations in matter and solar neutrino spectroscopy", Nuovo Cim. C9:17-26, 1986.

[MIN 01] H. Minakata and H. Nunokawa, "Exploring neutrino mixing with low energy superbeams", JHEP 0110 (2001) 001 [arXiv:hep-ph/0108085].

[MIN 02] H. Minakata, H. Sugiyama, O. Yasuda, K. Inoue and F. Suekane, "Reactor measurement of Theta(13) and its complementarity to long-baseline experiments", Phys. Rev. D 68 (2003) 033017.

[MOR 03] S. Moriyama [XMASS Collaboration], "XMASS experiment", http://www.slac.stanford.edu/spires/find/hep/www?irn=6028543 *Prepared for 4th Workshop on Neutrino Oscillations and their Origin (NOON2003), Kanazawa, Japan, 10-14 Feb 2003*

[OBE 03] L. Oberauer, C. Grieb, F. von Feilitzsch and I. Manno, "Light concentrators for Borexino and CTF", Nucl. Instrum. Meth. A 530 (2004) 453.

[OHL 00] T. Ohlsson and H. Snellman, "Three flavor neutrino oscillations in matter", J. Math. Phys. 41 (2000) 2768 [Erratum-ibid. 42 (2001) 2345] [arXiv:hep-ph/9910546].

[OKA] N. Okada and O. Yasuda, "A sterile neutrino scenario constrained by experiments and cosmology", Int. J. Mod. Phys. A 12 (1997) 3669 [arXiv:hep-ph/9606411].

[OSI 01] A. Osipowicz *et al.* [KATRIN Collaboration], "KATRIN: A next generation tritium beta decay experiment with sub-eV sensitivity for the electron neutrino mass", arXiv:hep-ex/0109033.

[PAU 30] W. Pauli, letter to Tübingen Conference, December 4, 1930, translated in L.M. Brown, Phys. Today 23, Sept. 1978.

[PER 01] W. J. Percival *et al.* [The 2dFGRS Collaboration], "The 2dF Galaxy Redshift Survey: The power spectrum and the matter content of the universe", Mon. Not. Roy. Astron. Soc. 327 (2001) 1297 [arXiv:astro-ph/0105252].

[PON 68] B. Pontecorvo, "Neutrino experiments and the question of leptonic-charge conservation", Sov. Phys. JETP 26 (1968), 984.

[PDG 00] Particle Data Group, Europ. Phys. J. C15 (2000), 692.

[PET 02] S. T. Petcov and M. Piai, "The LMA MSW solution of the solar neutrino problem, inverted neutrino mass hierarchy and reactor neutrino experiments", Phys. Lett. B 533 (2002) 94 [arXiv:hep-ph/0112074].

[PIE 01] A. Piepke [KamLAND Collaboration], "KamLAND: A reactor neutrino experiment testing the solar neutrino anomaly", Nucl. Phys. Proc. Suppl. 91 (2001) 99.

[REI 57] F. Reines and C. L. Cowan, "Neutrino Physics", Phys. Today 10N8 (1957) 12.

[REI 60] F. Reines, C. L. Cowan, F. B. Harrison, A. D. McGuire and H. W. Kruse, "Detection Of The Free Anti-Neutrino", Phys. Rev. 117 (1960) 159.

[REI 95] F. Reines, "The Neutrino: From Poltergeist to Particle", Nobel Lectures, Physics 1991-1995, World Scientific Publishing Co., Singapore, 1997

[SAN 03] M. Sanchez *et al.* [Soudan 2 Collaboration], "Observation of atmospheric neutrino oscillations in Soudan 2", Phys. Rev. D 68 (2003) 113004 [arXiv:hep-ex/0307069].

[SCH 00] S. Schonert [LENS Collaboration], "LENS: Spectroscopy of low energy solar neutrinos", http://www.slac.stanford.edu/spires/find/hep/www?irn=4867050 SPIRES entry *Prepared for 30th International Conference on High-Energy Physics (ICHEP 2000), Osaka, Japan, 27 Jul - 2 Aug 2000*

[SCH 03] S. Schonert, T. Lasserre and L. Oberauer, “The HLMA project: Determination of high Delta(m**2) LMA mixing parameters and constraint on |U(e3)| with a new reactor neutrino experiment”, Astropart. Phys. 18 (2003) 565 [arXiv:hep-ex/0203013].

[SNO 02] Q. R. Ahmad *et al.* [SNO Collaboration],“Direct evidence for neutrino flavor transformation from neutral-current interactions in the Sudbury Neutrino Observatory”, Phys. Rev. Lett. 89 (2002) 011301.

[STA 00] I. Stancu *et al.* [MiniBooNE collaboration], “The MiniBooNE detector technical design report”, FERMILAB-TM-2207 (2000).

[STE 88] J. Steinberger, Experiments with High-Energy Neutrino Beams”, Nobel Lectures, Physics 1981-1990, World Scientific Publishing Co., Singapore, 1993

[WAM 02] K. Wamba [EXO Collaboration], “EXO: The Enriched Xenon Observatory for double beta decay”, eConf C020620 (2002) THAP11 [arXiv:hep-ph/0210186].

[WEI 02] C. Weinheimer, “Direct neutrino mass search”, arXiv:hep-ex/0210050.

[WEL 89] W. T. Welford, R. Winston, “High Collection Nonimaging Optics”, Academic Press, Inc., (1989).

[WHI 03] K. Whisnant, J. M. Yang and B. L. Young, “Measuring CP violation and mass ordering in joint long baseline experiments with superbeams”, Phys. Rev. D 67 (2003) 013004 [arXiv:hep-ph/0208193].

[WIL 82] D. H. Wilkinson, “Analysis Of Neutron Beta Decay”, Nucl. Phys. A 377 (1982) 474.

[WOL 78] L. Wolfenstein, “Neutrino Oscillations in Matter”, Phys. Rev. D 17 (1978) 2369.

[WOL 81] L. Wolfenstein, “CP Properties Of Majorana Neutrinos And Double Beta Decay”, Phys. Lett. B 107 (1981) 77.

[WU 57] C. S. Wu, E. Ambler, R. W. Hayward, D. D. Hoppes and R. P. Hudson, “Experimental Test Of Parity Conservation In Beta Decay”, Phys. Rev. 105 (1957) 1413.

[YOR 00] D. G. York *et al.* [SDSS Collaboration], "The Sloan Digital Sky Survey: technical summary", Astron. J. 120 (2000) 1579 [arXiv:astro-ph/0006396].

[ZAT 65] G.T. Zatsepin and O.G. Razhskaya, "Calculation of neutron production by muons at different depths underground", Bull. Acad. Sci. USSR Phys. Ser. (1965) p.1779-1782.

Vielen Dank an:

Meinem Doktorvater Franz v. Feilitzsch für die herzliche Aufnahme an den Lehrstuhl und die Möglichkeit auf diesem interessanten Gebiet der Physik tätig zu werden.

Lothar Oberauer für die stete freundschaftliche Unterstützung bei meiner Arbeit und seine Hilfsbereitschaft.

Caren Hagner, dass sie es mir ermöglicht hat ein Jahr an der Viginia Tech Universität zu arbeiten.

Bruce Vogelaar und Henning Back für die herzliche Aufnahme in Virginia.

Meinen Borexino Kollegen Ludwig Niedermeier, Christian Lendvai und Davide d'Angelo für ihre Hilfsbereitschaft und Freundschaft. Ich wäere froh wenn ich immer die Möglichkeit hätte in einem Team wie diesem zu arbeiten.

Meinem langjährigen Freund und Kollegen Jean-Côme Lanfranchi der immer bereit war zu helfen oder auch ein aufmunterndes Gespräch zu führen.

Den Institutssekretärinnen Beatrice van Bellen und Alexandra Füldner für ihre aussergewöhnliche Bereitschaft mir in jeder Lage zu helfen (vor allem wenn ich einmal wieder etwas vergessen habe!).

Den Mitarbeitern in unserer Werkstatt, Harald Hess, Erich Seitz und Thomas Richter fr̈ ihre äusserst kompetente technische Unterstützung.

Allen anderen Kollegen von E15 für die freundliche Arbeitsatmospähre.

Meinen Eltern dafür dass sie es mir ermöglicht haben diesen Weg zu gehen und meiner Frau Lil für ihre Geduld und seelische Unterstützung (und auch für das Korrekturlesen!).